UCLouvain

epl

École polytechnique de Louvain

Determination of the angle of attack from blade-resolved CFD, towards improved modelling of blade-vortex interaction on rotors

Author: **Elian DEBOUVRIE**
Supervisor: **Grégoire WINCKELMANS, Denis-Gabriel CAPRACE**
Reader: **Vincent LEGAT**
Academic year 2025–2026
Master [120] : ingénieur civil mécanicien

Abstract

This work investigates the accuracy of a method based on flow velocity for extracting the angle of attack (AoA) from CFD simulations. The post-processing approach uses the velocity, pressure and density fields extracted along iso-distance contours surrounding the airfoil to estimate the circulation and the AoA. The lift coefficient is then predicted using the Kutta–Joukowski law.

Two-dimensional wall-resolved incompressible and weakly compressible simulations of a NACA0012 airfoil are first used to assess the circulation conservation and the accuracy of both the extracted AoA and the lift estimation along several extraction contours. The influence of weak compressibility effects is investigated up to Mach 0.5. Wall-resolved and wall-modeled RANS simulations are then compared to evaluate whether wall functions can accurately reproduce the near-wall flow behaviour while reducing the computational cost. Finally, the method is applied to three-dimensional configurations in which counter-rotating Lamb–Oseen vortices are imposed at the inlet to reproduce blade-vortex interaction.

The results show that the circulation is not perfectly conserved between contours, even in incompressible configurations, due to a small amount of vorticity associated with numerical effects enclosed between the contours. Under weak compressibility conditions, the classical incompressible Kutta–Joukowski formulation remains a good approximation, although compressibility effects become more visible as the Mach number increases. The wall-modeled simulations remain consistent with the wall-resolved reference cases, which justifies their use in the subsequent three-dimensional simulations.

In the three-dimensional simulations, the spanwise lift coefficient distribution is accurately estimated for the $\Omega_{0.25c}$ contour. Strong spanwise variations in the estimated quantities are observed near the vortex cores, showing that the estimation is sensitive to localized vortical structures.

Acknowledgements

Je souhaite tout d'abord adresser mes sincères remerciements au Docteur Caprace et au Professeur Winckelmans pour leur disponibilité, leur expertise et leurs précieux conseils tout au long de ce travail.

Sur un plan plus personnel, je voudrais remercier mes parents et mes sœurs pour leur soutien constant tout au long de ces cinq années d'études. Leur présence et leurs encouragements ont été essentiels dans l'accomplissement de ce parcours.

Enfin, je remercie ma copine ainsi que mes amis, avec qui j'ai partagé les doutes et la joie de cette dernière année. Leur soutien et leur présence ont rendu cette aventure plus agréable.

Notation

a	Circle radius in the Joukowski transformation, m
a_0	Lift-curve slope, rad^{-1}
b	Wing span, m
c	Chord length, m
C_d	Drag coefficient
C_l	Lift coefficient
$C_{l,\mathrm{wing}}$	Lift coefficient obtained from the wing surface
C_p	Pressure coefficient
E	Total energy per unit mass, $\mathrm{J\,kg^{-1}}$
F_1	Blending function of the k–ω SST turbulence model
k	Turbulent kinetic energy, $\mathrm{m^2\,s^{-2}}$
k_{eff}	Effective thermal conductivity, $\mathrm{W\,m^{-1}\,K^{-1}}$
l	Lift per unit span, $\mathrm{N\,m^{-1}}$
M	Mach number
p	Static pressure, Pa
r	Radial distance from the vortex core, m
r_c	Vortex core radius, m
Re	Reynolds number
Re_c	Chord Reynolds number
Re_Γ	Vortex Reynolds number
s	Curvilinear coordinate along the extraction contour, m
t	Airfoil thickness ratio
T	Static temperature, K
u	Local velocity component, $\mathrm{m\,s^{-1}}$

$\mathbf{u}$ Velocity vector, $\mathrm{m\,s^{-1}}$

$\|\mathbf{u}\|$ Velocity magnitude, $\mathrm{m\,s^{-1}}$

u_e Effective velocity, $\mathrm{m\,s^{-1}}$

$\mathbf{u}_e$ Effective velocity vector, $\mathrm{m\,s^{-1}}$

u_Γ Velocity induced by the bound circulation, $\mathrm{m\,s^{-1}}$

u_t Tangential velocity, $\mathrm{m\,s^{-1}}$

u_n Normal velocity, $\mathrm{m\,s^{-1}}$

u_τ Friction velocity, $\mathrm{m\,s^{-1}}$

u^+ Dimensionless velocity in wall units

U_∞ Freestream velocity, $\mathrm{m\,s^{-1}}$

$V_\parallel$ Velocity component parallel to the chord, $\mathrm{m\,s^{-1}}$

$V_\perp$ Velocity component normal to the chord, $\mathrm{m\,s^{-1}}$

V_θ Tangential velocity of the Lamb–Oseen vortex, $\mathrm{m\,s^{-1}}$

y^+ Dimensionless wall distance

z Spanwise coordinate, m

α Angle of attack, rad or deg

α_{ref} Reference angle of attack, rad or deg

γ Vortex-sheet strength or circulation per unit length, $\mathrm{m\,s^{-1}}$

Γ Circulation, $\mathrm{m^2\,s^{-1}}$

Γ_1 Circulation computed from the velocity integral, $\mathrm{m^2\,s^{-1}}$

Γ_2 Density-weighted circulation, $\mathrm{m^2\,s^{-1}}$

Γ_{ref} Reference circulation obtained from the Fluent lift, $\mathrm{m^2\,s^{-1}}$

Δs Curvilinear spacing between two contour points, m

Δu_t Tangential velocity jump, $\mathrm{m\,s^{-1}}$

θ Angular coordinate, rad

κ von Kármán constant

μ Dynamic viscosity, $\mathrm{Pa\,s}$

μ_t Turbulent viscosity, $\mathrm{Pa\,s}$

ν Kinematic viscosity, $\mathrm{m^2\,s^{-1}}$

ρ Density, $\mathrm{kg\,m^{-3}}$

ρ_∞ Freestream density, $\mathrm{kg\,m^{-3}}$

ρ_0 Stagnation density, $\mathrm{kg\,m^{-3}}$

$\boldsymbol{\tau}_{\mathrm{eff}}$ Effective stress tensor, Pa

ω_x Streamwise vorticity, $\mathrm{s^{-1}}$

ω_z Spanwise vorticity, $\mathrm{s^{-1}}$

$\Omega_{0.25c}$ Iso-distance contour located at $0.25c$ from the airfoil

$\Omega_{0.50c}$ Iso-distance contour located at $0.50c$ from the airfoil

$\Omega_{0.85c}$ Iso-distance contour located at $0.85c$ from the airfoil

$\Omega_{1.20c}$ Iso-distance contour located at $1.20c$ from the airfoil

Contents

Abstract i
Acknowledgements ii

Notation **iii**

1 Introduction **1**
1.1 Context 1
1.2 Tip vortex phenomenon 1
1.3 Objectives and structure of the manuscript 3
Chapter 2: Validity of the Kutta–Joukowski theorem under weak compressibility effects 3
Chapter 3: AoA and effective velocity extraction from blade-resolved 2D RANS simulations 3
Chapter 4: Wall-modeled versus wall-resolved RANS simulations . . 3
Chapter 5: AoA extraction from 3D wall-modeled RANS simulations 3

2 Validity of the Kutta–Joukowski theorem under weak compressibility effects **4**
2.1 Introduction 4
2.2 Numerical set-up 5
2.2.1 Flow solver and governing equations 5
Turbulence closure 5
Numerical discretization and solver settings 6
2.2.2 Computational domain and mesh 7
Extraction contours for post-processing 8
Mesh characteristics and quality 9
2.2.3 Fluid properties and boundary conditions 10
Incompressible cases 10
Compressible cases 11
2.3 Results 11
2.3.1 Boundary layer and tangential velocity analysis 11
Effect of AoA on Velocity Distribution 13
2.3.2 Sensitivity of the computed circulation to the integration contour . 14
2.3.3 Comparison with Fluent lift coefficient 18
2.4 Conclusion 19

3 Extraction of the AoA and effective velocity from blade-resolved 2D CFD simulations **21**
3.1 Introduction 21
3.2 Post-processing approach 21

3.2.1 Circulation distribution . . . 26
3.3 Results . . . 28
3.3.1 Prediction accuracy of the effective velocity . . . 28
3.3.2 Prediction accuracy of the AoA . . . 31
3.4 Conclusion . . . 33

4 Wall-modeled versus wall-resolved RANS simulations 34
4.1 Introduction . . . 34
4.2 Mesh . . . 34
4.3 Near-wall modeling . . . 36
4.4 Comparison between wall-modeled and wall-resolved RANS simulations . . . 37
4.4.1 $u^+(y^+)$ profiles . . . 38
4.4.2 Aerodynamic coefficients and pressure distribution . . . 38
4.4.3 Circulation variations . . . 40
4.4.4 Comparison of the AoA extraction results . . . 42
4.5 Conclusion . . . 44

5 AoA extraction from 3D wall-modeled RANS simulations 46
5.1 Introduction . . . 46
5.2 Numerical set-up . . . 46
5.2.1 Mesh and computational domain . . . 47
5.2.2 Boundary conditions . . . 47
5.2.3 Adaptive mesh refinement . . . 49
5.3 Results . . . 51
5.3.1 Case 1: Vortices convecting below the wing . . . 51
Flow topology and vortex-wing interaction . . . 51
Impact on lift coefficient estimation . . . 53
Impact on AoA extraction . . . 56
5.3.2 Case 2: Vortices impacting the wing . . . 57
Flow topology and vortex–wing interaction . . . 57
Impact on lift coefficient estimation . . . 60
Impact on the AoA extraction . . . 62
5.4 Conclusion . . . 62

6 Conclusion and Perspectives 63
6.1 Perspectives . . . 63

Use of AI 65

A 66

List of Figures

1.1 Spanwise circulation distribution 2

2.1 NACA0012 airfoil geometry 7
2.2 Computational domain and mesh topology 7
2.3 Iso-distance extraction contours 8
2.4 Curvilinear spacing along extraction contours 9
2.5 y^+ distributions for incompressible and compressible cases 9
2.6 Velocity field and sampling normals 12
2.7 Dimensionless velocity profiles and law of the wall 13
2.8 Tangential velocity and velocity magnitude at different AoA 14
2.9 Circulation variations for different Mach numbers 16
2.10 Density ratio field 17
2.11 Mach number field 17
2.12 Spanwise vorticity field for incompressible flow 18
2.13 Spanwise vorticity field at $M = 0.5$ 18
2.14 Lift coefficient polars from Fluent and Kutta–Joukowski 19

3.1 Dimensionless tangential velocity jump distribution 27
3.2 Velocity magnitude near the trailing edge at 5° 27
3.3 Velocity magnitude near the trailing edge at 10° 27
3.4 Relative error on the effective velocity predicted 29
3.5 Density ratio field ρ/ρ_∞. 30
3.6 Mach number field 30
3.7 Density ratio and Mach number fields at $M = 0.4$ 30
3.8 Dimensionless tangential velocity jump at $M = 0.4$ 31
3.9 Relative error on the AoA predicted 32

4.1 Mesh topology comparison for blunt and rounded airfoils 35
4.2 Improved near-airfoil mesh and extraction contours 36
4.3 Curvilinear spacing for the improved mesh 36
4.4 Dimensionless velocity profiles for wall-resolved and wall-modeled simulations 38
4.5 Lift coefficient comparison for incompressible cases with the different mesh configurations 39
4.6 Lift coefficient comparison for compressible cases with the different mesh configurations 39
4.7 Drag coefficient comparison for incompressible cases with the different mesh configurations for the incompressible case 39
4.8 Drag coefficient comparison for compressible cases for the different mesh configurations 39

4.9 Pressure coefficient distributions for incompressible cases with the different mesh configurations 40
4.10 Circulation variations for different mesh configurations 41
4.11 Vorticity field for the initial coarsened mesh in the incompressible case . . 41
4.12 Vorticity field for the improved mesh in the incompressible case 41
4.13 Comparison of effective velocity and AoA errors using the flat-plate assumption 43
4.14 Comparison of effective velocity and AoA errors using the uniform assumption 44

5.1 3D structured mesh and extraction contours 47
5.2 3D configuration and inlet boundary conditions 48
5.3 Counter-rotating vortices imposed at the inlet 48
5.4 Streamwise vorticity field, $\omega_x c/U_\infty$, at the inlet plane 50
5.5 Streamwise vorticity, $\omega_x c/U_\infty$, without AMR 50
5.6 Streamwise vorticity, $\omega_x c/U_\infty$, with AMR 50
5.7 Surface streamlines for case 1 51
5.8 Downstream view of the three-dimensional streamlines for case 1 52
5.9 Upstream and top view of the three-dimensional streamlines for case 1 . . 52
5.10 Dimensionless streamwise vorticity,$\omega_x c/U_\infty$, evolution downstream for the case 1 53
5.11 Spanwise lift coefficient distribution for case 1 54
5.12 (a) Dimensionless streamwise vorticity $\omega_x c/U_\infty$ in the $z/c = 0.50$ yx plane . 54
5.13 (b) Dimensionless spanwise voritcity $\omega_z c/U_\infty$ in the $z/c = 0.50$ yx plane . . 54
5.14 Dimensionless streamwise and spanwise vorticity fields for case 1 54
5.15 Vertical velocity field upstream and downstream of the wing for case 1 . . . 55
5.16 Difference between Fluent and $\Omega 0.25c$ contour lift coefficients for case 1 . . 56
5.17 AoA extraction error for case 1 56
5.18 Surface streamlines for case 2 57
5.19 Upstream streamlines for case 2 58
5.20 Downstream streamlines for case 2 58
5.21 Dimensionless streamwise vorticity evolution downstream of the wing . . . 59
5.22 Spanwise lift coefficient distribution for case 2 60
5.23 (a) Dimensionless streamwise voritcity $\omega_x c/U_\infty$ in the $z/c = 0.50$ plane . . 60
5.24 (b) Dimensionless spanwise vorticity $\omega_z c/U_\infty$ in the $z/c = 0.50$ plane 60
5.25 (a) $x/c = -1.20$ 61
5.26 (b) a $x/c = 2.20$ 61
5.27 Vertical velocity field upstream and downstream of the wing for case 2 . . . 61
5.28 Difference between Fluent and $\Omega 0.25c$ contour lift coefficients for case 2 . . 61
5.29 AoA extraction error for case 2 62

A.1 Relative error in effective velocity magnitude for the flat-plate assumption for different mesh configurations 69
A.2 Relative error in effective velocity magnitude for the flat-plate assumption for different mesh configurations 70
A.3 Dimensionless velocity profiles for the compressible case and different mesh configurations 71

List of Tables

2.1 Mesh specifications. 9
2.2 Freestream conditions used for the incompressible and compressible simulations. 10
2.3 Boundary conditions imposed for the incompressible simulations. 11
2.4 Boundary conditions imposed for the compressible simulations. 11
2.5 Local Reynolds number Re_x at the sampling locations. 12

4.1 Improved mesh specifications. 36

5.1 Experimental vortex characteristics from the NASA S-76 HVAB database . 49

Chapter 1

Introduction

1.1 Context

The aerodynamic performance of rotor blades is closely linked to the local flow conditions experienced by the blade sections. In particular, the angle of attack (AoA) and the effective velocity are key quantities governing aerodynamic loads and rotor performance. They also constitute primary variables in many aerodynamic models such as lifting line and actuator based approaches.

However, in three-dimensional flow configurations, the AoA is not uniquely defined. Indeed, the AoA derives from a definition that is strictly valid only in two-dimensional configurations.

In recent years, several approaches have been developed to estimate the local AoA directly from blade-resolved CFD simulations. Existing approaches for AoA extraction can generally be divided into three categories: methods based on axial induction, methods based on surface pressure distributions, and methods based on flow velocity measurements around the blade sections [1, 2]. The approach used in the present work belongs to the latter category. More specifically, the method relies on velocity fields sampled along contours surrounding the airfoil sections in order to estimate the circulation, the effective velocity, and the AoA.

The present work is a continuation of the study by Caprace et al. [3] and aims at further assessing the accuracy of the methodology under three-dimensional configurations involving tip vortex interaction. [4, 5, 6]

1.2 Tip vortex phenomenon

This section is adapted from the LMECA2323 [7] course notes and is included here as a brief theoretical reminder.

Along the spanwise direction of a rotor blade, the circulation around the aerodynamic profile, $\Gamma(y)$, varies as a function of the radial position y.

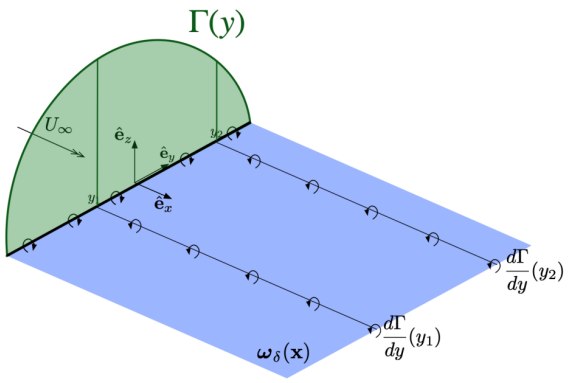
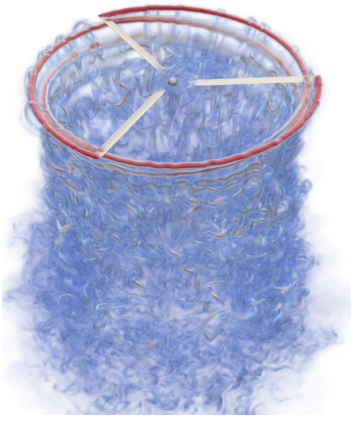


Figure 1.1: Schematic representation of the spanwise circulation distribution $\Gamma(y)$ and the associated trailing vortex sheet generated by a finite wing (from [8]).

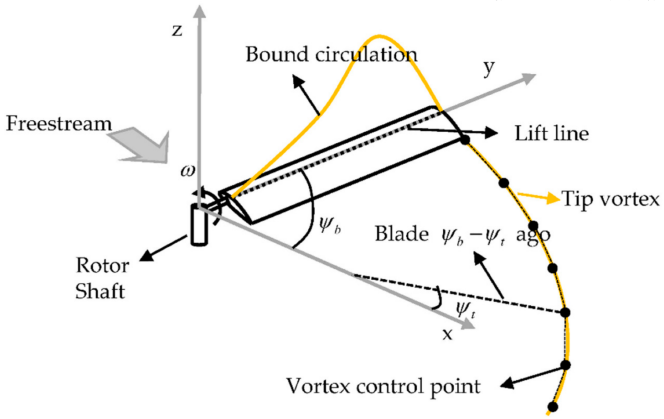
For a finite blade, the circulation distribution must vanish at both the root and the tip. Consider now a region where the circulation decreases along the spanwise direction, such that $\Gamma(y + dy) < \Gamma(y)$.

The circulation difference between two adjacent spanwise locations, $d\Gamma = \Gamma(y + dy) - \Gamma(y)$, cannot disappear abruptly. According to Helmholtz's vortex theorems, vortex tubes must remain continuous and cannot terminate within the fluid domain[9]. Therefore, any spanwise variation of bound circulation must be balanced by the shedding of vorticity into the wake.

This process generates a trailing vortex sheet downstream of the blade. The circulation per unit span of the shed vortex sheet is given by $\gamma(y) = -\frac{d\Gamma(y)}{dy}$. [10] This relation shows that the intensity of the shed vorticity is directly controlled by the spanwise circulation gradient.
Near the blade tip, the circulation rapidly decreases toward zero, leading to large values of $d\Gamma/dy$. As a result, the trailing vortex sheet becomes increasingly concentrated in this region, which leads to the roll-up and formation of a tip vortex.



(a) Volume rendering of the vorticity magnitude in the wake of the Knight and Hefner rotor (from [6]).



(b) Schematic representation of the bound circulation and the associated tip vortex generated by a rotor blade (from [11]).

In rotor configurations, the vortices generated by one blade can interact with the following

blades and alter their aerodynamic loading.

1.3 Objectives and structure of the manuscript

The main objective of this work is to apply the methodology developed by Caprace et al. [3] to three-dimensional flow involving tip vortex interactions representative of rotor applications. The work aims to assess the accuracy of the AoA extraction and lift coefficient predictions in such complex flow configurations.

The study first investigates the applicability of the Kutta–Joukowski theorem under weak compressibility effects, since the lift coefficient estimation relies on the Kutta–Joukowski theorem. The methodology is then evaluated on two-dimensional wall-resolved and wall-modeled RANS simulations in order to analyze the influence of near-wall modeling on the accuracy of the method. Finally, the approach is extended to three-dimensional wall-modeled RANS simulations involving imposed vortex interactions representative of rotor wake environments.

Chapter 2: Validity of the Kutta–Joukowski theorem under weak compressibility effects

This chapter investigates the validity of the Kutta–Joukowski theorem in weakly compressible flow conditions. The conservation of circulation and the resulting lift predictions are analyzed for several Mach numbers using blade-resolved CFD simulations.

Chapter 3: AoA and effective velocity extraction from blade-resolved 2D RANS simulations

This chapter presents the methodology used to extract the AoA and the effective velocity from two-dimensional wall-resolved RANS simulations. The influence of contour location and of the assumptions underlying the methodology on the accuracy of the predicted quantities is analyzed.

Chapter 4: Wall-modeled versus wall-resolved RANS simulations

This chapter compares wall-modeled and wall-resolved RANS simulations in order to evaluate the influence of near-wall modeling on circulation conservation, aerodynamic coefficients, and AoA extraction.

Chapter 5: AoA extraction from 3D wall-modeled RANS simulations

This chapter extends the methodology to three-dimensional wall-modeled RANS simulations involving imposed vortex interactions. The influence of the perturbations induced by the vortices on the extracted AoA and predicted lift coefficient is investigated.

Chapter 2

Validity of the Kutta–Joukowski theorem under weak compressibility effects

2.1 Introduction

The objective of this chapter is to assess the validity of the lift prediction based on the circulation using the Kutta–Joukowski relation in weakly compressible flow conditions. Two formulations are considered. The first one is based on the classical definition of circulation:

$$l_1 = \rho_\infty U_\infty \Gamma_1 \qquad [\mathrm{N/m}], \tag{2.1}$$

whereas the second one uses a density-weighted circulation in order to account for local density variations along the integration contour:

$$l_2 = \rho_\infty U_\infty \Gamma_2 \qquad [\mathrm{N/m}]. \tag{2.2}$$

The classical circulation is defined as:

$$\Gamma_1 = \oint_C \mathbf{u} \cdot \mathbf{t} ds = \oint_C u_t ds \approx \sum_{i=1}^{N-1} \frac{u_{t,i} + u_{t,i+1}}{2} \Delta s_i \qquad [\mathrm{m^2/s}] \tag{2.3}$$

where C is the integration contour, $\mathbf{t}$ is the local unit tangent vector, u_t is the tangential velocity component, and Δs_i is the distance between two consecutive contour points. The density-weighted circulation is defined as:

$$\Gamma_2 = \frac{1}{\rho_\infty} \oint_C (\rho \mathbf{u}) \cdot \mathbf{t} ds = \frac{1}{\rho_\infty} \oint_C \rho u_t ds \approx \frac{1}{\rho_\infty} \sum_{i=1}^{N-1} \frac{\rho_i u_{t,i} + \rho_{i+1} u_{t,i+1}}{2} \Delta s_i \qquad [\mathrm{m^2/s}] \tag{2.4}$$

Both quantities are evaluated numerically using trapezoidal integration along iso-distance contours surrounding the airfoil.

To evaluate the accuracy of the lift predictions obtained from Eqs. (2.1) and (2.2), the flow around a NACA0012 airfoil is investigated for Mach numbers ranging from $M = 0.3$ to $M = 0.5$ and for several AoA. An incompressible reference case at $U_\infty = 88.2$ m/s is

also considered. The CFD simulations are performed using *Ansys Fluent*. The velocity and density fields are extracted along several iso-distance contours from the airfoil surface, and the corresponding lift coefficients are computed as:

$$C_l = \frac{l}{\frac{1}{2}\rho_\infty U_\infty^2 c}. \tag{2.5}$$

The lift coefficients obtained from the Eq 2.1 and Eq 2.2 are then compared with the lift coefficients directly computed by *Ansys Fluent*.

This comparison allows the accuracy of the Kutta–Joukowski law to be assessed in weakly compressible flow configurations.

2.2 Numerical set-up

This section describes the numerical set-up used in the simulations, including the flow solver and the governing equations, the computational domain and the boundary conditions.

2.2.1 Flow solver and governing equations

The compressible Reynolds-averaged Navier–Stokes (RANS) equations are solved using ANSYS Fluent 2025 R2 Student Version. The governing equations are written in conservative form, following the formulation used in the ANSYS Fluent Theory Guide [12]. For steady compressible flow, they read:

- Continuity equation:
$$\nabla \cdot (\rho \mathbf{u}) = 0.$$
- Momentum equation:
$$\nabla \cdot (\rho \mathbf{u}\mathbf{u}) = -\nabla p + \nabla \cdot \boldsymbol{\tau}_{\text{eff}}.$$
- Energy equation:
$$\nabla \cdot [(\rho E + p)\mathbf{u}] = \nabla \cdot (k_{\text{eff}} \nabla T) + \nabla \cdot (\boldsymbol{\tau}_{\text{eff}} \cdot \mathbf{u}) + S_h.$$

In these equations, ρ is the density, $\mathbf{u}$ is the velocity vector, p is the static pressure, E is the total energy per unit mass, T is the temperature, k_{eff} is the effective thermal conductivity, and S_h is a volumetric heat source term. The effective stress tensor $\boldsymbol{\tau}_{\text{eff}}$ is defined by the turbulence closure described below.

Turbulence closure

Turbulence is modelled using the k–ω SST model [13, 14]. This model belongs to the class of eddy-viscosity models and is commonly used for turbulent flows around aerodynamic profiles. In the k–ω SST model, the Reynolds stress tensor is closed using the Boussinesq

approximation, which relates the Reynolds stresses to the mean strain rate tensor through a turbulent viscosity μ_t:

$$-\rho\overline{u_i' u_j'} = 2\mu_t S_{ij} - \frac{2}{3}\rho k \delta_{ij}, \tag{2.6}$$

where $S_{ij} = \frac{1}{2}\left(\frac{\partial \overline{u_i}}{\partial x_j} + \frac{\partial \overline{u_j}}{\partial x_i}\right)$.

The turbulent fluctuations are therefore not explicitly resolved. Their mean effect is represented through the turbulent viscosity μ_t, which contributes to the effective stress tensor:

$$\boldsymbol{\tau}_{\text{eff}} = (\mu + \mu_t)\left[\nabla \mathbf{u} + (\nabla \mathbf{u})^T - \frac{2}{3}(\nabla \cdot \mathbf{u})\mathbf{I}\right] - \frac{2}{3}\rho k \mathbf{I} \tag{2.7}$$

where μ is the dynamic viscosity and μ_t is the turbulent viscosity.

In the k–ω SST model, μ_t is computed locally from the transported turbulence quantities k and ω. It scales as $\mu_t \sim \rho\frac{k}{\omega}$.

For the compressible simulations, the compressibility correction available in the k–ω SST model is activated in order to account for dilatational effects in the turbulence model. This correction mainly affects the transport equation for the turbulent kinetic energy k through the introduction of a dilatation term.The transport equation for the specific dissipation rate ω remains unchanged [12].

Numerical discretization and solver settings

The governing equations are discretized using a finite volume method, where the computational domain is divided into control volumes and the equations are integrated over each cell. Fluxes across cell faces are evaluated to transform the governing equations into a system of algebraic equations, which is solved iteratively. A pressure-based coupled solver is used. This approach solves the momentum and pressure based continuity equations simultaneously, which generally improve convergence compared to segregated methods. Although originally developed for incompressible flows, pressure-based solvers are now capable of accurately handling compressible regimes and are preferred for their robustness and convergence properties [15].
For the compressible cases, compressibility effects are taken into account in both the solver and the turbulence model. For the incompressible case, the density is assumed constant, and compressibility effects are therefore neglected [12]. In this case, the incompressible RANS equations are solved.

At each iteration, the coupled pressure–velocity system and the remaining transport equations are solved iteratively until convergence is reached.

The equations are discretized on a co-located finite volume grid, where all variables are stored at the cell centers. Second-order upwind schemes are used for the discretization of momentum, energy, turbulence quantities, and density, while pressure is also discretized using a second-order scheme. Gradients are evaluated using a least-squares cell based method.

All simulations are performed under steady-state conditions. The simulations are considered converged when all scaled residuals fall below 10^{-6}.

2.2.2 Computational domain and mesh

The airfoil considered in this work is a NACA0012 profile with a blunt trailing edge. The airfoil coordinates were generated from the analytical NACA0012 thickness distribution, modified to account for the blunt trailing edge [7]:

$$y(x) = 5t(0.2969\sqrt{x} - 0.1260x - 0.3516x^2 + 0.2843x^3 - 0.1015x^4) \tag{2.8}$$

where $t = 0.12$ corresponds to the airfoil thickness ratio.

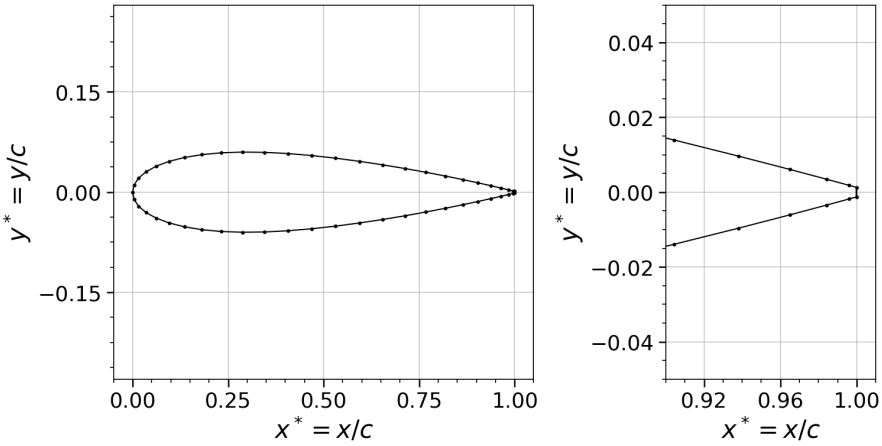


Figure 2.1: NACA 0012 airfoil geometry with a detailed view of the trailing edge region.

The computational domain consists of an inlet boundary, an outlet boundary, and the airfoil surface. To ensure that the flow arrives with the prescribed AoA, the inlet is located 7 chord lengths upstream of the airfoil, while the outlet is placed 9 chord lengths downstream. The domain shape is inspired from the work of Shelil et al. [14] and Rezaei et al. [16]

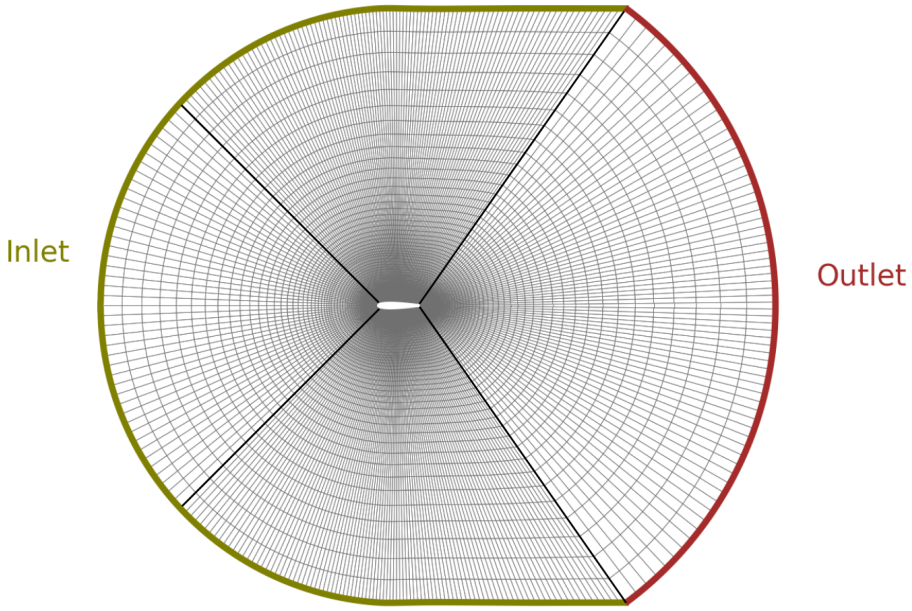


Figure 2.2: Computational domain and mesh structure around the airfoil. For visualization purposes, a coarsened version of the mesh is displayed .

When meshing the geometry in Fluent, the blunt trailing edge led to the generation of triangular elements in the near trailing edge region. To avoid this issue, the domain was partitioned by introducing additional lines connecting the airfoil to the outer boundary. These additional lines, visible as black lines in Fig. 2.2, are defined as interior boundaries in Fluent, meaning that they act like internal mesh edges [17]. The partitioning enabled better control of the mesh refinement near the airfoil but leads to a noticeable discontinuity in cell size across the mesh. This effect arises from the meshing strategy in ANSYS Meshing, where the surface discretization is imposed by specifying a fixed number of divisions along each geometric edge leading to local clustering of the cell near the trailing edge.

Extraction contours for post-processing

The velocity, density and pressure fields are retrieved on different iso-distance contours. Since Fluent is based on a finite volume formulation, the flow quantities are retrieved at cell centers.

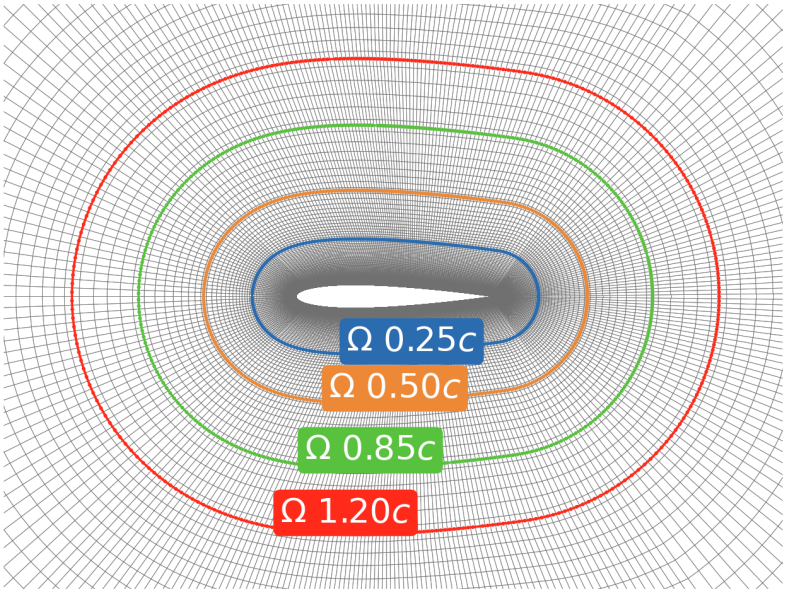


Figure 2.3: Mesh in the near-airfoil region together with the iso-distance contours used for the circulation and AoA extraction.

Here, ds denotes the curvilinear distance between two consecutive sampling points along the different contours. As the sampling points are associated with cell centers, jumps appear in the ds distribution due to the partitioning of the domain. The mesh was refined in the vicinity of the airfoil so that the curvilinear spacing ds along the closest contour remains as smooth as possible. This is particularly important as the near airfoil region is characterized by strong gradients, where abrupt variations in cell size may introduce unphysical vorticity. Consequently, the ds distribution for the contour at $0.25c$ is significantly smoother than for contours located farther away, such as at $1.20c$.

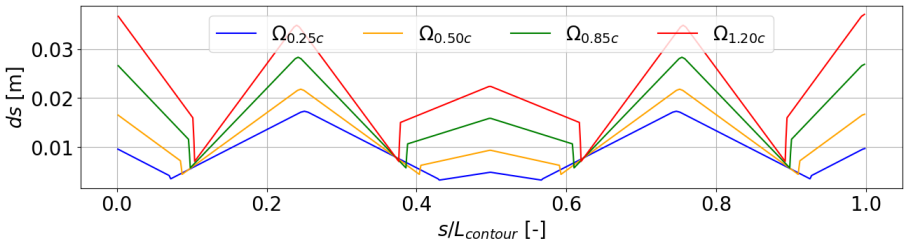


Figure 2.4: Evolution of the curvilinear spacing ds along the different iso-distance extraction contours.

Mesh characteristics and quality

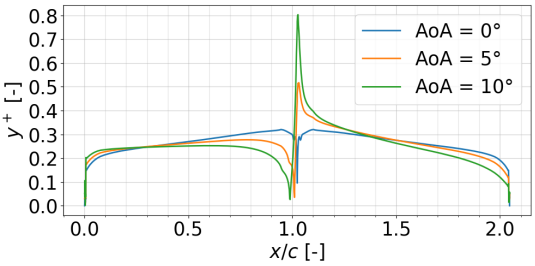
The mesh main characteristics are summarized in Table 2.1.

Number of nodes	230280
Number of cells	229775
Growth factor	1.0227

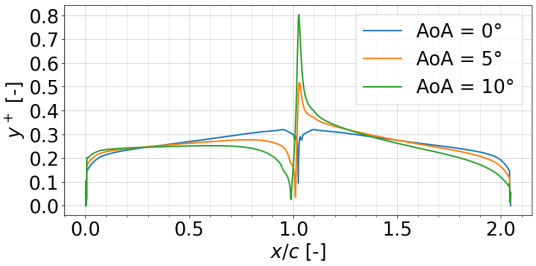
Table 2.1: Mesh specifications.

The maximum aspect ratio reaches 5.68×10^3, located near the leading edge. As the simulations are wall resolved, the first cell height must be sufficiently small to properly capture the boundary layer.

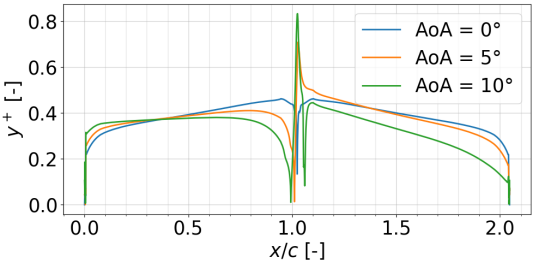
Figure 2.5 shows that the distribution of y^+ along the airfoil remains below 1 for both incompressible and compressible cases, ensuring sufficient near-wall refinement.



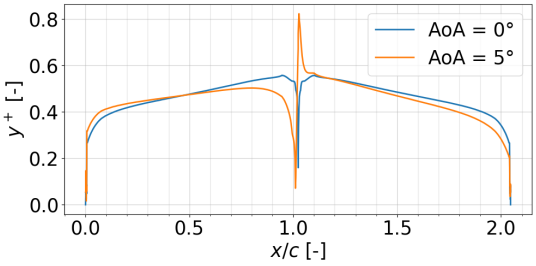
(a) Incompressible case ($U_\infty = 88.2\,\mathrm{m/s}$)



(b) Compressible case ($M = 0.3$)



(c) Compressible case ($M = 0.4$)



(d) Compressible case ($M = 0.5$)

Figure 2.5: y^+ distribution along the airfoil surface for incompressible and compressible cases at different Mach numbers and AoA.

2.2.3 Fluid properties and boundary conditions

Air is used as the working fluid in the present study. For all simulations, the operating pressure is fixed at 101325 Pa. Although the viscosity of air varies with temperature according to Sutherland's law, the temperature variations remain limited within the Mach number range considered in this work. The dynamic viscosity is therefore assumed constant and set to:

$$\mu = 1.7894 \times 10^{-5} \text{ kg/(m s)}.$$

The turbulence intensity and turbulent viscosity ratio prescribed at the inlet are used to define the incoming turbulence level. The turbulence intensity is fixed to 0.05%, while the turbulent viscosity ratio is set to 5, as recommended for external flows simulations [13, 18].

Two flow regimes are investigated: incompressible and compressible flows. The corresponding freestream conditions are summarized in Table 2.2. For the compressible cases, the freestream velocity is obtained from the prescribed Mach number using the speed of sound at the imposed static temperature.

Flow regime	M_∞	U_∞ (m/s)	Re_c
Incompressible	–	88.2	6.04×10^6
Compressible	0.3	102.1	6.99×10^6
Compressible	0.4	136.1	9.32×10^6
Compressible	0.5	170.1	1.16×10^7

Table 2.2: Freestream conditions used for the incompressible and compressible simulations.

For all the cases considered, the chord Reynolds number is larger than 6×10^6. The boundary layer is therefore expected to be predominantly turbulent over most of the airfoil surface. This assumption is consistent with the use of the fully turbulent $k-\omega$ SST model in the present simulations [19]. The following subsections detail the specific boundary conditions used for the incompressible and compressible cases, respectively.

Incompressible cases

For the incompressible simulations, the density is assumed constant and set to

$$\rho = 1.225 \text{ kg/m}^3.$$

The Reynolds number is controlled through the freestream velocity. The boundary conditions imposed for the incompressible simulations are summarized in Table 2.3 [17].

Boundary	Imposed quantities
Inlet	• Freestream velocity magnitude U_∞ • Flow direction corresponding to the prescribed AoA
Outlet	Reference static pressure
Airfoil surface	• No-slip wall condition

Table 2.3: Boundary conditions imposed for the incompressible simulations.

Compressible cases

For the compressible simulations, the density is computed using the ideal gas law. The freestream static temperature imposed at the inlet is fixed to 288.15 K. The boundary conditions imposed for the compressible simulations are summarized in Table 2.4. [12]

Boundary	Imposed quantities
Inlet	• Freestream Mach number • Freestream static pressure • Freestream static temperature • Flow direction corresponding to the prescribed AoA
Outlet	Static pressure
Airfoil surface	• No-slip wall condition • Adiabatic wall condition

Table 2.4: Boundary conditions imposed for the compressible simulations.

2.3 Results

This section presents the results related to the prediction of the lift coefficient. First, the boundary layer behaviour and the tangential velocity distribution around the airfoil are analysed. The sensitivity of the circulation prediction to the integration contour is then evaluated. Finally, the lift coefficients obtained from the two formulations introduced in Eqs. (2.1) and (2.2) are compared with the values extracted directly from Fluent.

2.3.1 Boundary layer and tangential velocity analysis

First, the boundary layer velocity profile will be discussed and compared with the classical law of the wall. The velocity field is sampled along three normals to the airfoil located at $x/c = 0.05$, 0.29 and 0.62, as shown in Fig. 2.6.

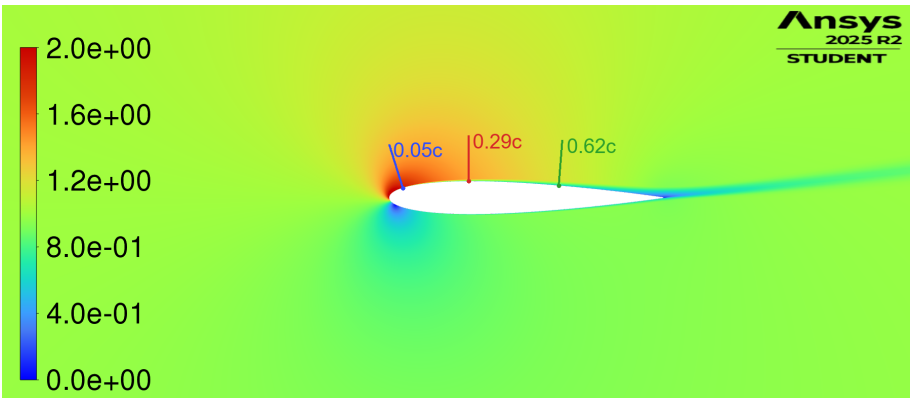


Figure 2.6: Dimensionless velocity magnitude $\|\mathbf{u}\|/U_\infty$ field for $U_\infty = 88.2\,\mathrm{m/s}$ at $\alpha = 10°$, showing the sampling normals.

The investigated case is the incompressible one with $U_\infty = 88.2$ m/s and $\alpha = 10°$. Due to the non-orthogonality of the computational mesh relative to the airfoil surface, the velocity profiles are extracted along sampling normals that do not coincide with the cell centers. Consequently, the flow field quantities are interpolated by Fluent from the cell-centered solution onto the sampling normals, which introduces an interpolation error. The resulting profiles are then expressed in terms of the non-dimensional variables u^+ and y^+.

The local Reynolds number Re_x increases along the airfoil chord, as summarized in Table 2.5.

Sampling location	Re_x
$0.05\,c$	3.0×10^5
$0.29\,c$	1.75×10^6
$0.62\,c$	3.73×10^6

Table 2.5: Local Reynolds number Re_x at the sampling locations.

This increase in Re_x directly affects the structure of the velocity profiles, as shown in Fig. 2.7. The theoretical law of the wall displayed in the figure is plotted using $\kappa = 0.385$ and $C = 4.1$.

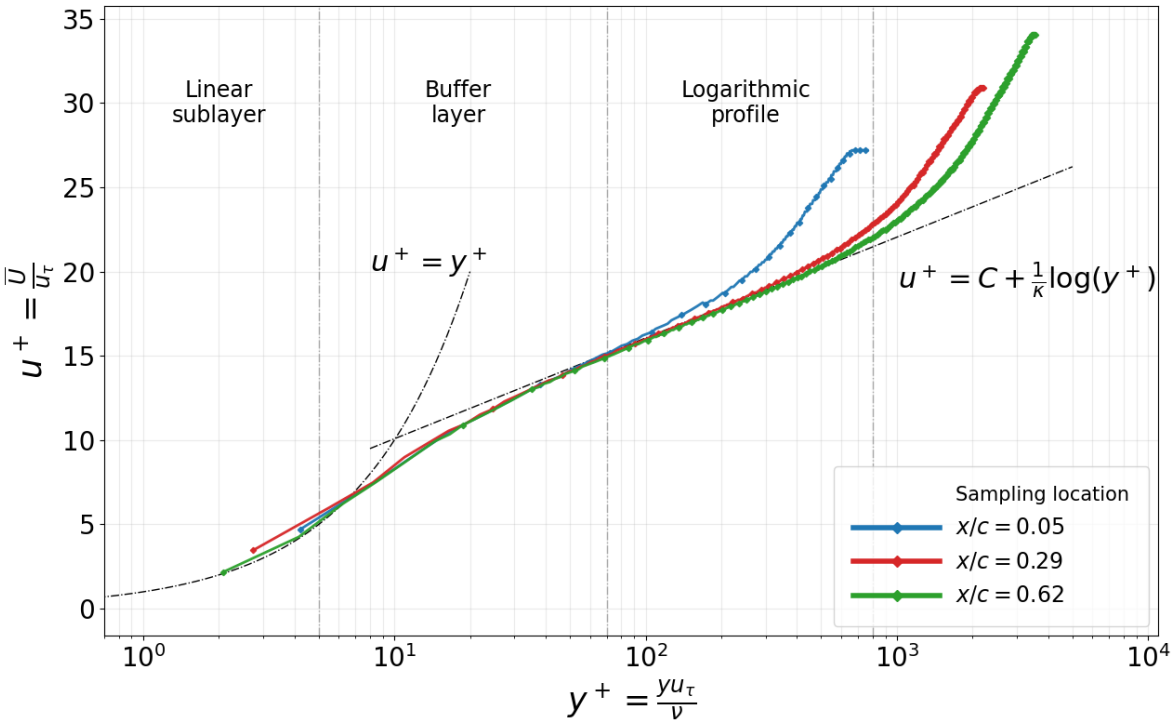


Figure 2.7: Dimensionless velocity profiles $u^+(y^+)$ along the sampling normals compared with the theoretical law of the wall (black dashed line).

At $x/c = 0.05$ ($Re_x \approx 3.0 \times 10^5$), the profile already exhibits the characteristic structure of a turbulent boundary layer, consistently with the fully turbulent k–ω SST model. However, the logarithmic region is still limited, indicating that the boundary layer is not yet fully developed at this upstream location.

Further downstream, at $x/c = 0.29$ ($Re_x \approx 1.75 \times 10^6$), the velocity profile follows the logarithmic law over a wider range of y^+. This indicates that a logarithmic region is progressively established, consistently with the development of a turbulent boundary layer in which turbulent stresses become increasingly dominant over viscous stresses [20].

At $x/c = 0.62$ ($Re_x \approx 3.73 \times 10^6$), the logarithmic region extends over an even wider range of y^+ and remains close to the theoretical law of the wall. As expected, the outer part of the profile departs from the logarithmic law.

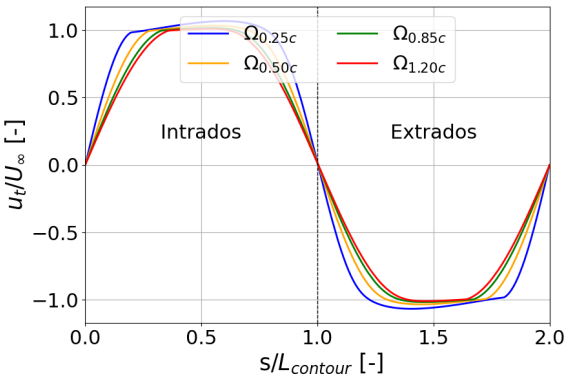
Effect of AoA on Velocity Distribution

In this section, the influence of the AoA on the flow field and on the tangential velocity distribution along the integration contour is analysed.

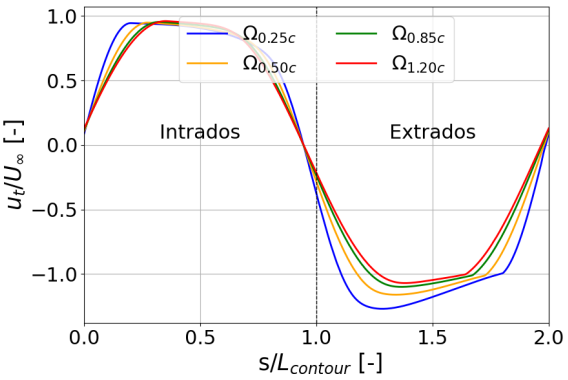
At zero AoA, the flow field is symmetric with respect to the airfoil. This symmetry is also observed in the tangential velocity distribution along the extrados and intrados, resulting in zero circulation and therefore zero lift.

For non-zero AoA, the flow becomes asymmetric. The flow accelerates over the extrados and decelerates over the intrados, leading to higher tangential velocities on the upper surface and lower tangential velocities on the lower surface.

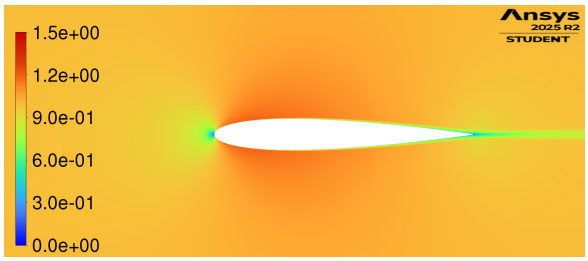
This asymmetry generates a non-zero circulation, resulting in a positive lift. Here, s denotes the curvilinear coordinate along the iso-distance contour. The coordinate starts at the trailing edge, progresses towards the leading edge along the intrados, and then returns to the trailing edge along the extrados.



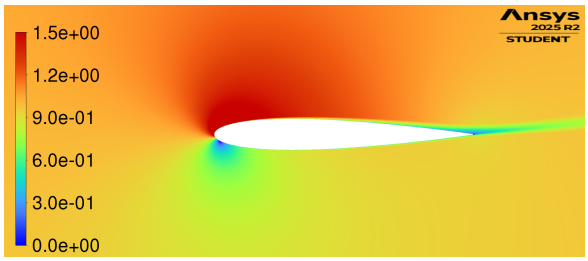
(a) Tangential velocity distribution along the iso-distance contours at $\alpha = 0°$



(b) Tangential velocity distribution along the iso-distance contours at $\alpha = 10°$



(c) Dimensionless velocity magnitude field $\|\mathbf{u}\|/U_\infty$ at $\alpha = 0°$



(d) Dimensionless velocity magnitude field $\|\mathbf{u}\|/U_\infty$ at $\alpha = 10°$

Figure 2.8: Comparison of tangential velocity profiles and dimensionless velocity magnitude field at different AoA.

2.3.2 Sensitivity of the computed circulation to the integration contour

The influence of the integration contour on the computed circulation is investigated in this section. The objective is to assess whether circulation remains conserved when different contours are used around the airfoil.

According to potential flow theory, the circulation should remain independent of the integration contour, provided that the flow is irrotational in the region enclosed between the contours. This property follows directly from Stoke's theorem[21]:

$$\Gamma_{C_2} - \Gamma_{C_1} = \iint_{S_{C_2-C_1}} \boldsymbol{\omega} \cdot \mathbf{n}\, dS \tag{2.9}$$

where $S_{C_2-C_1}$ denotes the surface enclosed between the two contours.

Therefore, if $\boldsymbol{\omega} = 0$ in this region, the circulation theoretically remains conserved:

$$\Gamma_{C_2} = \Gamma_{C_1}. \tag{2.10}$$

Since air viscosity is relatively low, viscous effects remain mainly confined to the boundary layer and wake regions, while the outer flow remains nearly irrotational. However, small variations in the computed circulation are observed depending on the contour considered.

The circulation is computed using Eqs. (2.3) and (2.4). Since the lift coefficient is obtained from Eqs. (2.1) and (2.2), any variation in the computed circulation directly affects the predicted lift coefficient. To quantify the sensitivity to contour location, both the relative variation:

$$\frac{\Gamma - \Gamma_{ref}}{\Gamma_{ref}} \quad [-] \tag{2.11}$$

and the absolute variation:

$$\Gamma - \Gamma_{ref} \quad [m^2/s] \tag{2.12}$$

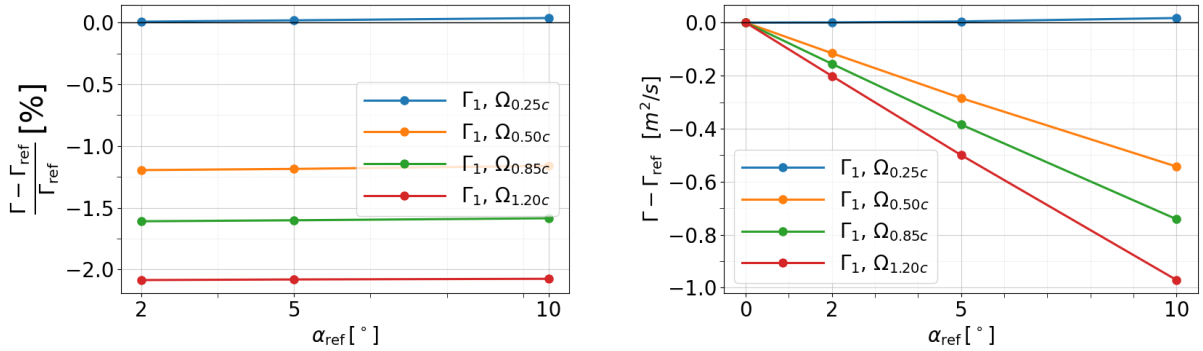
are analysed for four AoA (0°, 2°, 5°, and 10°), for both incompressible and compressible cases. The reference circulation is defined as:

$$\Gamma_{ref} = \frac{l_{\text{Fluent}}}{\rho_\infty U_\infty} \quad [m^2/s] \tag{2.13}$$

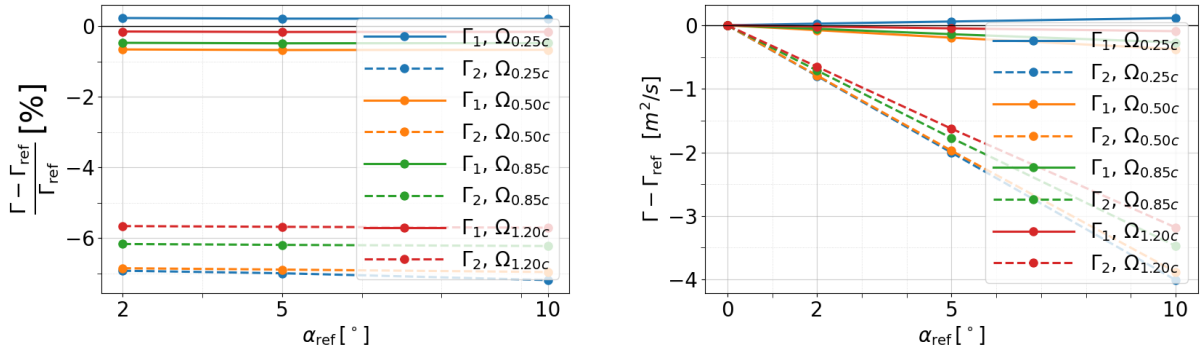
which follows directly from the Kutta–Joukowski relation using the lift predicted by Fluent.

At zero AoA, the relative variation is not meaningful because the reference circulation is close to zero. For clarity, these values are not shown in the relative variation plots. Instead, they are shown in the absolute variation plots, where they remain small.

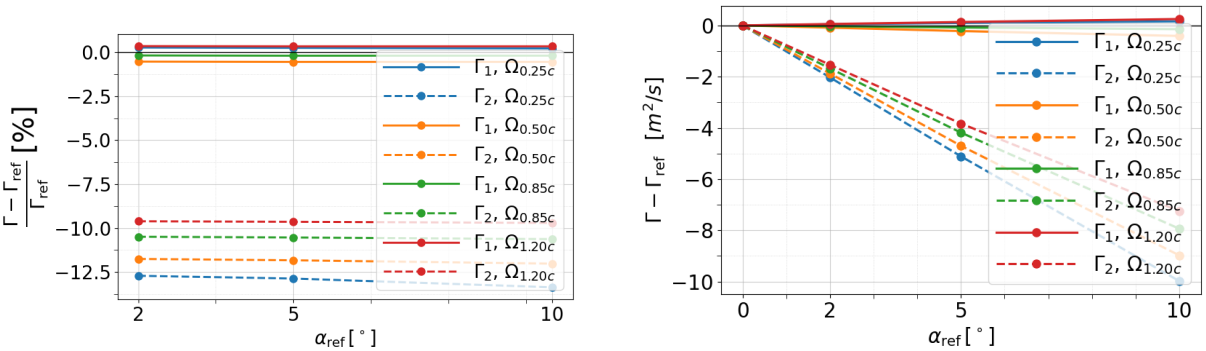
The relative variation remains nearly independent of the AoA, whereas the absolute variation $\Gamma - \Gamma_{ref}$ increases with the AoA. This behaviour is consistent with the increase of Γ_{ref} as the AoA increases, which tends to preserve a nearly constant relative variation across different AoA at a fixed freestream velocity.



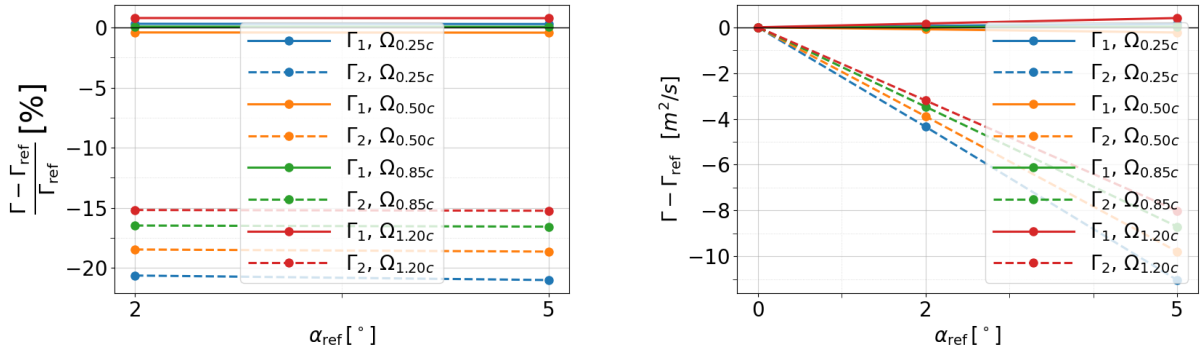
(a) Incompressible case



(b) $M = 0.3$



(c) $M = 0.4$



(d) $M = 0.5$

Figure 2.9: Relative and absolute circulation variations obtained from the Γ_1 and Γ_2 formulations as a function of the AoA for different Mach numbers.

For the incompressible case, a relative variation of approximately 2% is observed between the closest contour ($\Omega_{0.25c}$) and the farthest one ($\Omega_{1.20c}$), almost independently of the AoA. The closest contour provides the lowest relative and absolute variations from the reference circulation.

For the compressible cases, the relative variation between contours remains below 1% for the first formulation, indicating a weaker sensitivity to contour location than in the incompressible case. More specifically, the Γ_1 formulation remains weakly sensitive to contour location, whereas the Γ_2 formulation exhibits a stronger dependence, which becomes more pronounced as the Mach number increases.

The stronger contour sensitivity of Γ_2 can be explained by the inclusion of the local density in the integral. In compressible flow, the acceleration of the fluid over the extrados is linked with a local decrease in density, according to the isentropic relation [22]:

$$\frac{\rho}{\rho_0} = \left(1 + \frac{\gamma - 1}{2} M^2\right)^{-\frac{1}{\gamma - 1}} \tag{2.14}$$

On the extrados, density variations are small but non-negligible. Since the second formulation explicitly depends on the local density, its integrand becomes sensitive to the contour location. The contour $\Omega_{0.25c}$ may intersect regions with significant density gradients, whereas the contour $\Omega_{1.20c}$ may lie outside these regions. This explains the stronger sensitivity of the Γ_2 formulation to contour location.

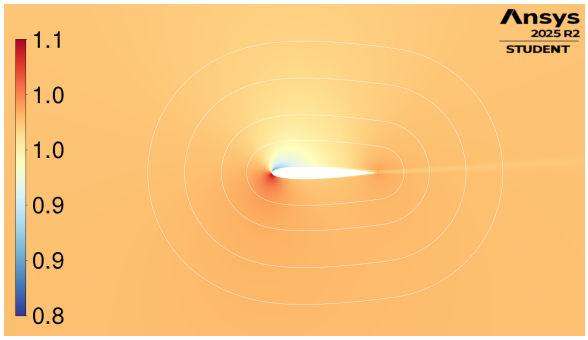


Figure 2.10: Density ratio field ρ/ρ_∞ for the flow at $M = 0.4$ and $\alpha = 5°$.

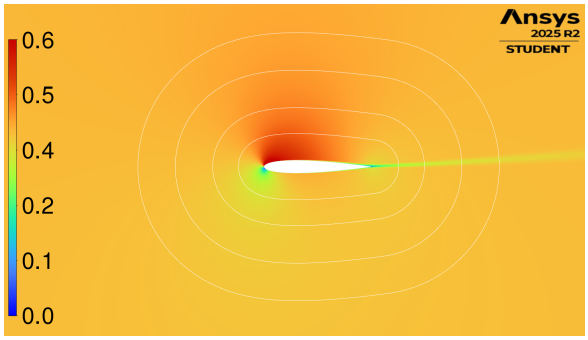


Figure 2.11: Mach number field for the flow at $M = 0.4$ and $\alpha = 5°$.

According to Stoke's theorem, the observed circulation difference between two contours should correspond to the integral of vorticity over the region enclosed between them.

One possible explanation for the observed circulation variations is the presence of mesh induced spurious vorticity near the partitioning lines, where abrupt changes in cell size occur. Since vorticity is computed from velocity gradients, these local mesh size discontinuities affect the reconstructed vorticity field [23]. This hypothesis can be assessed by examining the distribution of the dimensionless vorticity $\omega_z c/U_\infty$, as shown in Fig. 2.12.

The presence of unphysical vorticity is clearly visible in these figures. These regions therefore contribute to the observed circulation variations between contours.

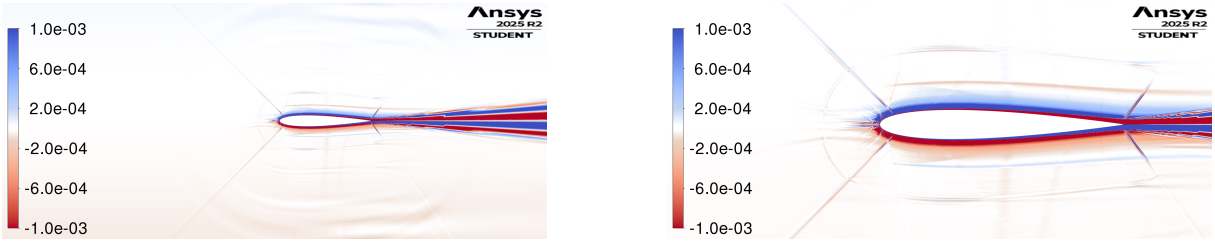


Figure 2.12: Dimensionless spanwise vorticity field $\omega_z c/U_\infty$ for the incompressible case at $\alpha = 0°$.

A similar behaviour is also observed for the case at $M = 0.5$ and $\alpha = 5°$.

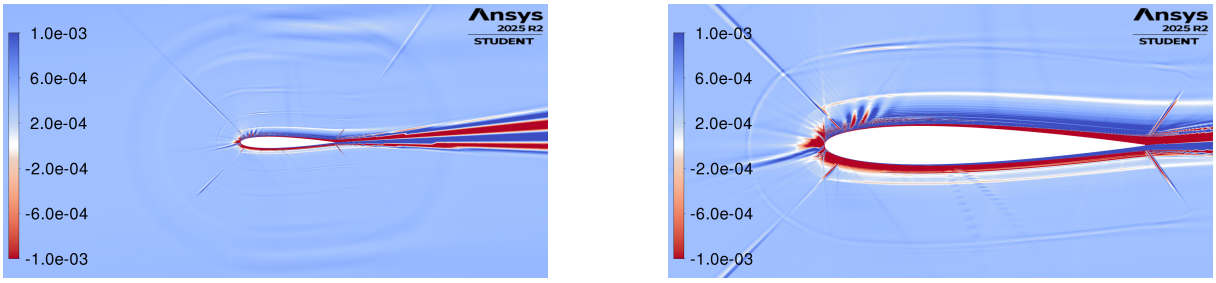


Figure 2.13: Dimensionless spanwise vorticity field $\omega_z c/U_\infty$ for the compressible case at $M = 0.5$ and $\alpha = 5°$.

For a fixed AoA, both the relative and absolute variations associated with the first formulation decrease as the Mach number increases, despite the corresponding increase in lift and circulation magnitude. This suggests that the contour sensitivity is not governed only by the amplitude of the circulation. Instead, the lower contour sensitivity observed at higher Mach numbers appears to be associated with a smaller amount of spurious vorticity enclosed between the integration contours.

2.3.3 Comparison with Fluent lift coefficient

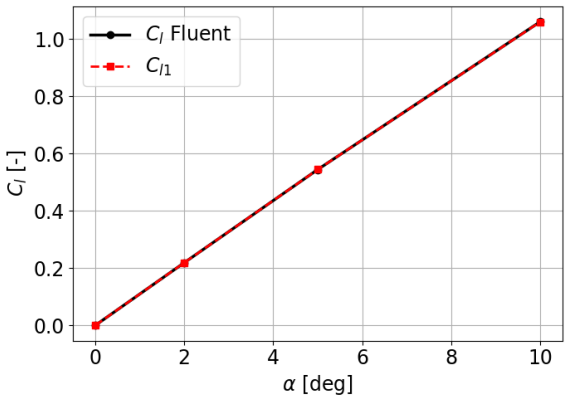
In this section, the lift coefficients predicted by the two formulations are compared with the reference values obtained from Ansys Fluent in order to assess the accuracy of the Kutta–Joukowski estimation. The formulation based on the classical circulation Γ_1 is denoted C_{l1} and is defined as:

$$C_{l1} = \frac{l_1}{\frac{1}{2}\rho_\infty U_\infty^2 c} \tag{2.15}$$

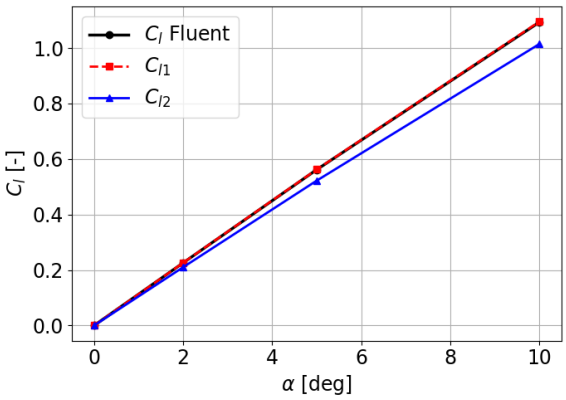
The formulation based on the density-weighted circulation Γ_2 is denoted C_{l2} and is defined as:

$$C_{l2} = \frac{l_2}{\frac{1}{2}\rho_\infty U_\infty^2 c} \tag{2.16}$$

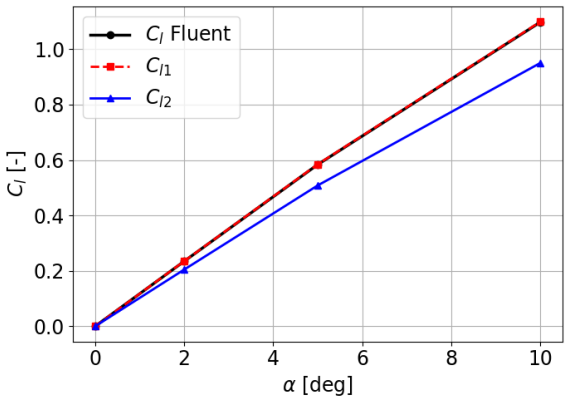
The predicted lift coefficients are computed from the flow quantities extracted along the reference contour $\Omega_{0.25c}$. This contour is selected because it is the closest to the airfoil and, as shown in the previous section, it provides the smallest deviation from the reference circulation for the first formulation, Γ_1.



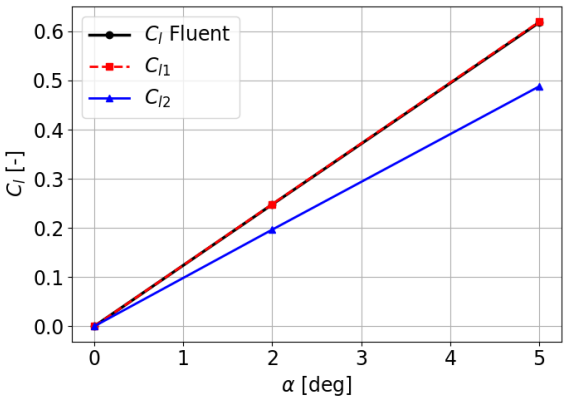
(a) Incompressible case



(b) $M = 0.3$



(c) $M = 0.4$



(d) $M = 0.5$

Figure 2.14: Lift coefficient polars obtained from Fluent and from the Kutta–Joukowski formulations (2.1) and (2.2) for the incompressible and compressible cases.

The lift polars obtained from the different approaches are shown in Fig. 2.14. The C_{l1} curve closely follows the Fluent reference results over the full range of Mach numbers considered. In contrast, the C_{l2} formulation progressively deviates from the reference solution as the Mach number increases and compressibility effects become more pronounced.

As discussed in the previous section, this deviation is related to the inclusion of the local density in the circulation integral, which makes the formulation more sensitive to compressibility effects. Consequently, the circulation magnitude predicted by Γ_2 is reduced, leading to a systematic underestimation of the lift coefficient.

2.4 Conclusion

The results show that the evaluated circulation is not perfectly conserved across the different integration contours. Although these discrepancies remain limited in magnitude, they are unphysical and may be induced by cell-size jumps present in the mesh. This highlights the importance of mesh quality for lift estimations based on the circulation.

The comparison with Fluent results shows that the first formulation (C_{l1}) provides accurate

predictions of the lift coefficient for both incompressible and weakly compressible flows. This confirms the robustness of the classical Kutta–Joukowski formulation under weak compressibility effects.

In contrast, the second formulation (C_{l2}), which explicitly includes the local density in the contour integral, systematically underestimates the lift coefficient due to the compressibility effects.

Overall, this chapter demonstrates that the classical Kutta–Joukowski formulation remains valid and reliable in weakly compressible flow regimes. Therefore, the lift coefficient can be accurately predicted from the circulation using the classical Kutta–Joukowski relation.

Chapter 3

Extraction of the AoA and effective velocity from blade-resolved 2D CFD simulations

3.1 Introduction

This chapter presents the post-processing algorithm developed by Caprace et al. [3]. The objective of this approach is to estimate the effective velocity and the AoA from flow field quantities extracted along iso-distance contours surrounding the airfoil in steady two-dimensional CFD simulations.

The performance of the algorithm is then investigated through the relative errors associated with both the predicted AoA and the effective velocity magnitude $\|\mathbf{u}_e\|$, for different flow conditions and contour locations.

3.2 Post-processing approach

This section presents the methodology implemented in the post-processing code. The underlying idea is to decompose the extracted velocity field into the incoming undisturbed flow and the perturbation induced by the bound circulation around the airfoil. By removing the latter contribution, a representative inflow velocity can be reconstructed, allowing the estimation of the AoA.
The different steps of the algorithm are described below:

- **Data extraction:** The velocity, pressure, and density fields are extracted along several contours surrounding the airfoil. Since *Ansys Fluent* is a finite-volume solver, the flow quantities are retrieved at the cell centers in order to avoid interpolation errors [12].
- **Circulation computation:** Since the flow quantities are extracted along the contours, the circulation along each contour is computed using the line integral of the tangential velocity.

While the total circulation is directly obtained from the contour integration, its spatial distribution remains unknown and must therefore be modeled. The airfoil contour is discretized into vortex panels using the actual airfoil geometry. The total circulation is then distributed over these panels according to a flat plate vortex sheet distribution. This distribution is used as an approximate representation of the bound circulation distribution along the airfoil.

Two circulation distributions are considered:

- Uniform circulation distribution: constant vortex sheet strength distributed uniformly along the chord:

$$\gamma(x) = \frac{\Gamma}{c} \tag{3.1}$$

- Flat plate circulation distribution: chordwise varying vortex sheet strength based on the flat plate distribution:

$$\gamma(x) = \frac{2\Gamma}{\pi c}\sqrt{\frac{1 - x/c}{x/c}}. \tag{3.2}$$

This second distribution uses the flat plate theory only to prescribe the chordwise scaling of the bound circulation. This scaling can be derived from two equivalent theoretical approaches: thin airfoil theory and potential flow theory based on a Joukowski transformation. Both approaches rely on an inviscid flat plate representation of the airfoil and lead to the same chordwise dependence of $\gamma(x)$.
The amplitude is then fixed by the normalization factor $2\Gamma/(\pi c)$, so that the integral of the distribution over the chord recovers the circulation Γ extracted from the iso-distance contour. The derivation used to obtain the normalization factor is provided in Appendix A.

Thin airfoil theory
This theory assumes an inviscid, incompressible and irrotational flow around a thin airfoil at small angle of attack [7]. The airfoil thickness is neglected and the bound circulation is represented by a vortex sheet distributed along the camber line. For a symmetric airfoil such as the NACA0012, the camber line reduces to a flat plate.

The coordinate x represents a point located on the flat plate where the non-penetration boundary condition is enforced. The variable ξ denotes the position of an infinitesimal vortex element distributed along the plate. The following integral equation therefore evaluates the cumulative velocity induced at the point x by all vortex elements distributed over the flat plate.

$$\frac{1}{2\pi}\int_0^c \frac{\gamma(\xi)}{x - \xi}\, d\xi = V_\infty \alpha \tag{3.3}$$

where V_∞ is the freestream velocity and α is the angle of attack.
Introducing the change of variable:

$$\xi = \frac{c}{2}(1 + \cos\theta) \quad \text{and} \quad x = \frac{c}{2}(1 + \cos\theta_0) \tag{3.4}$$

Eq. (3.3) becomes:

$$\frac{1}{2\pi}\int_0^{\pi}\frac{\gamma(\theta)\sin\theta}{\cos\theta_0-\cos\theta}\,d\theta = V_\infty\alpha \tag{3.5}$$

The analytical solution of this equation is:

$$\gamma(\theta) = 2\alpha V_\infty\frac{1-\cos\theta}{\sin\theta} \tag{3.6}$$

Using the inverse transformation of Eq. (3.4)

$$\cos\theta = \frac{2x}{c} - 1 \tag{3.7}$$

$$\sin\theta = \sqrt{1-\cos^2\theta} = \sqrt{1-\left(\frac{2x}{c}-1\right)^2} = 2\sqrt{\frac{x}{c}\left(1-\frac{x}{c}\right)} \tag{3.8}$$

Thus, the flat plate vortex sheet strength distribution is:

$$\gamma(x) = 2\alpha V_\infty\frac{2\left(1-\frac{x}{c}\right)}{2\sqrt{\frac{x}{c}\left(1-\frac{x}{c}\right)}} = 2\alpha V_\infty\sqrt{\frac{1-x/c}{x/c}} \tag{3.9}$$

This distribution is singular at the leading edge and progressively decreases to zero toward the trailing edge, highlighting the strongly non uniform nature of the bound circulation distribution over a flat plate. The same result can also be obtained from potential flow theory using a conformal transformation.

Potential flow theory

The flat plate circulation distribution can also be derived from potential flow theory [21]. The coordinate $\tilde{x} \in [0, c]$ is measured from the leading edge to the trailing edge of the flat plate. The resulting vortex sheet strength expression is:

$$\gamma = u^+ - u^- = 2U_\infty\sqrt{\frac{1-\frac{\tilde{x}}{c}}{\frac{\tilde{x}}{c}}}\sin\alpha \tag{3.10}$$

Assuming small AoA, $\sin\alpha \simeq \alpha$, which gives:

$$\gamma(\tilde{x}) \simeq 2U_\infty\alpha\sqrt{\frac{1-\tilde{x}/c}{\tilde{x}/c}} \tag{3.11}$$

Therefore, under the small AoA assumption, the circulation distribution obtained from potential flow theory in Eq. 3.11 is identical to the result derived from thin airfoil theory in Eq. 3.9.

The full derivation of Eqs. 3.10 and 3.11 is provided in Appendix A.

- **Induced velocity correction:** The velocity induced by the bound circulation, denoted by $\mathbf{u}_\Gamma$, is estimated along the contour using a Biot–Savart formulation. [24, 3]. The objective is to reconstruct the velocity induced by the bound circulation of the airfoil at each point of the iso-distance contours and subtract it from the extracted velocity field in order to reconstruct the effective velocity vector.

For a two-dimensional incompressible flow, the velocity induced by a vorticity distribution $\omega(\mathbf{x}')$ is given by the Biot–Savart law:

$$\mathbf{v}(\mathbf{x}) = -\frac{1}{2\pi} \int \frac{(\mathbf{x} - \mathbf{x}') \times (\omega(\mathbf{x}')\, \hat{\mathbf{e}}_z)}{|\mathbf{x} - \mathbf{x}'|^2}\, d\mathbf{x}' \tag{3.12}$$

In the present approach, the vorticity is assumed to be concentrated on the airfoil surface. This corresponds to modeling the bound circulation as a vortex sheet of strength $\gamma(s)$ distributed along the airfoil contour.

Mathematically, this assumption can be expressed using a Dirac distribution localised on the airfoil surface $\omega(\mathbf{x}') = \gamma(s)\, \delta(\mathbf{x}' - \mathbf{x}'(s))$

Substituting this expression into the Biot–Savart formulation yields the velocity induced by the vortex sheet:

$$\mathbf{u}_\Gamma(\mathbf{x}) = \frac{1}{2\pi} \int_{\text{airfoil}} \frac{\gamma(s)\, \mathbf{e}_z \times (\mathbf{x} - \mathbf{x}'(s))}{|\mathbf{x} - \mathbf{x}'(s)|^2}\, ds. \tag{3.13}$$

The airfoil is discretized into N panels. In the constant panel approximation, the vortex sheet strength is assumed constant over each panel:

$$\gamma(s) \approx \gamma_j \qquad \text{for } s \in \text{panel } j. \tag{3.14}$$

The total induced velocity is therefore approximated as the sum of the contributions of all panels:

$$\mathbf{u}_\Gamma(\mathbf{x}) = \sum_{j=1}^{N_p} \frac{\gamma_j}{2\pi} \int_{\text{panel } j} \frac{\mathbf{e}_z \times (\mathbf{x} - \mathbf{x}')}{|\mathbf{x} - \mathbf{x}'|^2}\, ds'. \tag{3.15}$$

The integral is therefore reduced to the analytical evaluation of the induced velocity generated by a single straight vortex panel.

Consider panel j, of length L_j, defined by its endpoints $\mathbf{s}_{0,j}$ and $\mathbf{s}_{1,j}$. A local orthonormal basis attached to the panel is introduced:

- $\mathbf{t}_j$: unit tangent vector along the panel,
- $\mathbf{n}_j$: unit normal vector.

The observation point $\mathbf{x}$ is expressed in this local frame as (x, y), where:

- x is the tangential coordinate,
- y is the signed normal distance to the panel.

The source point on panel j is parameterized by the local tangential coordinate x', such that $x' \in [-L_j/2,\, L_j/2]$. The two endpoints of the panel correspond to the local coordinates $x'_0 = -\frac{L_j}{2}$ and $x'_1 = \frac{L_j}{2}$.

The vector connecting the source point to the observation point can then be written as: $\mathbf{x} - \mathbf{x}' = (x - x')\, \mathbf{t}_j + y\, \mathbf{n}_j$.

Using the identities $\mathbf{e}_z \times \mathbf{t}_j = \mathbf{n}_j$ $\mathbf{e}_z \times \mathbf{n}_j = -\mathbf{t}_j$. One obtains $\mathbf{e}_z \times (\mathbf{x} - \mathbf{x}') = (x - x')\, \mathbf{n}_j - y\, \mathbf{t}_j$.

Substituting this expression into the Biot–Savart integral gives:

$$\mathbf{u}_\Gamma^{(j)}(\mathbf{x}) = \frac{\gamma_j}{2\pi} \int_{-L_j/2}^{L_j/2} \frac{(x - x')\,\mathbf{n}_j - y\,\mathbf{t}_j}{(x - x')^2 + y^2}\, dx'. \tag{3.16}$$

The induced velocity can be decomposed into tangential and normal components:

$$\mathbf{u}_\Gamma^{(j)} = u_t^{(j)}\,\mathbf{t}_j + u_n^{(j)}\,\mathbf{n}_j, \tag{3.17}$$

with:

$$u_t^{(j)} = -\frac{\gamma_j}{2\pi} \int_{-L_j/2}^{L_j/2} \frac{y}{(x - x')^2 + y^2}\, dx', \quad u_n^{(j)} = \frac{\gamma_j}{2\pi} \int_{-L_j/2}^{L_j/2} \frac{x - x'}{(x - x')^2 + y^2}\, dx'. \tag{3.18}$$

The tangential integral is obtained using the identity:

$$\frac{d}{dx'}\left[\arctan\left(\frac{x - x'}{y}\right)\right] = -\frac{y}{(x - x')^2 + y^2}. \tag{3.19}$$

Integrating analytically yields:

$$u_t^{(j)} = \frac{\gamma_j}{2\pi}\left[\arctan\left(\frac{x - x_1'}{y}\right) - \arctan\left(\frac{x - x_0'}{y}\right)\right] \tag{3.20}$$

which yields

$$u_t^{(j)} = \frac{\gamma_j}{2\pi}\left[\arctan\left(\frac{x - L_j/2}{y}\right) - \arctan\left(\frac{x + L_j/2}{y}\right)\right]. \tag{3.21}$$

Introducing the endpoint angles

$$\theta_{0,j} = \arctan\left(\frac{x - x_0'}{y}\right), \qquad \theta_{1,j} = \arctan\left(\frac{x - x_1'}{y}\right), \tag{3.22}$$

the tangential component can be written compactly as

$$u_t^{(j)} = \frac{\gamma_j}{2\pi}\,(\theta_{1,j} - \theta_{0,j}). \tag{3.23}$$

Geometrically, $\theta_{0,j}$ and $\theta_{1,j}$ represent the angles under which the two endpoints of panel j are seen from the observation point.

For the normal component, using:

$$\frac{d}{dx'}\left[\ln\Big((x - x')^2 + y^2\Big)\right] = -\frac{2(x - x')}{(x - x')^2 + y^2}, \tag{3.24}$$

One obtains:

$$u_n^{(j)} = \frac{\gamma_j}{4\pi} \ln\left(\frac{(x - x_0')^2 + y^2}{(x - x_1')^2 + y^2}\right). \tag{3.25}$$

Introducing the distances from the observation point to the two endpoints of panel j,

$$r_{0,j} = |\mathbf{x} - \mathbf{s}_{0,j}|, \qquad r_{1,j} = |\mathbf{x} - \mathbf{s}_{1,j}|, \tag{3.26}$$

where $\mathbf{s}_{0,j}$ and $\mathbf{s}_{1,j}$ denote the position vectors of the first and second endpoints of panel j in the global Cartesian frame.
One obtains the compact expression:

$$u_n^{(j)} = \frac{\gamma_j}{4\pi} \ln\left(\frac{r_{0,j}^2}{r_{1,j}^2}\right) = \frac{\gamma_j}{2\pi} \frac{1}{2} \ln\left(\frac{r_{0,j}^2}{r_{1,j}^2}\right). \tag{3.27}$$

Here, $r_{0,j}$ and $r_{1,j}$ correspond to the distances between the observation point and the two endpoints of panel j. The induced velocity of one panel in its local frame is

$$\mathbf{u}_{\Gamma,\mathrm{loc}}^{(j)} = \frac{\gamma_j}{2\pi} \begin{pmatrix} \theta_{1,j} - \theta_{0,j} \\ \frac{1}{2} \ln\left(\frac{r_{0,j}^2}{r_{1,j}^2}\right) \end{pmatrix}. \tag{3.28}$$

Summing over all panels gives the total induced velocity:

$$\mathbf{u}_\Gamma(\mathbf{x}) = \sum_{j=1}^{N_p} \frac{\gamma_j}{2\pi} R(\alpha_j) \begin{pmatrix} \theta_{1,j} - \theta_{0,j} \\ \frac{1}{2} \ln\left(\frac{r_{0,j}^2}{r_{1,j}^2}\right) \end{pmatrix} \tag{3.29}$$

where $R(\alpha_j)$ denotes the rotation matrix transforming the velocity components from the local panel frame $(\mathbf{t}_j, \mathbf{n}_j)$ to the global Cartesian frame.
The effective inflow velocity is then reconstructed by subtracting the induced contribution from the measured velocity field:

$$\mathbf{u}_e = \frac{1}{L} \int_\Omega (\mathbf{u} - \mathbf{u}_\Gamma)\, dl \;\approx\; \sum_{j=1}^{N} (\mathbf{u}_j - \mathbf{u}_{\Gamma j}) \frac{\Delta l_j}{L}. \tag{3.30}$$

- **Determination of the AoA:** Finally, the AoA is defined as the signed angle between the airfoil chord direction $\mathbf{c}$ and the reconstructed effective velocity vector $\mathbf{u}_e$:

$$\alpha = \angle(\mathbf{c}, \mathbf{u}_e). \tag{3.31}$$

3.2.1 Circulation distribution

The objective of this section is to assess whether the circulation distribution along the airfoil can be approximated either by the flat plate distribution derived from potential flow theory or by a uniform distribution. In potential flow theory, the circulation per unit length is directly related to the tangential velocity jump across a vortex sheet:

$$\gamma(x) = u_t(x, 0^+) - u_t(x, 0^-), \tag{3.32}$$

where $u_t(x, 0^+)$ and $u_t(x, 0^-)$ denote the tangential velocity evaluated just above and below the plate [21].

This relation strictly holds for an idealized flat plate represented as a vortex sheet. For an airfoil of finite thickness in viscous flow, the velocity jump must be reconstructed from the flow field surrounding the airfoil.

To evaluate the validity of these assumptions, the tangential velocity is extracted along an iso-distance contour located at a distance of $2 \times 10^{-2}c$ from the airfoil surface. The velocity difference between the extrados and intrados is then reconstructed as a function of the chordwise coordinate and compared with the flat plate distribution A.4.

To reduce the direct dependence on the AoA, the reconstructed velocity jump is normalized by the corresponding value of Γ/c for the incompressible cases at 5° and 10° angle of attack. The resulting dimensionless quantities are:

$$\frac{\Delta u_t^{FP}}{\Gamma/c} = \frac{2}{\pi}\sqrt{\frac{1-x/c}{x/c}} \qquad \text{and} \qquad \Delta u_t^* = \frac{\Delta u_t}{\Gamma/c}. \tag{3.33}$$

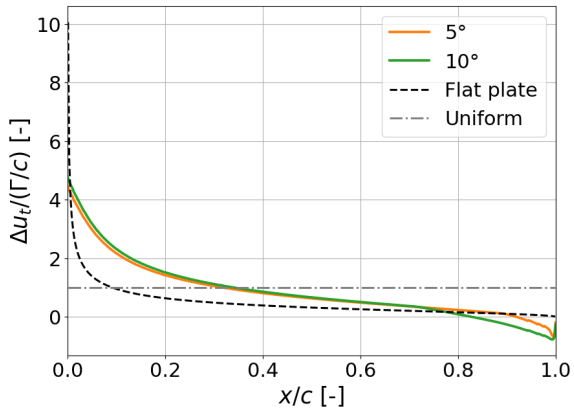


Figure 3.1: Dimensionless tangential velocity jump along the chordwise direction for different AoA, compared with the theoretical flat-plate distribution.

Near the trailing edge, the reconstructed velocity jump becomes locally negative. This behaviour is due to the presence of a small recirculation region on the extrados, while the flow remains attached on the intrados, leading to a negative local tangential velocity difference.

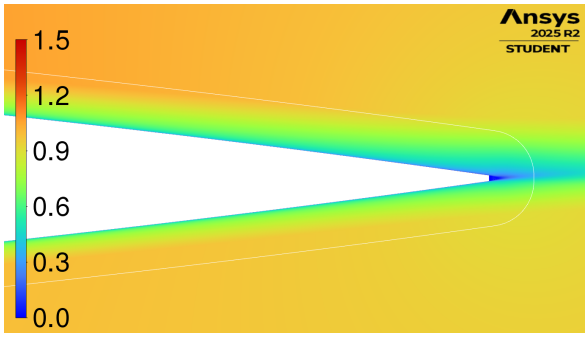


Figure 3.2: Dimensionless velocity magnitude field $\|\mathbf{u}\|/U_\infty$ in the near trailing-edge region for the incompressible case at $\alpha = 5°$

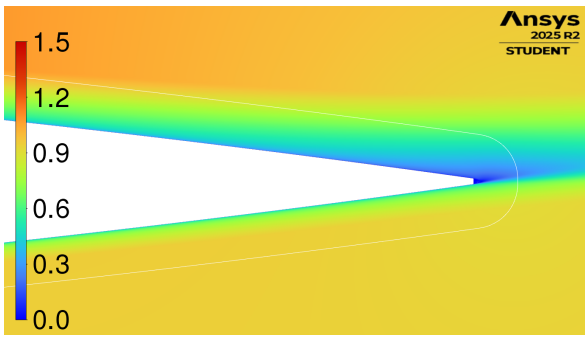


Figure 3.3: Dimensionless velocity magnitude field $\|\mathbf{u}\|/U_\infty$ in the near trailing-edge region for the incompressible case at $\alpha = 10°$

Overall, the reconstructed distribution exhibits the same qualitative behaviour as the flat plate solution. In particular, a strong increase in the velocity jump is observed near

the leading edge, consistent with the leading edge singularity predicted by potential flow theory. However, the CFD results remain finite because the leading edge radius of the airfoil is finite.

In contrast, the uniform circulation distribution assumption does not reproduce the strong spatial variations observed near the leading edge and therefore provides only a simplified approximation of the circulation distribution along the airfoil.

3.3 Results

This section presents the prediction accuracy of the AoA and of the effective velocity magnitude.

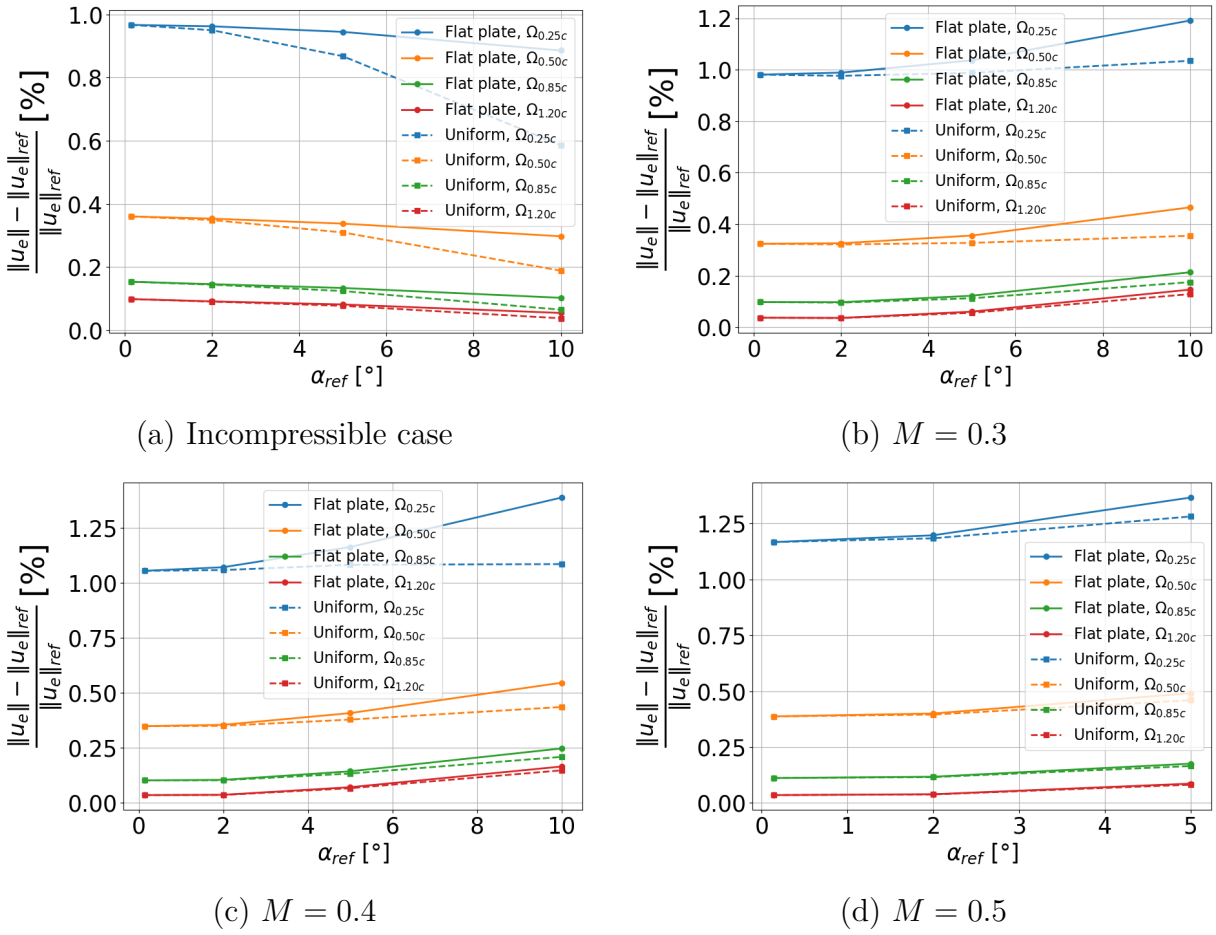
Two main aspects are investigated. First, the sensitivity of the effective velocity estimation to the assumed circulation distribution and to the contour location is analyzed. As mentioned previously, two circulation models are considered: a uniform circulation distribution and the flat plate circulation distribution. Second, the accuracy of the AoA prediction is assessed under the same conditions.

The reference inflow velocity is known in both magnitude and direction since it is imposed at the inlet. The AoA is therefore defined as the angle between the inflow velocity and the airfoil chord. In the present cases, the reference AoA is known by definition. The prescribed values of α_{ref} are 2°, 5°, and 10°, respectively.

The analysis is performed for both incompressible and compressible cases in order to evaluate the impact of compressibility effects on the post-processing code.

3.3.1 Prediction accuracy of the effective velocity

The relative error on the effective inflow velocity magnitude $\|\mathbf{u}_e\|$ is evaluated for different flow conditions, circulation models, and contour locations.



(a) Incompressible case

(b) $M = 0.3$

(c) $M = 0.4$

(d) $M = 0.5$

Figure 3.4: Relative error in the extracted effective velocity magnitude $\|\mathbf{u}_e\|$ as a function of α_{ref} for different Mach numbers, circulation models, and contour locations.

The prediction of the effective velocity shows limited sensitivity to the assumed circulation distribution. Both the uniform and flat plate circulation models provide comparable results over the investigated flow conditions.

In contrast, the prediction accuracy strongly depends on the contour location, with the relative error progressively decreasing as the contour moves away from the airfoil. This behavior can be explained by the evolution of the induced velocity field with increasing distance from the airfoil. Close to the airfoil, the induced velocity strongly depends on the local circulation distribution, making the correction highly sensitive to modelling assumptions. Further away from the airfoil, the induced velocity field becomes progressively smoother and increasingly governed by the total circulation rather than by its detailed spatial distribution. As a result, the prediction becomes less sensitive to modelling discrepancies and the overall accuracy improves.

Similarly, the effective velocity predicted using the two assumed circulation distribution becomes closer as the contour distance increases because the corresponding induced velocity field becomes more similar.

Although both circulation models lead to similar results, the uniform distribution generally provides slightly lower errors.

The results further indicate that the prediction accuracy cannot be explained solely by

the quality of the circulation estimation. Although the circulation evaluated on the closest contours is often more accurate, as observed in Figure 2.9, the corresponding effective velocity predictions exhibit larger errors. This confirms that the accuracy of the induced velocity reconstruction depends not only on the circulation accuracy, but also on the assumed spatial circulation distribution.

Since the relative error remains positive, the predicted $\|\mathbf{u}_e\|$ is generally larger than the reference value. This indicates that the induced velocity correction is underestimated. Consequently, the correction does not fully remove the local induction effects, leading to an overprediction of the effective velocity.

Compressibility effects remain moderate in the present study. Across the investigated Mach number range, the method maintains a relatively consistent level of accuracy, indicating that the incompressible induced velocity correction remains reasonably valid for weakly compressible flows.

However, for a fixed angle of attack, the relative error tends to increase with Mach number, particularly at higher incidence. This trend becomes noticeable at $\alpha = 10°$, where the incompressible case exhibits a reduction in error while compressible cases show an increase. For the $M = 0.4$ case at 10°, a weak shock appears on the extrados, as illustrated in Figure 3.6. The presence of this weak shock introduces a local flow discontinuity. Therefore, the incompressible Biot–Savart correction and the idealized circulation distributions used to reconstruct $\mathbf{u}_e$ become less representative of the actual flow physics.

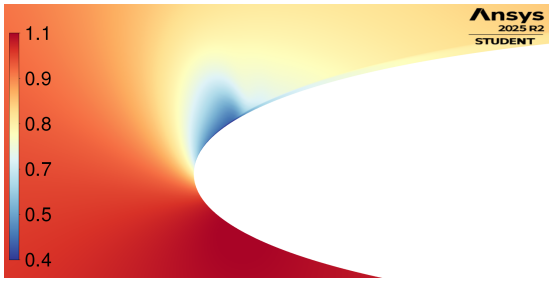


Figure 3.5: Density ratio field ρ/ρ_∞.

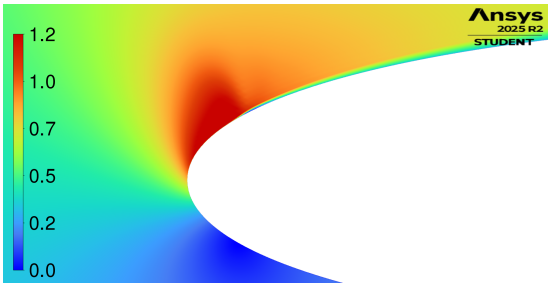


Figure 3.6: Mach number field

Figure 3.7: Density ratio and Mach number fields for the $M = 0.4$, $\alpha = 10°$ case showing a weak shock on the suction side of the airfoil.

To further investigate this behavior, the dimensionless tangential velocity jump distribution $\Delta u_t/(\Gamma/c)$ is analyzed for this flow condition.

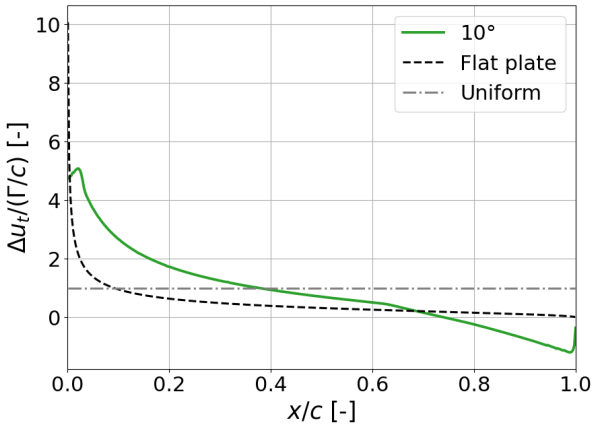


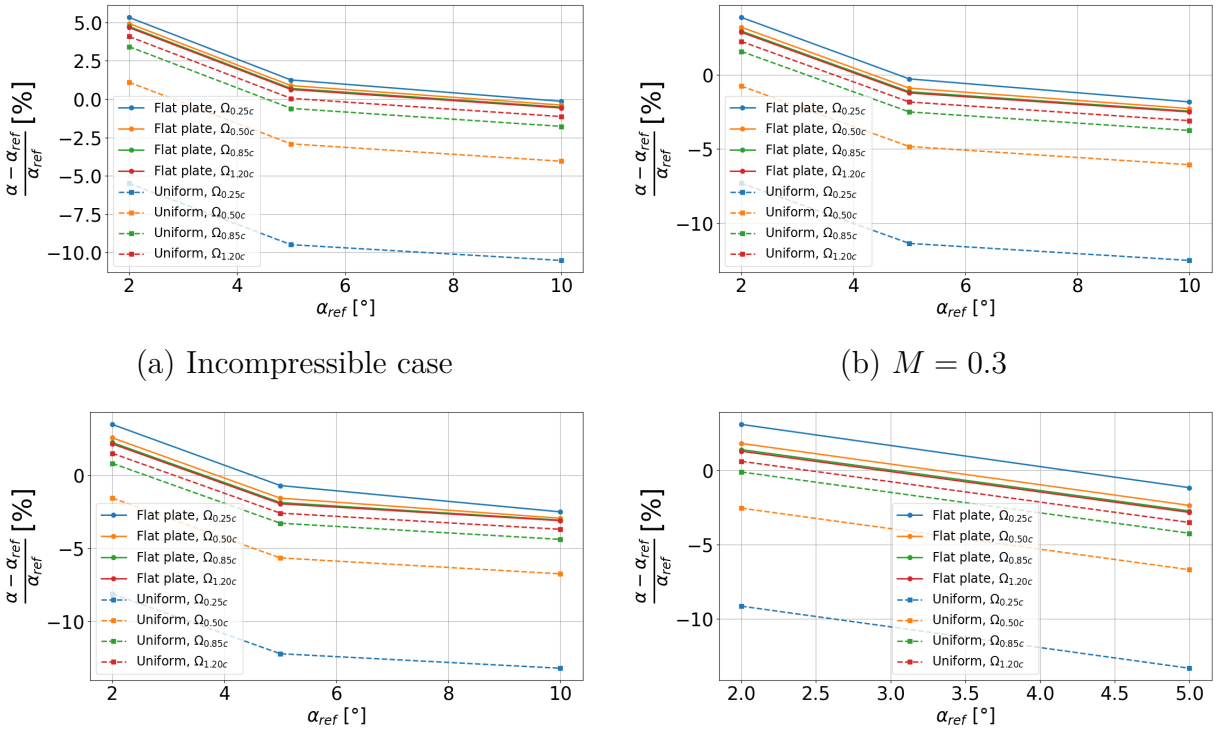
Figure 3.8: Dimensionless tangential velocity jump along the chordwise direction for the $M = 0.4$ and $\alpha = 10°$ case, compared with the theoretical flat-plate distribution.

The tangential velocity jump increases near the leading edge and reaches a local maximum in the vicinity of the shock location before decreasing downstream. This behavior indicates that the shock locally modifies the circulation distribution along the airfoil, leading to deviations from the flat plate circulation distribution.

Although the weak shock observed in the present cases does not strongly degrade the prediction accuracy, stronger compressibility effects could significantly affect the method. If a shock wave intersects the integration contour, the resulting flow discontinuity may affect both the circulation evaluation and the accuracy of the induced velocity reconstruction. Under such conditions, the assumptions underlying the present formulation may no longer remain valid, potentially leading to larger errors in the predicted effective velocity and AoA.

3.3.2 Prediction accuracy of the AoA

The relative error on the predicted AoA is presented for different Mach numbers, circulation models, and contour locations in Figure 3.9.



(a) Incompressible case

(b) $M = 0.3$

(c) $M = 0.4$

(d) $M = 0.5$

Figure 3.9: Relative error on the extracted AoA estimation as a function of α_{ref} for different Mach numbers, circulation models, and contour locations.

Overall, the flat plate circulation model generally provides more accurate AoA predictions than the uniform circulation assumption. This behavior is particularly visible for contours located close to the airfoil, where the uniform distribution produces larger deviations. The discrepancy between the two circulation models progressively decreases as the contour distance increases.

The improved performance of the flat plate circulation model can be explained by its better reproduction of the non uniform circulation distribution. Since the AoA is reconstructed from the direction of the corrected velocity vector, the prediction is highly sensitive to the induced velocity field produced by the assumed circulation distribution.
For the flat plate circulation model, the prediction remains relatively consistent across contour locations, indicating that the circulation variations along the chord are adequately captured.

In contrast, the uniform circulation assumption exhibits a stronger dependence on contour position, particularly for $\Omega_{0.25c}$, where the relative error becomes significantly larger. Since this assumption cannot reproduce the strong circulation gradients near the leading edge, it leads to poorer prediction accuracy for contours located close to the airfoil.

The AoA prediction is consistent with the effective inflow velocity estimation. The $\Omega_{0.25c}$ contour systematically overpredicts the effective inflow velocity magnitude and similarly produces larger reconstructed angles than the other contour locations.

However, despite these larger deviations for the effective velocity, $\Omega_{0.25c}$ provides the smallest relative error on the AoA.

This indicates that, although the velocity magnitude correction remains less accurate close to the airfoil, the reconstructed velocity direction is better captured, leading to a more accurate AoA estimation.

Compressibility effects also influence the prediction accuracy. For compressible conditions and for a fixed AoA, the relative error generally increases with Mach number.

For example, at $\alpha = 10°$, the relative error increases from approximately 2% at $M = 0.3$ to more than 2.5% at $M = 0.4$ for several contour locations. As the Mach number increases, the incompressible induced velocity reconstruction used to estimate $\mathbf{u}_e$ becomes less representative of the actual flow physics. Consequently, the induced velocity correction becomes less accurate, leading to larger errors in the predicted AoA.

The larger relative errors observed for the AoA prediction compared with $\|\mathbf{u}_e\|$ can be explained by the nonlinear dependence of the angle on the velocity components. While the effective inflow velocity magnitude depends on the norm of the corrected velocity vector, the AoA is reconstructed from its direction through an arctangent relationship. Small errors in the velocity components may therefore produce amplified variations in the estimated angle.

3.4 Conclusion

In conclusion, the analysis showed that the circulation distribution plays an important role in the induced velocity reconstruction. The flat plate circulation model provides a more realistic representation of the circulation distribution than the uniform model and generally leads to more accurate AoA predictions. The contour location also affects the prediction accuracy. Contours located farther from the airfoil provide more robust estimations of effective velocity, as the induced velocity field becomes less sensitive to local circulation variations and modelling assumptions. Concerning the AoA prediction, the $\Omega_{0.25c}$ contour generally provides the smaller relative error.

The effective velocity prediction remains only weakly dependent on the assumed circulation distribution, whereas the AoA estimation is more sensitive to the induced velocity reconstruction. The flat-plate circulation model consistently improves the AoA prediction, especially for contours located close to the airfoil. Finally, compressibility effects remain limited within the investigated Mach number range, although prediction errors tend to increase slightly at higher Mach numbers and AoA due to deviations from the incompressible assumptions underlying the correction model.

Chapter 4

Wall-modeled versus wall-resolved RANS simulations

4.1 Introduction

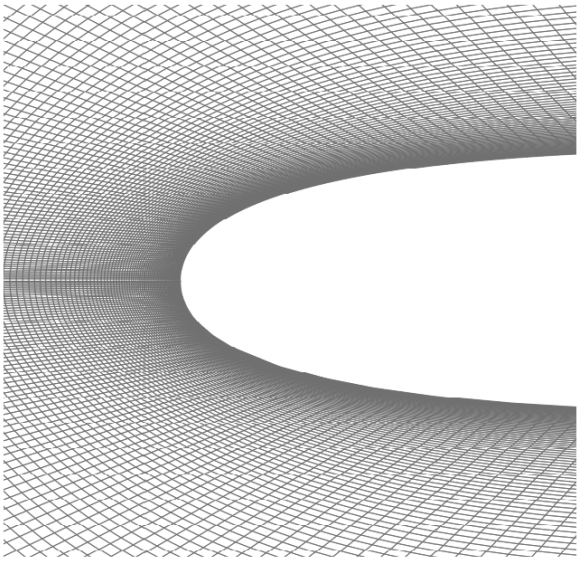
In order to perform three-dimensional simulations at a reasonable computational cost, wall functions are required. These functions model the near-wall behaviour of the flow instead of resolving the viscous sublayer explicitly, allowing larger values of y^+. The reduced near-wall mesh refinement requirements therefore decrease the total cell count and, consequently, the computational cost. [25]

This chapter investigates the differences between wall-modeled and wall-resolved RANS simulations in order to assess whether the wall-function approach significantly affects the quantities of interest.

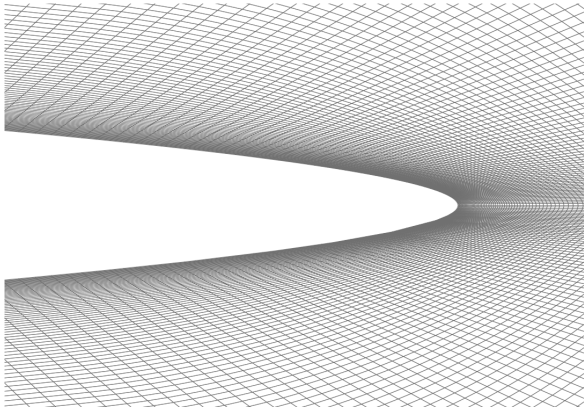
4.2 Mesh

In the previous chapters, the airfoil considered was a blunt NACA0012 profile. Since the mesh exhibited abrupt jumps in cell size, an improved mesh topology was developed. The airfoil used for the improved mesh corresponds to a rounded NACA0012 profile obtained through a Joukowski transformation [26]. The mesh is then generated using the *Ansys Fluent* meshing tool. This geometry modification allows the generation of a mesh without cell size discontinuities.

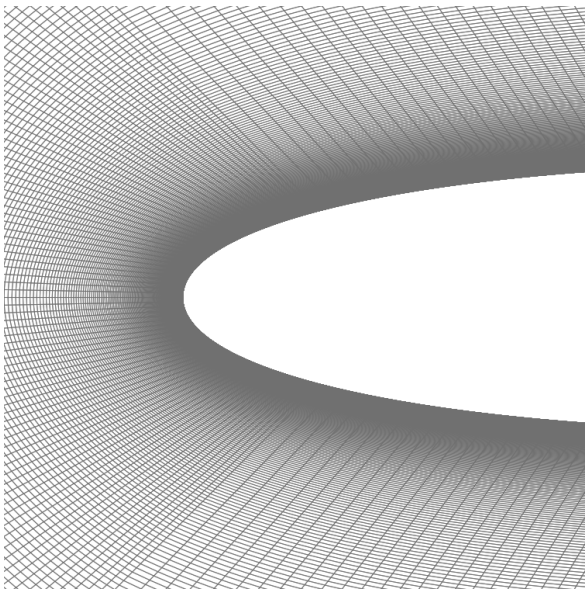
The airfoil geometries near the leading and trailing edges are shown below in order to highlight the differences between the blunt and rounded configurations.



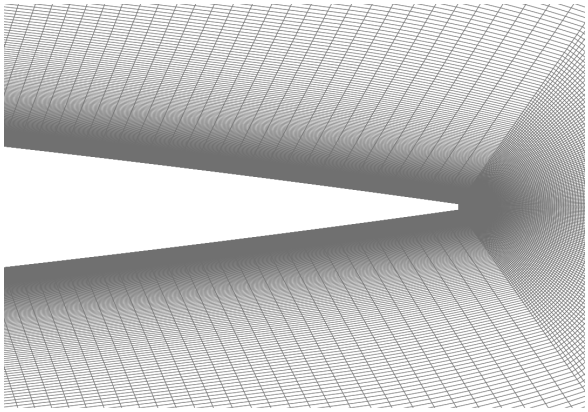
(a) Leading-edge region of the rounded NACA0012 mesh.



(b) Trailing-edge region of the rounded NACA0012 mesh.



(c) Leading-edge region of the blunt NACA0012 mesh.



(d) Trailing-edge region of the blunt NACA0012 mesh.

Figure 4.1: Comparison of the mesh topology in the leading-edge and trailing-edge regions for the rounded and blunt NACA0012 geometries.

Attempts were made to use this smooth topology for the wall-resolved simulations. However, when a sufficiently fine near-wall refinement was imposed around the airfoil, the *Ansys* meshing software was no longer able to generate a valid mesh. For this reason, the wall-resolved simulations presented in the previous chapter were performed using the mesh topology containing partitioning lines. An illustration of the meshing difficulties encountered under excessive refinement is provided in Appendix A.

The resulting mesh topology is shown in Figure 4.2.

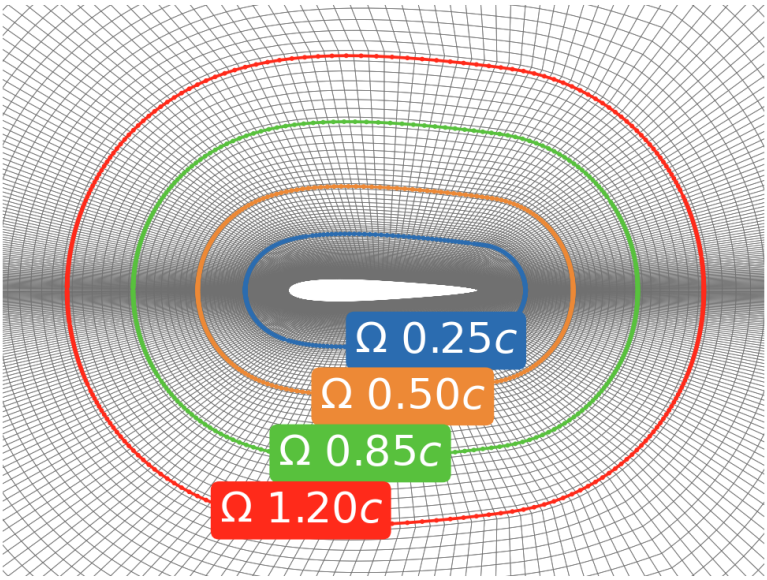


Figure 4.2: Improved mesh in the near-airfoil region together with the iso-distance contours used for the circulation and AoA extraction.

The improved mesh characteristics are summarized in Table 4.1.

Number of nodes	69200
Number of cells	68800
Growth factor	1.037
Maximum cell aspect ratio	174.23

Table 4.1: Improved mesh specifications.

This mesh ensures a smooth evolution of the contour spacing Δs along the iso-distance contours used in the post-processing procedure. The evolution of the contour spacing Δs along the iso-distance contours is shown in Figure 4.3.

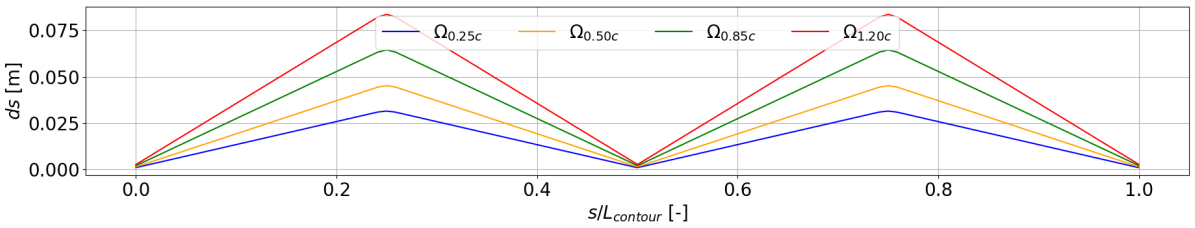


Figure 4.3: Evolution of the curvilinear spacing ds along the different iso-distance extraction contours for the improved mesh.

4.3 Near-wall modeling

The wall-modeled simulations presented in this chapter rely on the automatic near-wall treatment of the k–ω SST turbulence model [12]. This treatment automatically adapts to

the local mesh resolution. For sufficiently fine meshes, the model behaves as a wall-resolved formulation, whereas for coarser meshes it switches to a wall-function formulation.

In the wall-function regime, the viscous sublayer is not explicitly resolved. Instead, the wall shear stress is reconstructed using the semi-empirical law of the wall. Wall functions therefore require the center of the first cell adjacent to the wall to be located in, or sufficiently close to, the logarithmic region of the boundary layer. This typically corresponds to y^+ values between 30 and 300. In the present study, the mesh is generated such that $y^+ \approx 100$, placing the first cell within the recommended wall-function range. [27]

The near-wall velocity profile is modeled using the logarithmic law of the wall:

$$u^+ = \frac{1}{\kappa} \ln\left(y^+\right) + C \tag{4.1}$$

where $u^+ = \frac{u}{u_\tau}$, $y^+ = \frac{\rho u_\tau y}{\mu}$, the von Kármán constant $\kappa = 0.41$, and $C = 5.35$.

In compressible flows, density variations are directly included in the definition of y^+, leading to $y^+ = \frac{\rho_w u_\tau y}{\mu}$. In addition to the logarithmic velocity profile, a thermal wall function is employed to model heat transfer near the wall.

Wall functions rely on the assumption of an equilibrium turbulent boundary layer and may therefore lose accuracy in regions characterized by strong pressure gradients, flow separation or recirculation.

4.4 Comparison between wall-modeled and wall-resolved RANS simulations

In order to assess whether the wall-function approach remains consistent with the wall-resolved reference, several quantities are compared:

- The $u^+(y^+)$ profiles, in order to evaluate whether the wall functions accurately reproduce the boundary layer behavior observed in the wall-resolved simulations.
- The lift and drag coefficients predicted by *Ansys Fluent*
- The circulation, in order to determine whether the observed circulation variations persist without the cell-size discontinuities
- The results of the AoA extraction algorithm, in order to evaluate whether the wall-function approach affects the extracted quantities.

To ensure that the observed differences are not solely caused by changes in the mesh topology, the results obtained with the improved mesh are compared with both the initial coarsened mesh and the wall-resolved reference mesh. The initial coarsened mesh corresponds to the wall-resolved mesh after coarsening in order to match the refinement level of the improved mesh.

4.4.1 $u^+(y^+)$ profiles

In order to assess the behavior of the wall functions, the $u^+(y^+)$ profiles are reconstructed along the same three normals as those used in Fig. 2.6.

The incompressible case at $U_\infty = 88.2$ m/s and $\alpha = 10°$ is first investigated. The compressible case at $M = 0.3$ and $\alpha = 10°$ is also considered, and the corresponding $u^+(y^+)$ profiles are provided in Appendix A.3, since similar conclusions are obtained.

Overall, the wall-function approach provides satisfactory agreement with the wall-resolved results. The wall-modeled profiles reproduce the general behavior of the wall-resolved reference for both mesh configurations.

The slight overestimation of the u^+ profiles observed in the wall-modeled simulations may be related to the constants used in the *Ansys Fluent* law of the wall. The values employed in the wall-functions ($\kappa \approx 0.41$ and $C \approx 5.5$ [12]) differ slightly from the logarithmic behavior observed in the wall-resolved simulations, where $\kappa = 0.385$ and $C = 4.1$ (represented by the black dashed line in Fig.4.4) provide excellent agreement with the wall-resolved profile.

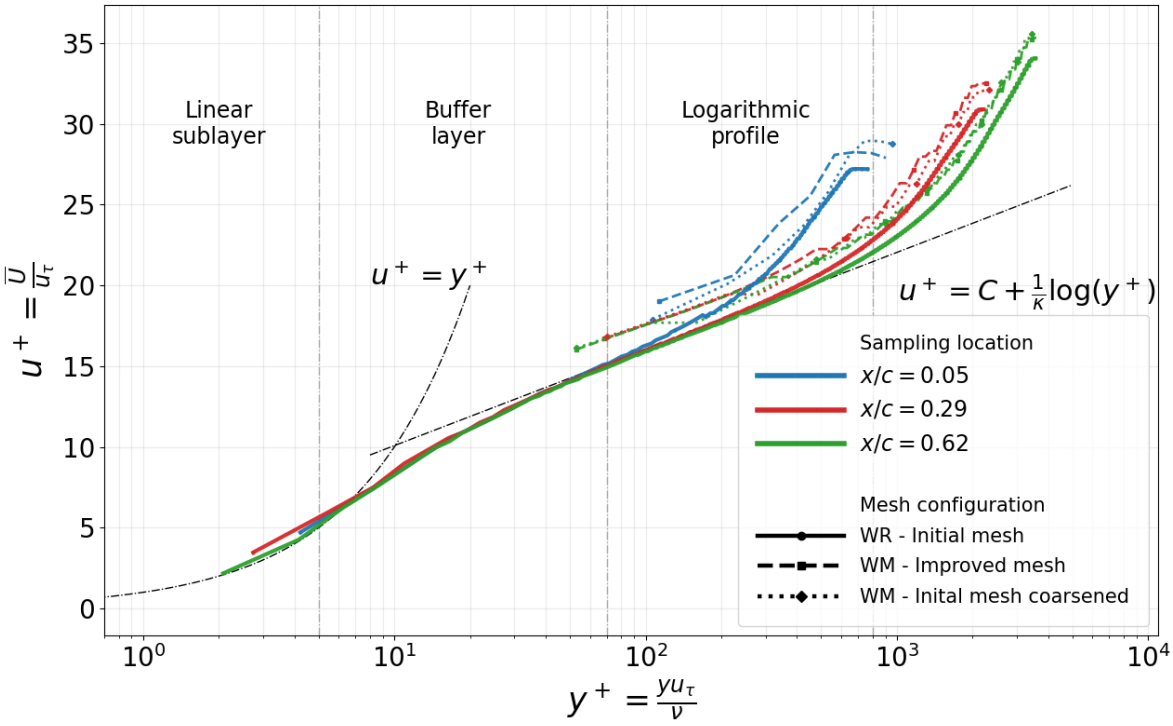


Figure 4.4: Comparison of the dimensionless velocity profiles $u^+(y^+)$ measured along the sampling normals with the theoretical law of the wall profile (black dashed line) for the wall-resolved and wall-modeled configurations.

4.4.2 Aerodynamic coefficients and pressure distribution

In this section, the aerodynamic coefficients and pressure distributions obtained with *Ansys Fluent* are compared for the different mesh configurations.

Compared with the wall-resolved results, the lift coefficient obtained with the improved

mesh is slightly lower. This trend is observed in both the incompressible and compressible cases, as shown in Fig. 4.5 and Fig. 4.6.

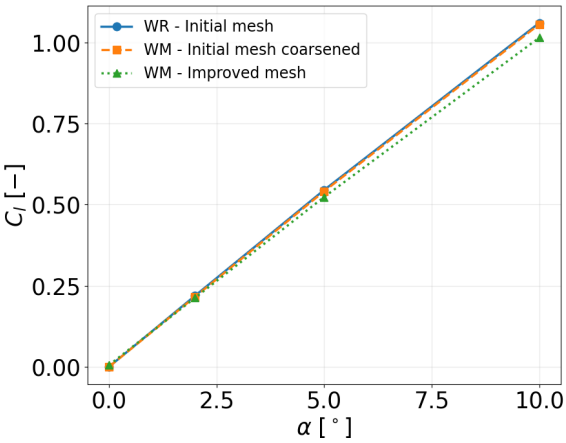


Figure 4.5: Comparison of the lift coefficient predictions obtained with the different mesh configurations for the incompressible cases.

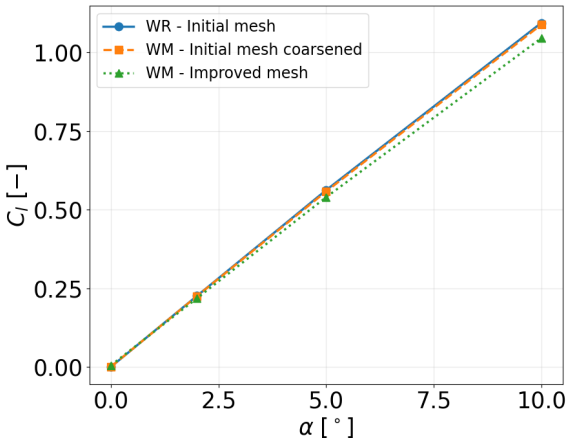


Figure 4.6: Comparison of the lift coefficient predictions obtained with the different mesh configurations for the compressible cases.

The drag coefficient is also investigated since this quantity is generally more sensitive to the near-wall treatment than the lift coefficient. Indeed, the lift coefficient mainly depends on the global pressure distribution around the airfoil, whereas the drag coefficient is strongly influenced by the wall shear stress, the boundary layer, and the local flow separation. Since these quantities are modeled through the wall-function approach, larger discrepancies are expected for the drag coefficient [27].

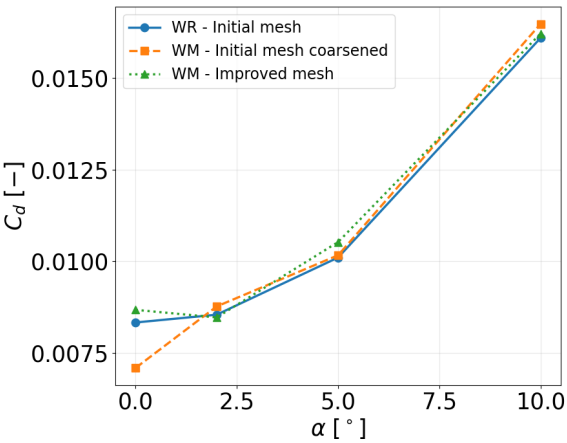


Figure 4.7: Comparison of the drag coefficient obtained with the different mesh configurations for the incompressible cases.

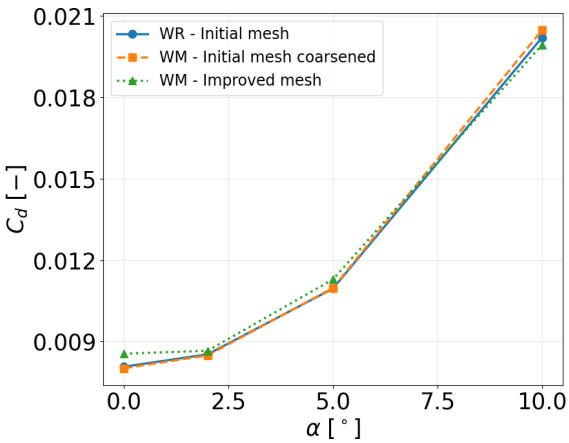


Figure 4.8: Comparison of the drag coefficient obtained with the different mesh configurations for the compressible cases.

Overall, larger discrepancies are observed for the drag coefficient than for the lift coefficient. However, the general trends remain well captured by the wall-modeled simulations for both mesh configurations and flow conditions.

The pressure coefficient is displayed as a function of the normalized curvilinear coordinate

s/c. The coordinate starts at the trailing edge on the intrados, progresses toward the leading edge, and then continues along the extrados back to the trailing edge.

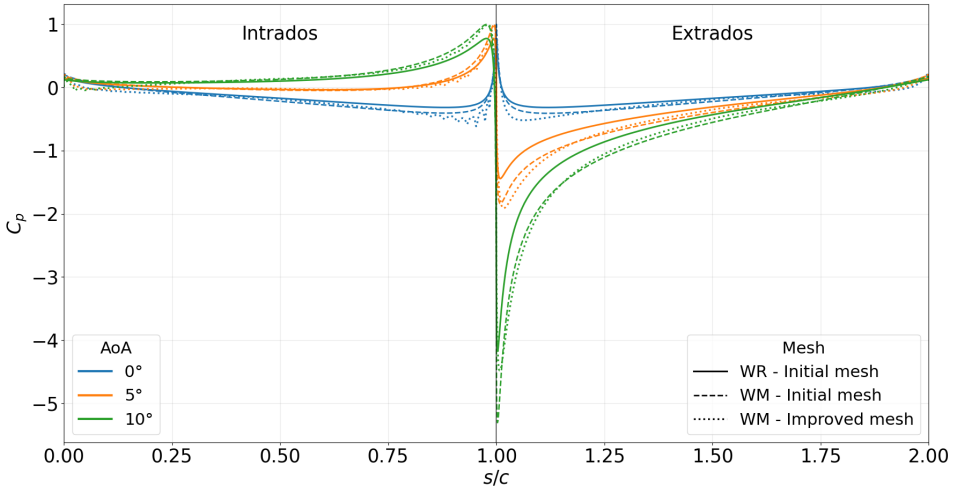


Figure 4.9: Distribution of the pressure coefficient along the dimensionless curvilinear coordinate s/c for the incompressible cases at angles of attack of 0°, 5°, and 10°.

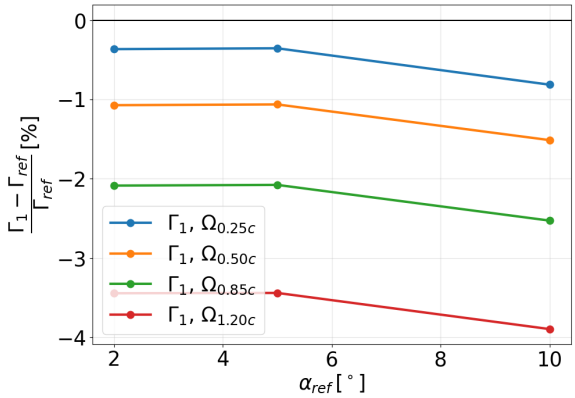
Overall, the pressure distributions remain in good agreement across the different mesh configurations. The largest discrepancies are mainly observed near the leading edge, where the geometric differences locally modify the pressure gradients.

As mentioned previously, the airfoil geometries are not identical for the different mesh configurations. Consequently, part of the discrepancies observed in both the aerodynamic coefficients and the pressure distributions can be attributed to the geometric differences between the blunt and rounded airfoil geometries.

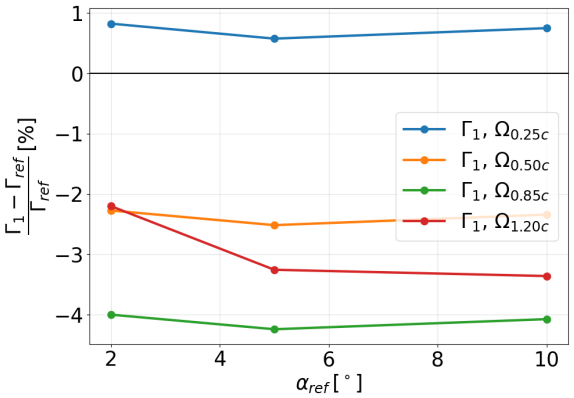
4.4.3 Circulation variations

In this section, the circulation variations along the iso-distance contours are analyzed. The unphysical circulation variations remain present for both the incompressible and compressible cases with the improved mesh. As discussed previously, these fluctuations were initially attributed to spurious vorticity generated by the abrupt cell-size discontinuities present in the initial mesh.

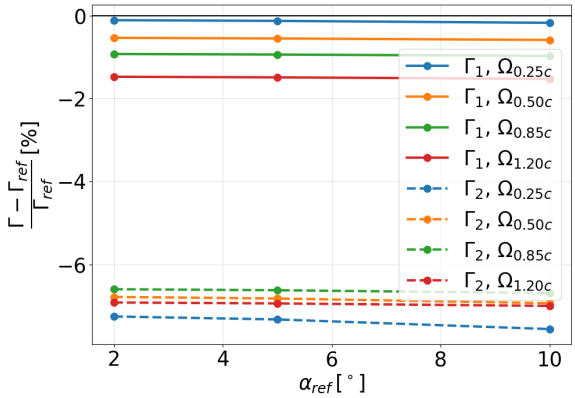
However, similar circulation variations are still observed with the improved mesh topology. Although this configuration does not contain cell-size discontinuities, the circulation is not fully conserved across the different extraction contours. This indicates that the observed behaviour cannot be attributed solely to mesh induced spurious vorticity enclosed between the extraction contours.



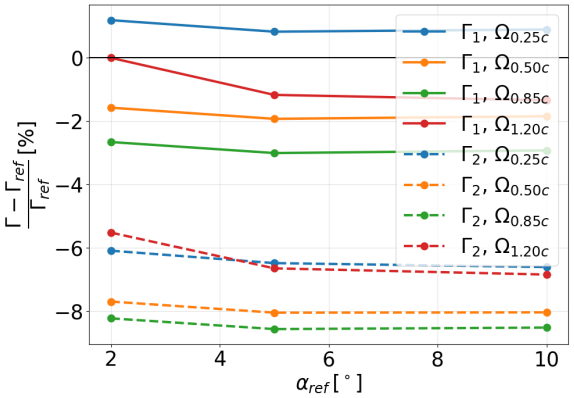
(a) Initial coarsened mesh in the incompressible cases.



(b) Improved mesh in the incompressible cases.



(c) Initial coarsened mesh in the compressible cases ($M_\infty = 0.3$).



(d) Improved mesh in the compressible cases ($M_\infty = 0.3$).

Figure 4.10: Relative circulation difference with respect to the reference wall-resolved solution for the different mesh configurations and flow conditions.

To further investigate this behaviour, the dimensionless vorticity field is analyzed. Small regions of residual vorticity remain visible outside the boundary layer, even with the improved mesh topology. Moreover, the amplitude of the circulation variations is larger than in the wall-resolved reference case, and the improved mesh exhibits slightly larger fluctuations than the initial coarsened mesh.

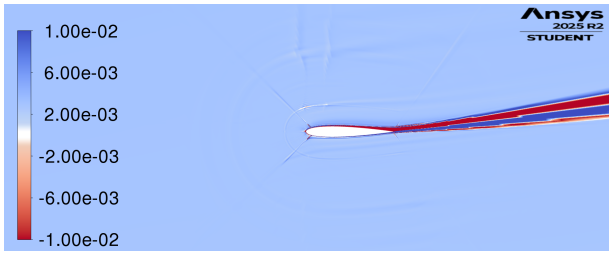


Figure 4.11: Dimensionless vorticity field $\omega_z c/U_\infty$ obtained with the initial coarsened mesh in the incompressible case ($U_\infty = 88.2$ m/s, $\alpha = 10°$).



Figure 4.12: Dimensionless vorticity field $\omega_z c/U_\infty$ obtained with the improved mesh in the incompressible case ($U_\infty = 88.2$ m/s, $\alpha = 10°$).

These observations suggest that the circulation fluctuations are not exclusively caused by the mesh induced vorticity associated with cell-size discontinuities. Part of the residual vorticity may also originate from the turbulence modelling assumptions used in the RANS formulation. As described in Section 2.2.1, the $k-\omega$ SST model closes the Reynolds stresses using the Boussinesq approximation and introduces a turbulent viscosity μ_t in the effective stress tensor, Eq. (2.7).

This additional turbulent viscosity may therefore contribute to artificial dissipation. In regions with strong velocity gradients, such as the boundary layer and the wake, the model may locally increase the eddy viscosity, which can enhance the diffusion of boundary layer or wake vorticity. This mechanism may therefore contribute to the residual vorticity observed in regions that would ideally remain nearly irrotational [28]. Although these contributions remain small, they can still affect the circulation when integrated along the extraction contours.

Consequently, the observed circulation variations are likely the result of a combined effect of mesh induced errors and turbulence modelling effects associated with the RANS simulations, rather than a purely mesh induced phenomenon. However, this interpretation remains a hypothesis, since the present results do not allow the origin of the observed discrepancies to be identified.

4.4.4 Comparison of the AoA extraction results

In this section, the results of the extraction algorithm obtained for both mesh configurations are compared with the wall-resolved reference solutions. To avoid overloading the discussion with additional figures, only the incompressible case is discussed here. The corresponding results for the compressible case are provided in Appendix A. Similar conclusions are obtained for both flow regimes.

For the initial coarsened mesh, the wall-function approach provides overall good agreement with the wall-resolved reference results. Under the uniform circulation assumption, both the relative error on the extracted AoA and on the effective velocity magnitude $||u_e||$ remain close to the wall-resolved results. With the flat plate circulation assumption, the effective velocity magnitude remains accurately predicted, while the relative error on the AoA is slightly reduced.

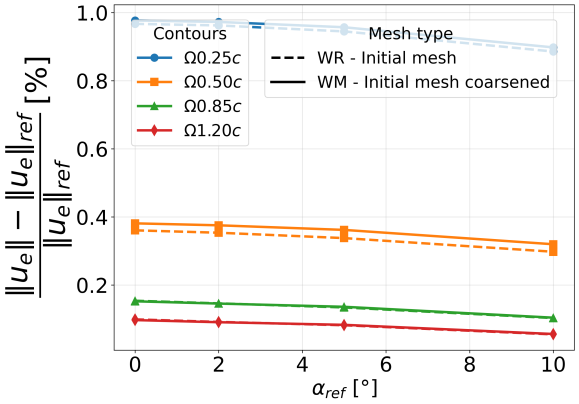
For the improved mesh, the agreement with the wall-resolved reference also remains satisfactory. Under the uniform circulation assumption, the general trends remain similar, but the first contour exhibits lower relative errors for both the effective velocity magnitude and the extracted AoA.

This may be due to a reduction of mesh induced spurious vorticity in the vicinity of the airfoil, since the improved mesh does not contain abrupt cell-size jumps. In the wall-resolved mesh, this mesh induced spurious vorticity was mainly located within the region enclosed by the closest contour. Reducing this contribution may therefore improve the prediction obtained from this contour.

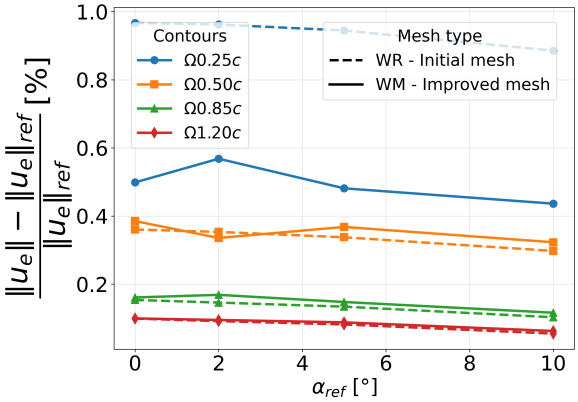
With the flat plate assumption, the relative error on $||u_e||$ follows trends similar to those observed in the wall-resolved case, while providing improved predictions for the first contour. Lower relative errors are also obtained for the extracted AoA compared to the

wall-resolved case.

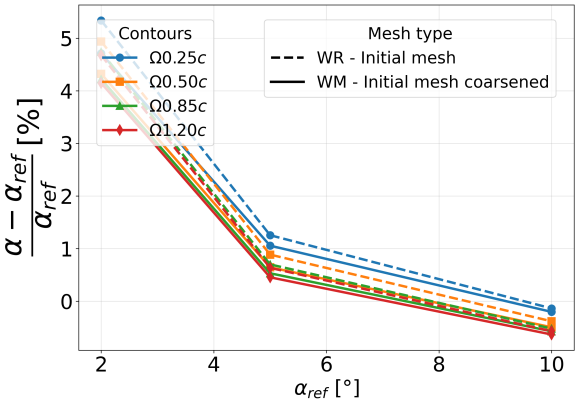
Overall, the wall-function approach provides satisfactory results for both mesh configurations, and the extraction algorithm remains consistent with the wall-resolved reference quantities.



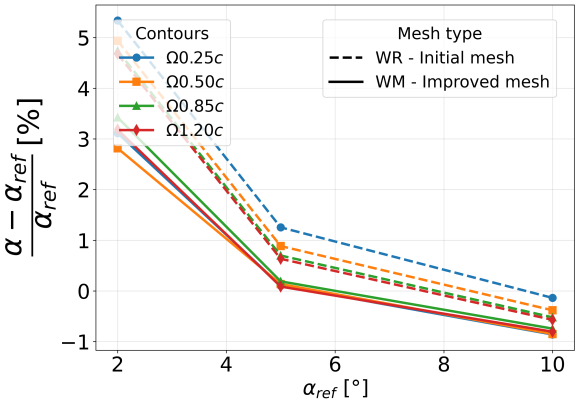
(a) Relative error in the effective velocity magnitude $||u_e||$ for the initial coarsened mesh.



(b) Relative error in the effective velocity magnitude $||u_e||$ for the improved mesh.

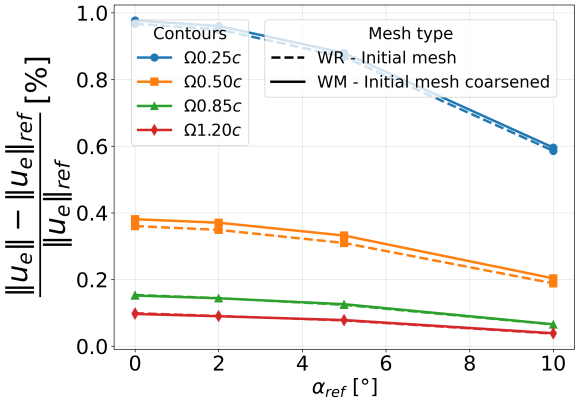


(c) Relative AoA error for the initial coarsened mesh.

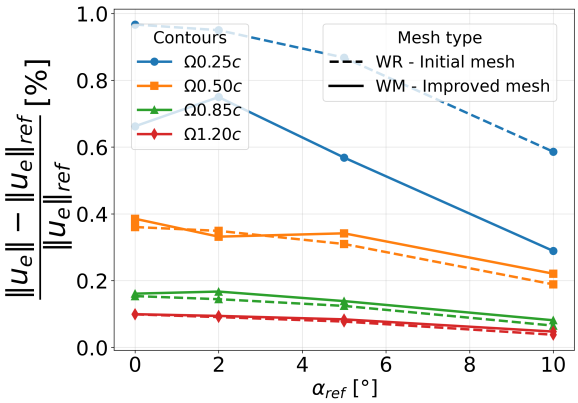


(d) Relative AoA error for the improved mesh.

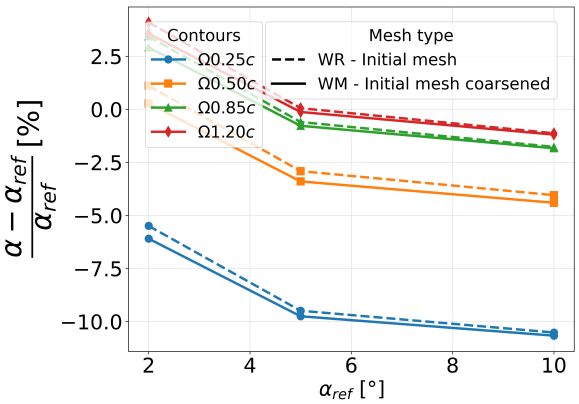
Figure 4.13: Comparison with the wall-resolved reference for the incompressible case using the flat-plate assumption: relative error in the effective velocity magnitude $||u_e||$ (top) and relative AoA error (bottom) for both mesh configurations.



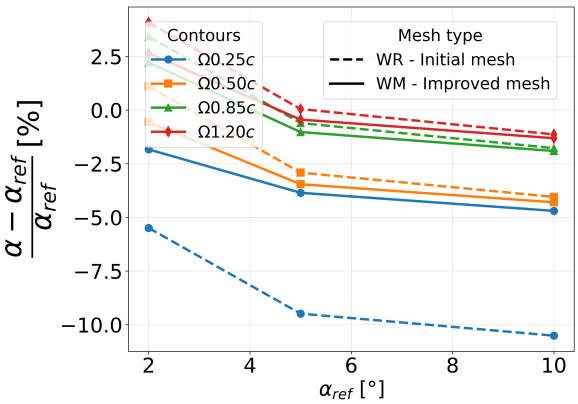
(a) Relative error in the effective velocity magnitude $||u_e||$ for the initial coarsened mesh.



(b) Relative error in the effective velocity magnitude $||u_e||$ for the improved mesh.



(c) Relative AoA error for the initial coarsened mesh.



(d) Relative AoA error for the improved mesh.

Figure 4.14: Comparison with the wall-resolved reference for the incompressible case using the uniform circulation assumption: relative error in the effective velocity magnitude $||u_e||$ (top) and relative AoA error (bottom) for both mesh configurations.

4.5 Conclusion

Overall, the wall-function approach combined with the improved mesh topology provides satisfactory agreement with the wall-resolved reference simulations.

The wall-modeled simulations correctly reproduce the main aerodynamic trends observed in the wall-resolved simulations. The $u^+(y^+)$ profiles remain in reasonably good agreement with the wall-resolved reference profiles, and the aerodynamic coefficients and pressure distributions are accurately captured despite small discrepancies associated with the near-wall modeling and the geometric differences between the blunt and rounded airfoil geometries.

Although the drag coefficient exhibits larger deviations than the lift coefficient, the overall aerodynamic behavior remains consistently reproduced. The circulation analysis also shows that the unphysical circulation fluctuations persist despite the absence of the cell-size

discontinuities in the improved mesh. This suggests that the observed variations are not solely caused by the mesh topology and may also be influenced by turbulence modelling effects associated with the RANS formulation.

Finally, the AoA extraction algorithm remains robust when applied to the wall-modeled simulations. Both the effective velocity magnitude and the extracted AoA remain in satisfactory agreement with the wall-resolved reference results and even exhibit improved predictions compared to the wall-resolved case when using the $\Omega_{0.25c}$ contour.

Consequently, despite the small discrepancies observed throughout the analysis, the wall-function approach combined with the improved mesh topology is considered sufficiently accurate for the subsequent three-dimensional simulations.

Chapter 5

AoA extraction from 3D wall-modeled RANS simulations

5.1 Introduction

The post-processing methodology presented in Chapter 3 can also be applied to three-dimensional CFD simulations. Velocity, density and pressure fields are extracted along iso-distance contours surrounding the airfoil in the spanwise direction. Each spanwise section is then treated as a two-dimensional plane, and the methodology is applied independently to each extracted plane [3].

The initial objective of this work was to generate a three-dimensional mesh of the S-76 rotor blade, including the blade tip responsible for the generation of tip vortices [6]. Several meshing strategies and Python-based geometrical generation approaches were investigated [29]. However, generating a structured mesh around the blade tip could not be achieved satisfactorily in the present work.

An alternative approach was therefore adopted in order to still investigate blade–vortex interaction phenomena. Instead of explicitly meshing the rotor tip, counter-rotating vortices were imposed at the inlet of the computational domain. These imposed vortices are intended to reproduce the flow perturbations associated with blade–vortex interactions.

The computational domain considered in this study consists of a spanwise extruded NACA0012 wing. As discussed in Chapter 4, the near-wall region is modeled using wall functions.

5.2 Numerical set-up

This section describes the three-dimensional computational domain, the boundary conditions, and the adaptive mesh refinement strategy used for the simulations.

5.2.1 Mesh and computational domain

The improved two-dimensional mesh presented previously was extruded along the spanwise direction over a span of two chord lengths to generate the three-dimensional mesh shown in Figure 5.3.

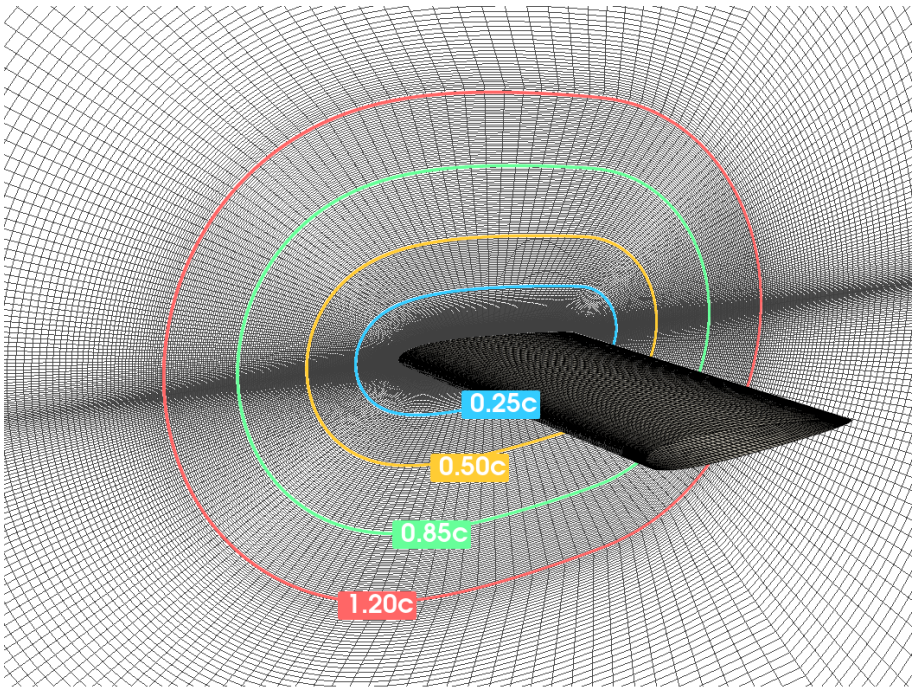


Figure 5.1: Three-dimensional structured mesh and iso-distance contours used for the circulation and AoA extraction.

The mesh contains 80 spanwise divisions, and the specifications of each spanwise segment are provided in Table 4.1. The computational mesh consists of 2.12×10^7 nodes and 5.22×10^6 hexahedral cells.

5.2.2 Boundary conditions

Symmetry boundary conditions are imposed on the lateral boundaries of the computational domain. These conditions enforce zero normal velocity and zero normal gradients of all variables at the symmetry planes. As a result, no flux crosses the lateral boundaries and the shear stress vanishes, making the condition equivalent to a slip-wall boundary condition [17].

In order to reproduce a blade–vortex interaction configuration, two counter-rotating vortices are imposed at the inlet boundary. As discussed with Pr. Winckelmans, the contribution of the image vortices must also be included in order to ensure consistency with the imposed symmetry planes. The imposed velocity field therefore includes both the two physical vortices located inside the computational domain and the contribution of their images across the symmetry planes.

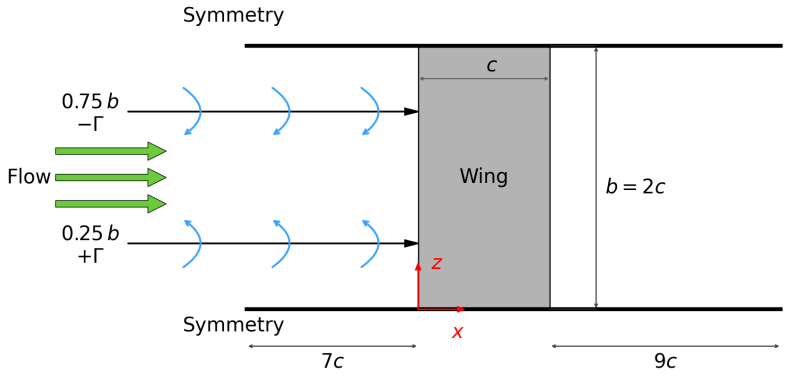


Figure 5.2: Schematic representation of the three-dimensional configuration and inlet boundary conditions viewed from above.

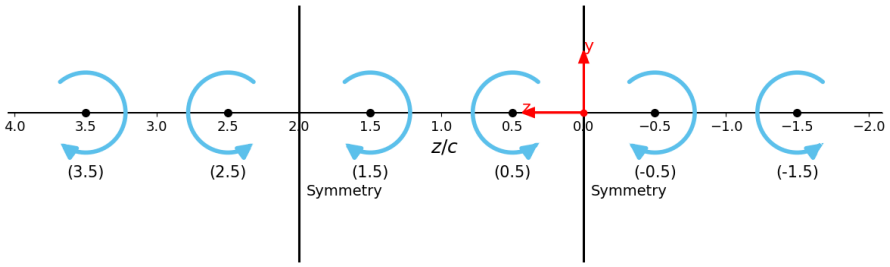


Figure 5.3: Spanwise locations and rotation directions of the counter-rotating vortices imposed at the inlet boundary.

The two physical vortices are imposed at the inlet plane with spanwise positions $z/c = 0.5$ and $z/c = 1.5$, where c denotes the wing chord. The image vortices are located at $z/c = -0.5$, $z/c = -1.5$ and $z/c = 2.5$, $z/c = 3.5$, symmetrically with respect to the planes $z/c = 0$ and $z/c = 2$, respectively.

Two vortex–wing interaction are investigated. In the first configuration, the imposed vortices convect below the wing without directly interacting with its surface. In the second configuration, the vortices directly interact with the wing.

In the first configuration, the vortex centers are imposed at $y/r_c = -2$ at the inlet, where r_c denotes the vortex core radius defined below. In the second configuration, the vortex centers are initially imposed at $y/r_c = 0$.

The two configurations therefore differ only by the initial vertical position of the imposed vortices at the inlet.

The vortex characteristics are determined from the NASA S-76 HVAB experimental database[30].

Table 5.1: Experimental tip vortex and flow characteristics extracted from the NASA S-76 HVAB database.

c_{exp} (m)	$U_{\infty,\mathrm{exp}}$ (m/s)	ν_{exp} (m^2/s)	$r_{c,\mathrm{exp}}$ (mm)	Γ_{exp} (m^2/s)
0.127	202.85	1.473×10^{-5}	12.63	4.15

Since the chord length differs between the experimental configuration and the present simulations, the vortex properties must be rescaled. The scaling procedure is based on preserving both the chord Reynolds number and the circulation Reynolds number, as well as their ratio Re_Γ/Re_c.

In the present simulations, the freestream velocity is set to 102 m/s and the chord length to 1 m. The circulation is therefore modified in order to preserve the same Reynolds number ratio, leading to:

$$\Gamma_{\mathrm{sim}} = \Gamma_{\mathrm{exp}} \frac{U_{\infty,\mathrm{sim}}\, c_{\mathrm{sim}}}{U_{\infty,\mathrm{exp}}\, c_{\mathrm{exp}}} = 16.1 \text{ m}^2/\text{s}. \tag{5.1}$$

The kinematic viscosity is then adjusted to preserve the same circulation Reynolds number, resulting in $\nu_{\mathrm{sim}} = 5.729 \times 10^{-5}$ m^2/s.

The resulting Reynolds numbers are therefore:

$$Re_{c,\mathrm{sim}} = Re_{c,\mathrm{exp}} = 1.75 \times 10^6, \qquad Re_{\Gamma,\mathrm{sim}} = Re_{\Gamma,\mathrm{exp}} = 2.82 \times 10^5. \tag{5.2}$$

The vortex core radius is similarly rescaled. The dimensionless ratio r_c/c is preserved during the scaling process, yielding:

$$r_{c,\mathrm{sim}} = r_{c,\mathrm{exp}} \frac{c_{\mathrm{sim}}}{c_{\mathrm{exp}}} = 99.45 \text{ mm} \tag{5.3}$$

The resulting dimensionless spanwise ratio is:

$$\frac{r_c}{b} = 0.05.$$

The imposed inlet velocity field is defined as the superposition of the freestream velocity U_∞, the velocity induced by the two physical vortices, and the velocity induced by their image vortices. The vortices are modeled using a Lamb–Oseen velocity distribution [31]:

$$V_\theta(r) = \frac{\Gamma}{2\pi r}\left(1 - \exp\left[-\alpha\left(\frac{r}{r_c}\right)^2\right]\right) \tag{5.4}$$

The radial distance to vortex i is defined as $r_i = \sqrt{(y-y_i)^2 + (z-z_i)^2}$.

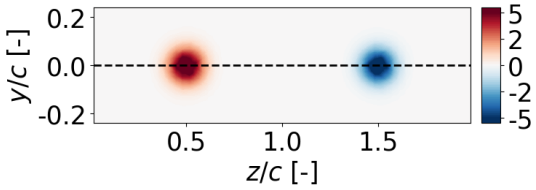
5.2.3 Adaptive mesh refinement

As the imposed vortices convect from the inlet toward the wing over a streamwise distance of $7c$, insufficient mesh resolution may lead to significant numerical diffusion and could

progressively alter the vortex structures. Under such conditions, the vortices become more diffuse before interacting with the wing. This affects the resulting blade–vortex interaction.

To limit this effect, adaptive mesh refinement (AMR) is employed. The refinement strategy is based on a geometric criterion centered on the vortex cores. Cells located inside the vortex regions are locally refined through cell subdivision, allowing sharper velocity gradients to be maintained during vortex convection. The effect of AMR can therefore be assessed by comparing the dimensionless streamwise vorticity field $\omega_x c/U_\infty$ at the inlet and near the wing, both with and without adaptive mesh refinement.

Figure 5.4: Dimensionless streamwise vorticity field, $\omega_x c/U_\infty$, imposed at the inlet plane located at $x/c = -7$.



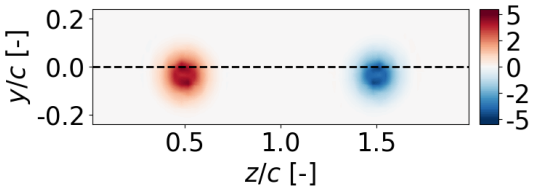


Figure 5.5: Dimensionless streamwise vorticity field, $\omega_x c/U_\infty$, in the plane located at $x/c = -0.5$ without AMR.

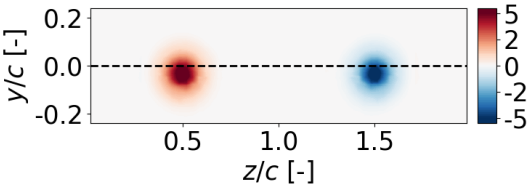


Figure 5.6: Dimensionless streamwise vorticity field, $\omega_x c/U_\infty$, in the plane located at $x/c = -0.5$ with AMR.

First, the vortices initially imposed at $y/c = 0$ at the inlet are no longer centered at the same vertical position in the plane located at $x/c = -0.5$. This displacement results from the mutual induced velocity of the two counter-rotating vortices, which produces a downward convection of the vortex pair.

The comparison between Fig. 5.5 and Fig. 5.6 highlights the strong influence of mesh refinement on vortex preservation. Without AMR, the vortices undergo significant numerical diffusion during their downstream convection.

In contrast, the use of AMR considerably improves vortex preservation during convection toward the wing. The reduction of numerical diffusion therefore allows the vortex–wing interaction to be captured more accurately.

The use of adaptive mesh refinement is therefore essential to preserve the imposed vortex structures during convection and maintain physically coherent vortex–wing interactions.

5.3 Results

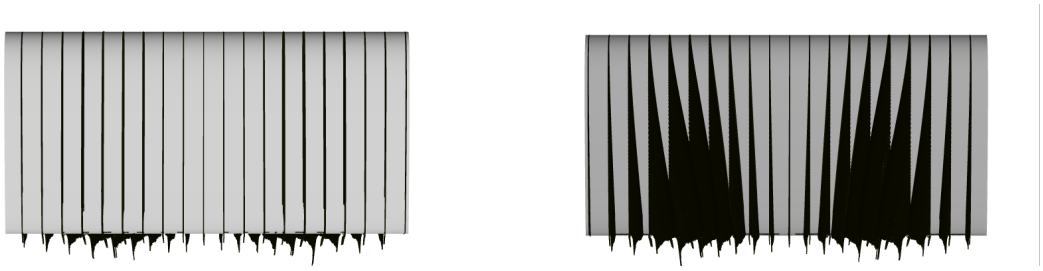
This section presents the results obtained for the two investigated vortex–wing interaction configurations. In the first configuration, the imposed vortices convect below the wing, whereas in the second configuration they directly interact with the wing surface.

For each case, the vortex-wing interaction is first analyzed, followed by the lift coefficient predicted for each spanwise section. Finally, the quantity $\alpha - C_l/a_0$ is investigated. Since the present configurations are three-dimensional, the AoA and the effective velocity cannot be defined as unambiguously as in a two-dimensional reference case. Therefore, the AoA distributions shown in Figs. 5.17 and 5.29 should be interpreted as spanwise distributions of the reconstructed AoA. For each spanwise section, this reconstructed AoA is defined as the angle between the local airfoil chord and the reconstructed effective velocity.

5.3.1 Case 1: Vortices convecting below the wing

Flow topology and vortex-wing interaction

In this configuration, the imposed counter-rotating vortex pair primarily convects below the wing. Nevertheless, the induced velocity field generated by the vortices still modifies the local flow topology, particularly on the pressure side of the wing. This behavior is first illustrated by the surface streamlines shown in Fig. 5.7.



(a) Suction side (b) Pressure side

Figure 5.7: Surface streamlines on both sides of the wing.

The suction side remains only weakly affected by the imposed vortical structures, whereas the pressure side exhibits a pronounced spanwise deviation of the streamlines toward the center of the domain. To better visualize the three-dimensional flow topology, streamlines in the vicinity of the wing are displayed in Fig. 5.8 and 5.9.

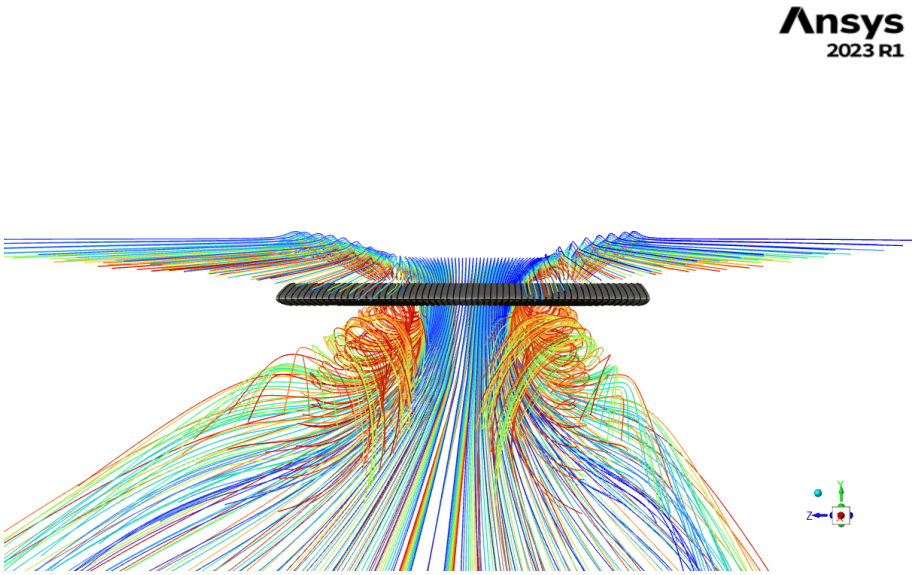


Figure 5.8: Three-dimensional streamlines for case 1, viewed from downstream.

The streamlines shown in Fig. 5.8 originate from the inlet in the region $-0.1 \leq y/c \leq 0.1$, in order to visualize the flow structures convected toward the wing.

The downstream view shows that, although the vortex pair mainly convects below the wing, its induced velocity field still interacts with the pressure side. In the region located between the two counter-rotating vortices, the induced velocity is directed downward, which produces a clear deflection of the streamlines below the wing. On the lateral sides of the vortex pair, the positive induced vertical velocity is observed, with streamlines being redirected upward and passing around the suction side of the wing. The upward and downward velocity regions are also visible from the top view, as shown in Fig. 5.9.

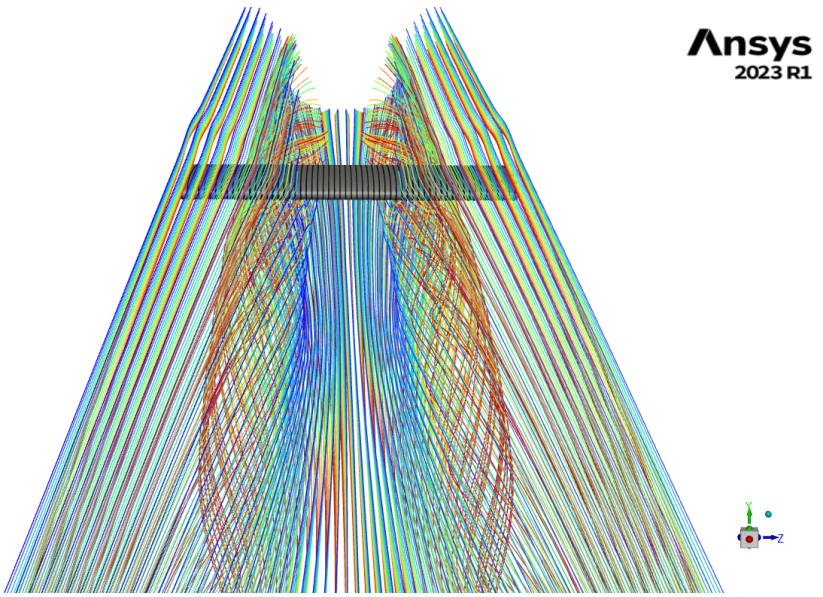
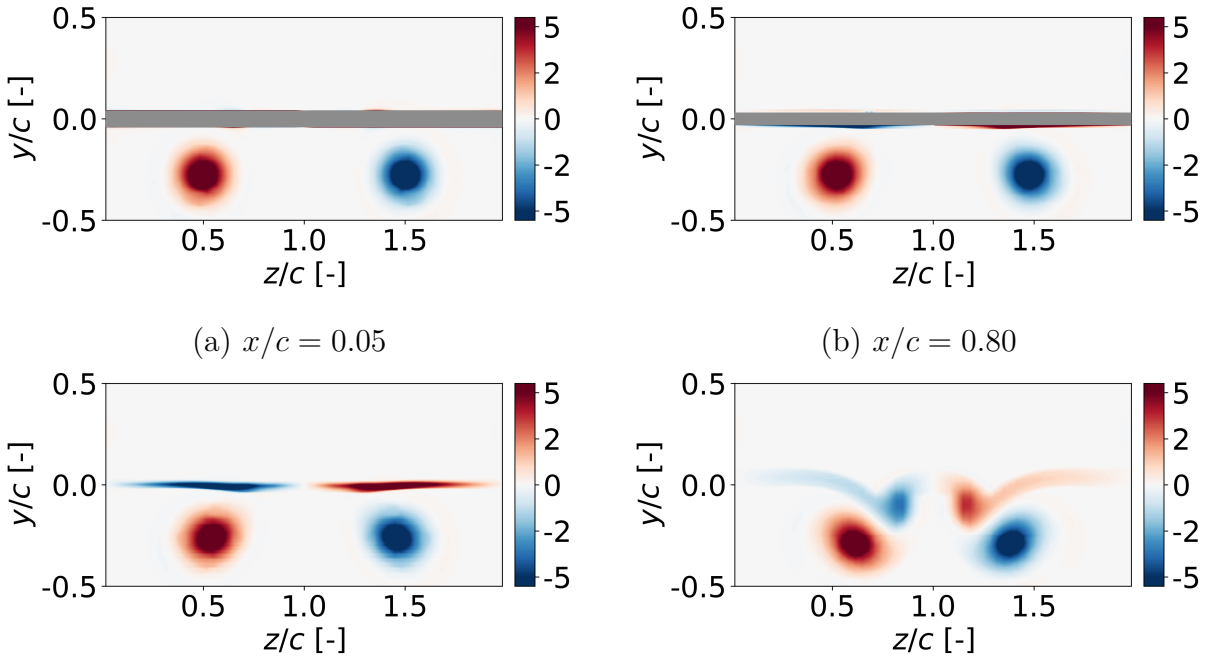


Figure 5.9: Three-dimensional streamlines for case 1, viewed from upstream and above.

The vortex–wing interaction can be further analyzed through the dimensionless streamwise

vorticity field extracted in successive yz planes downstream of the airfoil, as shown in Fig. 5.10. These planes illustrate the progressive evolution of the imposed counter-rotating vortices along the streamwise direction.



(a) $x/c = 0.05$

(b) $x/c = 0.80$

(c) $x/c = 1.40$

(d) $x/c = 2.00$

Figure 5.10: Dimensionless streamwise vorticity, $\omega_x c/U_\infty$, contours in successive yz planes downstream of the airfoil for streamwise locations ranging from $x/c = 0.05$ to $x/c = 2.00$. The figures illustrate the downstream evolution of the imposed counter-rotating vortex structures.

Close to the leading edge ($x/c = 0.05$), the imposed vortices remain relatively compact and only weakly affected by the wing. Further downstream, the interaction with the wake progressively alters the vortex topology. The wake vorticity interacts with the imposed vortices, leading to a gradual displacement of the vortex cores.

As the flow evolves downstream, the initially compact vortical structures progressively wrap around the wake vorticity generated by the wing. This behavior highlights the coupled interaction between the imposed vortices and the wing wake. The vortex induced velocity field modifies the local effective incidence along the span, while the wing wake simultaneously perturbs the imposed vortical structures.

Impact on lift coefficient estimation

The lift coefficient of each section was estimated from the circulation using the Eq. 2.15. As expected, due to the downward velocity induced by the vortices in the central part of the wing, the lift coefficient decreases locally.

Figure 5.11 presents the spanwise evolution of the lift coefficient obtained from the different contours. Among all contours, only the $\Omega 0.25c$ contour provides a reasonably accurate prediction of the reference lift coefficient obtained from the *Ansys Fluent* solution. As the

contour distance from the airfoil increases, the predicted lift progressively deviates from the reference solution and exhibits increasingly pronounced oscillations.

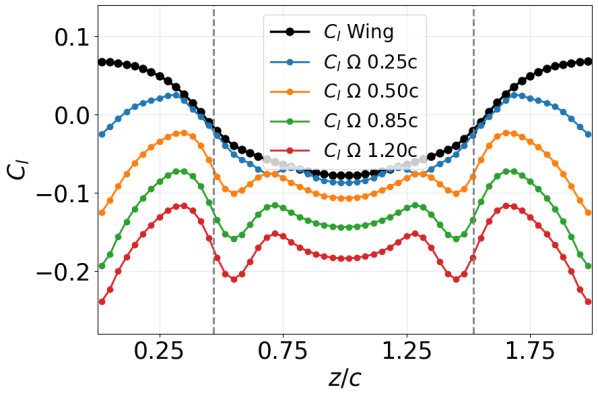


Figure 5.11: Spanwise evolution of the lift coefficient extracted from the different iso-distance contours. The vertical dashed lines indicate the spanwise locations of the imposed vortices.

First, the accuracy of the lift coefficient estimation decreases as the extraction contour is moved farther away from the airfoil. The vorticity fields shown in Fig. 5.13 indicate that the different contours do not enclose exactly the same amount of spanwise vorticity ω_z. This modifies the extracted circulation and therefore introduces an offset in the lift coefficient predicted from the Kutta–Joukowski relation.

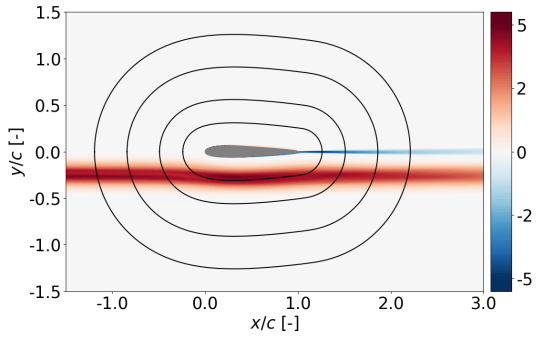


Figure 5.12: (a) Dimensionless streamwise vorticity $\omega_x c/U_\infty$ in the $z/c = 0.50$ yx plane

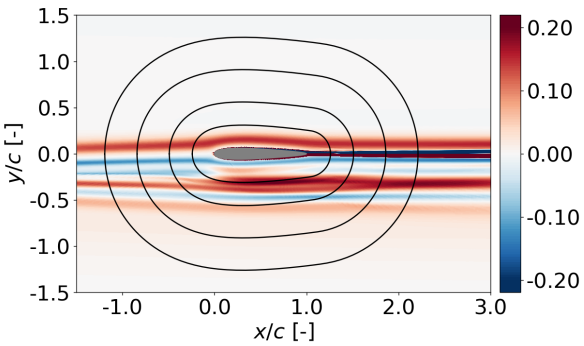


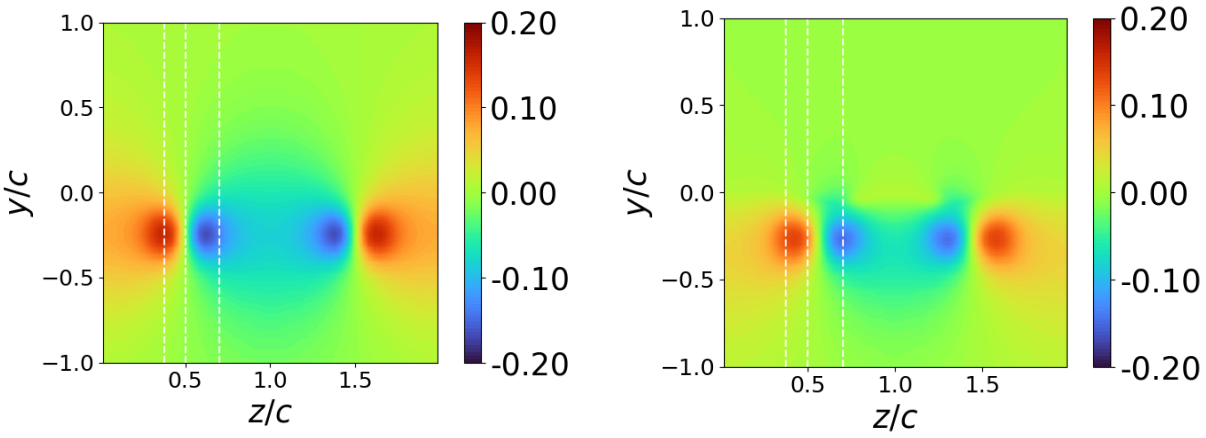
Figure 5.13: (b) Dimensionless spanwise voritcity $\omega_z c/U_\infty$ in the $z/c = 0.50$ yx plane

Figure 5.14: Dimensionless spanwise and streamwise vorticity field in the yx plane. The black line indicates the extraction contours.

Secondly, the oscillatory behavior observed in the lift distribution for the different contours is directly related to the downstream displacement of the vortices induced by the wing–vortex interaction. As shown previously, the vortex cores are progressively displaced toward the center of the domain while interacting with the wing wake. This displacement modifies the spatial distribution of the vertical velocity component intercepted by the extraction contours. Depending on the spanwise location, the leading and trailing edges of a given contour may intersect regions characterized by different induced vertical velocities. These

local imbalances modify the circulation integrated along the contour, thereby producing local increases or decreases in the predicted lift coefficient.

To illustrate this mechanism, the dimensionless vertical velocity field extracted in the yz planes located at $x/c = -1.20$ and $x/c = 2.20$ is shown in Fig. 5.15.



(a) $x/c = -1.20$

(b) $x/c = 2.20$

Figure 5.15: Dimensionless vertical velocity field v/U_∞ in the yz plane upstream and downstream of the airfoil. White dashed lines indicate the spanwise locations of extrema in the predicted lift coefficient: $z/c = 0.375$, 0.5, and 0.7.

For instance, at $z/c \approx 0.375$, the extraction contour intersects near the leading edge a region characterized by a strong positive vertical velocity induced by the vortex. Further downstream, the positive vertical velocity intercepted near the trailing edge becomes weaker. As a consequence, the circulation contribution associated with the leading edge region dominates, resulting in a local increase of the circulation and therefore of the predicted lift coefficient.

Conversely, at $z/c \approx 0.50$, the contour passes through the vortex core near the leading edge, where the induced vertical velocity is close to zero, while the trailing edge still intersects a region characterized by positive vertical velocity. This opposite imbalance reduces the circulation extracted along the contour and therefore produces a local decrease in the predicted lift coefficient.

The accuracy of the $\Omega 0.25c$ contour can be further evaluated by considering the difference between the reference *Ansys Fluent* lift coefficient and the prediction obtained from the contour extraction.

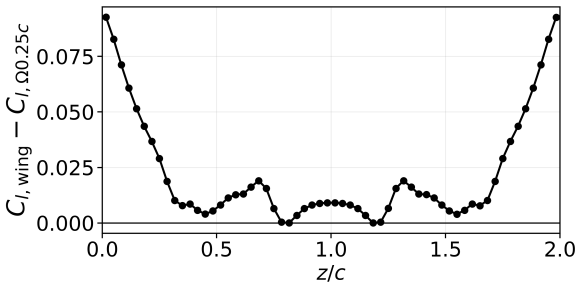


Figure 5.16: Spanwise evolution of the difference between the lift coefficient from *Ansys Fluent* and the lift coefficient extracted from the $\Omega_{0.25c}$ contour.

The lift coefficient obtained from the wing remains consistently larger than the one extracted from the contour. Local variations of the difference are observed near the vortex core locations, where the induced velocity gradients are strongest. The large increase observed near the lateral sides of the span is caused by the progressive decrease of the lift coefficient extracted from the contour as the vortex induced vertical velocity weakens away from the vortex cores, while the wing lift coefficient remains relatively stable.

Impact on AoA extraction

The accuracy of the AoA extraction is evaluated by considering the difference between the extracted AoA and the angle reconstructed from the wing lift coefficient obtained from *Ansys Fluent* using thin-airfoil theory:

$$\alpha - \frac{C_{l,\text{wing}}}{a_0}, \tag{5.5}$$

where a_0 denotes the lift-curve slope determined from Fig. 4.6. In the present case, $a_0 = 6.13$ rad^{-1}. The corresponding spanwise distribution is shown in Fig. 5.17.

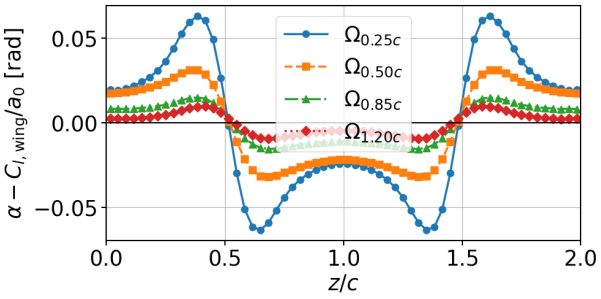


Figure 5.17: Spanwise evolution of the difference between the extracted AoA and C_l/a_0.

Pronounced local variations of the extracted AoA are observed near the imposed vortex locations, where the vortices strongly modify the local velocity field around the airfoil. The results also show a strong dependence on the contour location. The contours closest to the airfoil exhibit the largest local variations, whereas the farther contours produce smoother spanwise distributions. However, this does not necessarily imply a more physically accurate AoA estimation. Indeed, the closest contour, $\Omega_{0.25c}$, remains strongly sensitive to the local

induced velocity field and therefore captures more pronounced spanwise AoA variations generated by the vortices.

Overall, this suggests that the closest contour provides the most relevant representation of the local vortex–wing interaction, since it yields a more accurate lift prediction while also capturing the spanwise AoA variations induced by the vortices.

5.3.2 Case 2: Vortices impacting the wing

Flow topology and vortex–wing interaction

The interaction between the imposed counter-rotating vortices and the wing is first investigated through surface streamlines and dimensionless streamwise vorticity fields extracted in several yz planes along the streamwise direction.

Figure 5.18 presents the streamlines on both the pressure and suction sides of the airfoil. As the vortices approach the leading edge, each vortex is split into two parts which evolve separately on both sides of the wing. During the interaction, the vortex trajectories are significantly deviated by the presence of the wing. On the pressure side, the flow is deflected toward the interior whereas on the suction side the flow is deviated outward.



(a) Suction side (b) Pressure side

Figure 5.18: Surface streamlines on both sides of the wing.

The three-dimensional evolution of the streamlines is further illustrated in Fig. 5.19 and Fig. 5.20, which respectively show the flow upstream and downstream of the wing. As in the first case, the streamlines reveal the upward and downward velocity regions induced by the counter-rotating vortex pair.

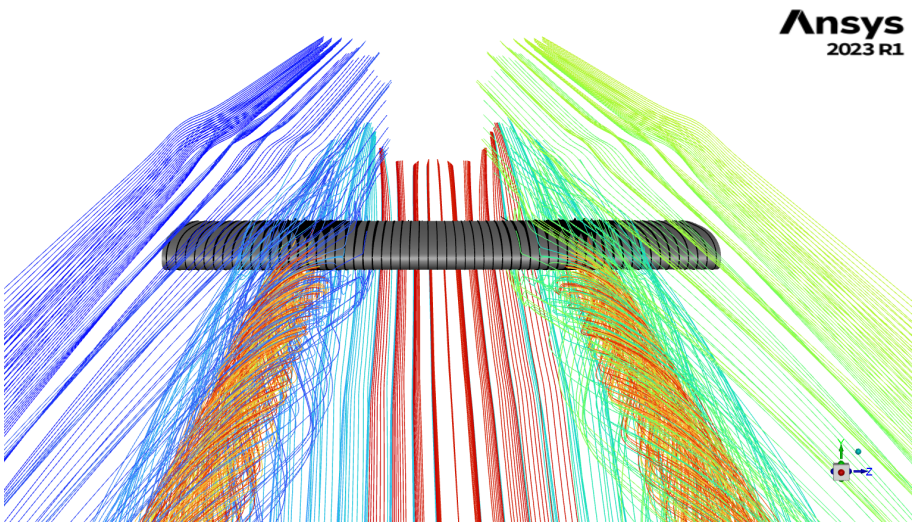


Figure 5.19: Three-dimensional streamlines approaching the wing from upstream

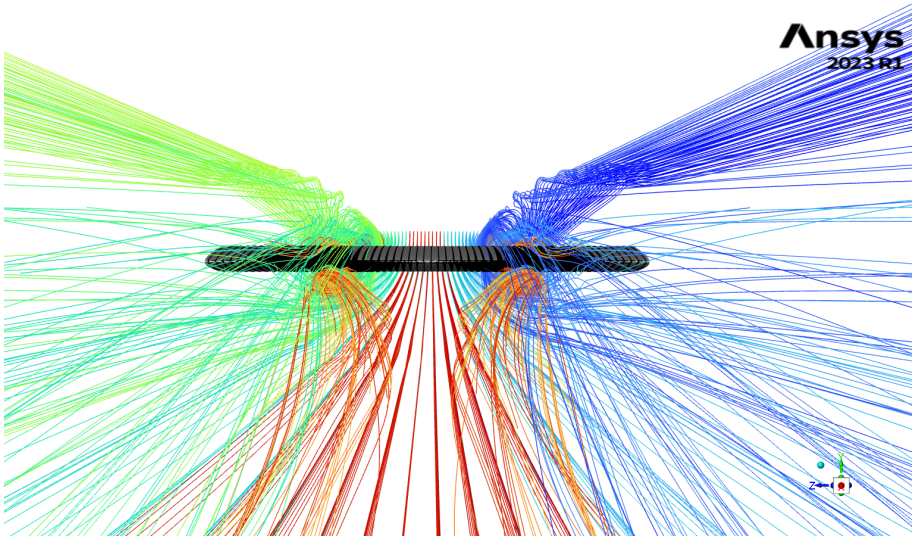


Figure 5.20: Three-dimensional streamlines downstream of the wing

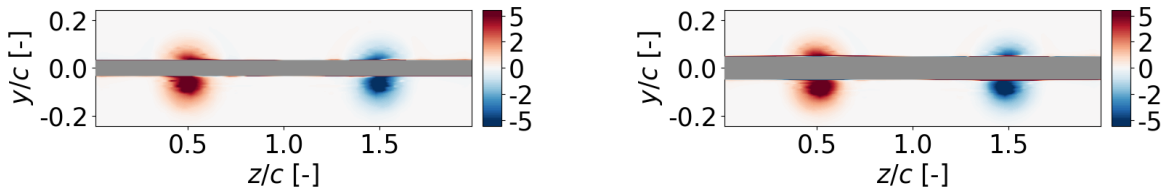
These observations are further confirmed by the dimensionless streamwise vorticity fields extracted in successive yz planes along the streamwise direction, as shown in Fig. 5.21. Near the leading edge, the vortex cores remain relatively compact and preserve their initial counter-rotating structure.

As the vortex pair is convected downward before reaching the wing, the vortices do not interact with the airfoil at $y = 0$, but at a slightly lower vertical position. The streamwise vorticity field in Fig. 5.23 shows that a larger portion of the vortical structures passes along the pressure side, explaining both the stronger vorticity and the more pronounced flow deflection observed in this region.

Further downstream, the vortices are displaced toward the interior region on the pressure side and toward the exterior on the suction side, consistently with the previously observed streamlines.

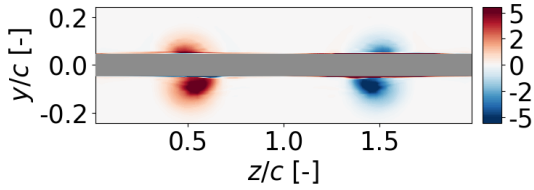
As the flow evolves downstream of the trailing edge, the vorticity originating from the

pressure side, the suction side, and the wake progressively interacts. The wake and the pressure side vorticity appear dominant, whereas the suction side vorticity remains weaker. These vortical structures progressively wrap around each other, leading to a coupled vortical structure in which the weaker suction side vorticity is entrained.

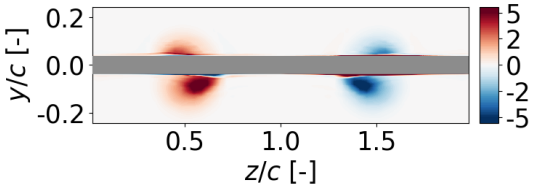


(a) $x/c = 0.05$

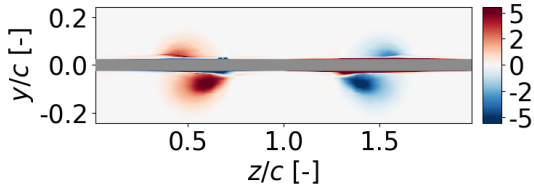
(b) $x/c = 0.20$



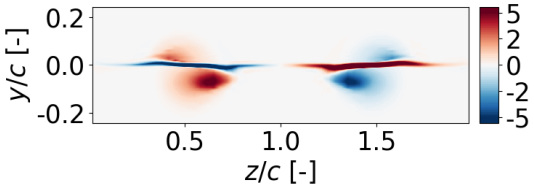
(c) $x/c = 0.40$



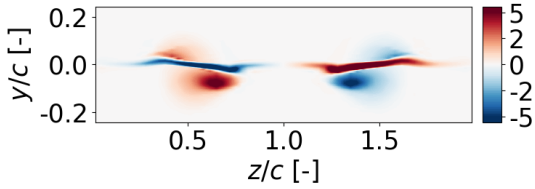
(d) $x/c = 0.60$



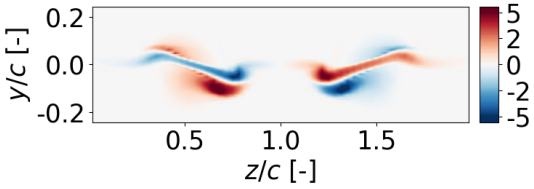
(e) $x/c = 0.80$



(f) $x/c = 1.20$



(g) $x/c = 1.40$



(h) $x/c = 2.00$

Figure 5.21: Dimensionless streamwise vorticity contours $\omega_x c/U_\infty$ in successive yz planes for streamwise locations ranging from $x/c = 0.05$ to $x/c = 2.00$.

Impact on lift coefficient estimation

The spanwise evolution of the lift coefficient is shown in Fig. 5.22. The wing lift coefficient exhibits a clear reduction in the central part of the wing, between the two imposed vortices. This behaviour is consistent with the downward velocity induced by the counter-rotating vortices in this region, which locally reduces the lift coefficient.

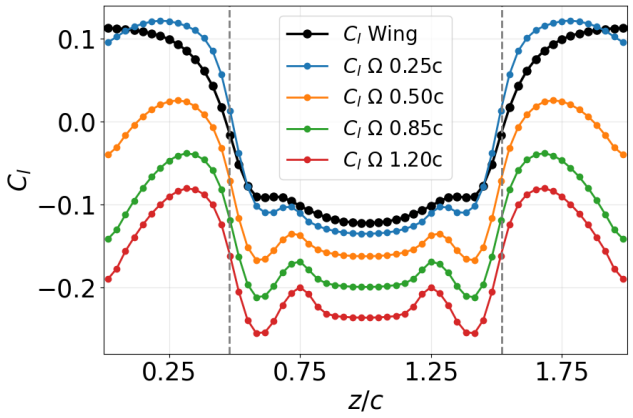


Figure 5.22: Spanwise evolution of the lift coefficient extracted from the different contours. The vertical dashed lines indicate the spanwise locations of the imposed vortices.

The contour-based predictions reproduce the same qualitative trend, although their accuracy strongly depends on the distance between the integration contour and the airfoil.

The closest contour, $\Omega_{0.25c}$, provides the best agreement with the wing lift coefficient, while the prediction progressively deteriorates as the contour distance from the airfoil increases.

As in the first case, the different extraction contours enclose different amounts of spanwise vorticity ω_z, as shown in Fig. 5.24. As the contour size increases, additional vorticity is included within the circulation integral, which modifies the computed circulation according to Stoke's theorem and therefore alters the lift coefficient predicted from the Kutta–Joukowski relation. Consequently, the farther contours exhibit larger deviations from the wing lift coefficient.

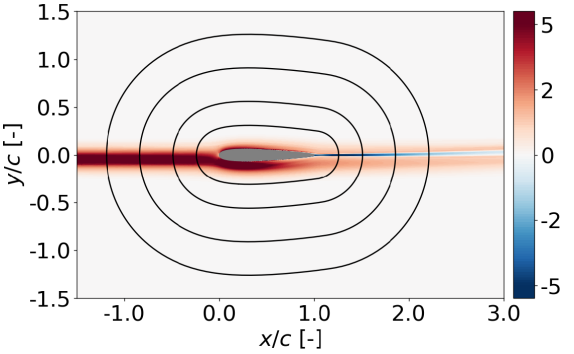


Figure 5.23: (a) Dimensionless streamwise voritcity $\omega_x c/U_\infty$ in the $z/c = 0.50$ plane

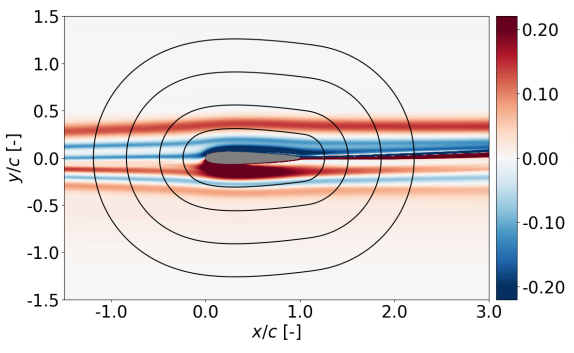


Figure 5.24: (b) Dimensionless spanwise vorticity $\omega_z c/U_\infty$ in the $z/c = 0.50$ plane

As in the first case, oscillations are also observed in the contour-based lift predictions.

These oscillations are directly related to the velocity field that the extraction contours intercept.

For instance, near $z/c = 0.375$, the leading edge of the contour intersects a region of strong positive vertical velocity, whereas the induced velocity intercepted near the trailing edge is weaker. This locally increases the extracted circulation and therefore the predicted lift coefficient.

Further along the span, the contour leading edge intersects regions characterized by negative vertical velocity, which reduces the extracted circulation and produces local minima in the predicted lift coefficient distribution.

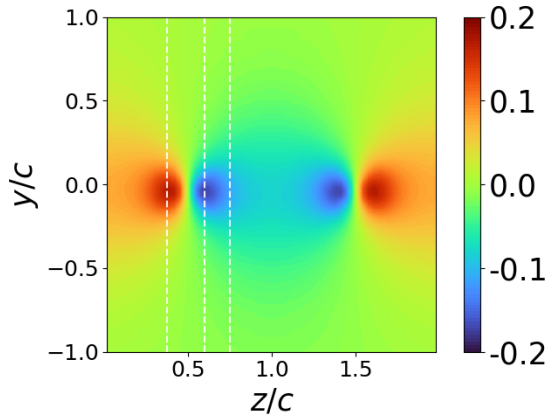


Figure 5.25: (a) $x/c = -1.20$

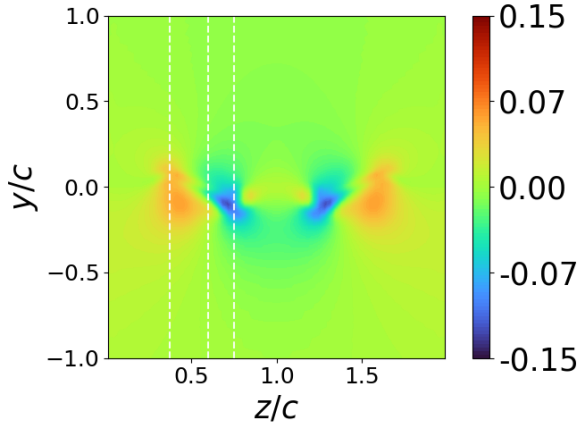


Figure 5.26: (b) a $x/c = 2.20$

Figure 5.27: Dimensionless vertical velocity field v/U_∞ in the yz plane upstream and downstream of the airfoil. White dashed lines indicate the spanwise locations of extrema in the predicted lift coefficient: $z/c = 0.375$, 0.5, and 0.7.

The difference between the lift coefficient extracted from the closest contour and the reference lift coefficient directly obtained from *Ansys Fluent* can now be analyzed. Strong local deviations are observed near $z/c \simeq 0.5$ and $z/c \simeq 1.5$, corresponding to the vortex core locations. The difference increases in regions characterized by positive induced vertical velocity and decreases where the induced vertical velocity becomes negative. This behavior is similar to that observed in the first configuration, although the deviations are significantly amplified here due to the stronger vortex–wing interaction.

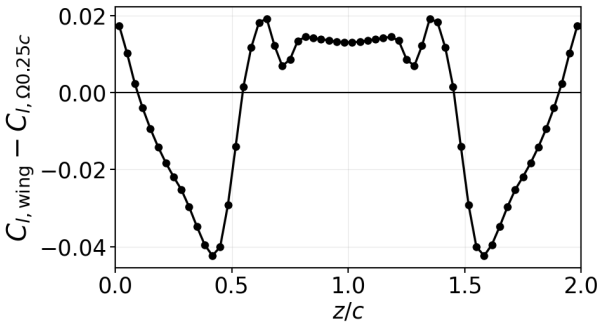


Figure 5.28: Difference between the lift coefficient from *Ansys Fluent* and the lift coefficient extracted from the $\Omega 0.25c$ contour

Impact on the AoA extraction

Figure 5.29 shows the spanwise evolution of the quantity $\alpha - C_l/a_0$ for the different contour locations. As in the first case, strong local variations are observed near the vortex cores, highlighting the strong influence of the imposed vortices on the AoA extraction.

The closest contour, $\Omega_{0.25c}$, exhibits the largest local fluctuations, indicating a strong sensitivity to the intense velocity gradients generated by the vortices. Since this contour is located close to the airfoil surface, it directly samples the highly non-uniform induced velocity field surrounding the vortex cores. As a result, the extracted AoA strongly reflects the local flow perturbations induced by the imposed vortices.

In contrast, the farther contours exhibit smoother spanwise distributions and smaller values of $\alpha - C_l/a_0$. This behaviour suggests that these contours are less sensitive to the strong local velocity gradients generated by the vortices.

As in the first case, the closest contour appears to provide a more representative estimate of the AoA of the local flow experienced by the wing, whereas the farther contours produce smoother distributions that are less representative of the local flow field.

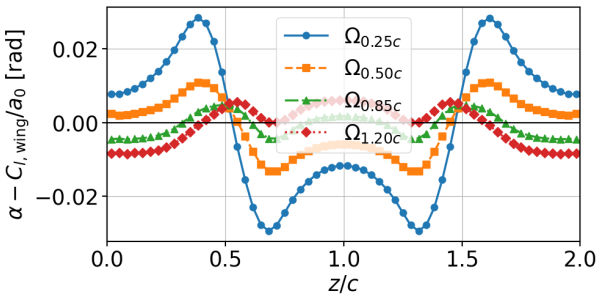


Figure 5.29: Spanwise evolution of the difference between the extracted AoA and the lift-based estimate C_l/a_0.

5.4 Conclusion

The AoA extraction methodology was applied to three-dimensional wall-modeled RANS simulations in the presence of imposed counter-rotating vortices representative of blade–vortex interaction phenomena. The use of adaptive mesh refinement proved essential to preserve the imposed vortex structures during their convection toward the wing.

The results showed that the vortex induced velocity field strongly modifies the local flow topology, the spanwise lift distribution, and the extracted AoA. In both investigated configurations, the methodology provided reasonably accurate estimates of the lift coefficient and AoA for each spanwise section.

However, the accuracy of the estimation strongly depends on the contour location. The closest contour, $\Omega_{0.25c}$, generally provided the best agreement with the reference wing quantities as it directly samples the highly non-uniform velocity field induced by the vortices.

Chapter 6

Conclusion and Perspectives

The first part of this work demonstrated that the classical Kutta–Joukowski formulation provides accurate lift predictions within the weakly compressible regime considered in this study. Although the circulation should theoretically remain conserved across the different integration contours, small unphysical variations were observed. These variations may be associated with both spurious vorticity induced by the mesh and turbulence modelling effects.

The second part of the work focused on the extraction of the AoA from two-dimensional wall-resolved simulations. The flat plate assumption provided a more realistic representation of the circulation distribution than the uniform model and generally led to more accurate AoA predictions. The contour location was also shown to influence the estimation accuracy. While contours located farther from the airfoil provided more accurate effective velocity estimations, the closest contour, $\Omega_{0.25c}$, generally provided better AoA predictions.

The third part of the study investigated the use of wall functions combined with an improved mesh topology. The wall-function approach successfully reproduced the main aerodynamic quantities obtained with the wall-resolved simulations while significantly reducing the computational cost.

Finally, the methodology was applied to three-dimensional wall-modelled simulations involving imposed counter-rotating vortices representative of blade–vortex interaction phenomena. Adaptive mesh refinement proved essential to limit the numerical diffusion of the vortices during their convection toward the wing. The results showed that the velocity field induced by the vortices strongly modified the spanwise lift distribution and the extracted AoA.

The contour location again played a major role in the estimation accuracy. The $\Omega_{0.25c}$ contour generally provided the best agreement with the reference lift distribution. In contrast, contours located farther from the airfoil exhibited larger deviations, due to the larger amount of spanwise vorticity enclosed within the integration domain.

6.1 Perspectives

A natural continuation of this work would be to extend the methodology to unsteady aerodynamic configurations. Dynamic stall cases would constitute a relevant application,

as they involve temporal variations of circulation, and flow separation.

A functional two-dimensional dynamic-stall setup was already developed in *Ansys Fluent* in parallel of this work. Future investigations could therefore focus on applying the extraction methodology to transient and separated flows in order to assess its robustness under unsteady aerodynamic conditions. These developments would allow the method to be evaluated in more realistic configurations, where transient vortex dynamics play a central role.

Use of AI

I used ChatGPT for grammatical corrections and reformulation of some sentences. I also used AI assistance for coding, such as graph generation.

Appendix A

Circulation redistribution

To redistribute the total circulation Γ according to the flat plate distribution, only the shape of the theoretical distribution is retained. The vortex sheet strength can be expressed as:

$$\gamma(x) = A\sqrt{\frac{1 - x/c}{x/c}}, \tag{A.1}$$

where A is a constant such that the integral of $\gamma(x)$ over the chord recovers the total circulation. Substituting Eq. (A.1) into the circulation integral gives:

$$\Gamma = A\int_0^c \sqrt{\frac{1 - x/c}{x/c}}\, dx. \tag{A.2}$$

Introducing the change of variable $X = x/c$, with $dx = c\, dX$, one obtains:

$$\Gamma = \int_0^c \gamma(x)\, dx = Ac\int_0^1 \sqrt{\frac{1 - X}{X}}\, dX. \tag{A.3}$$

Since $\int_0^1 \sqrt{\frac{1-X}{X}}\, dX = \frac{\pi}{2}$, the normalization constant is $A = \frac{2\Gamma}{\pi c}$.
The normalized flat plate circulation distribution therefore becomes

$$\gamma(x) = \frac{2\Gamma}{\pi c}\sqrt{\frac{1 - x/c}{x/c}}. \tag{A.4}$$

This expression preserves the chordwise shape of the flat plate distribution while ensuring that its integral over the chord is equal to the circulation Γ extracted from the iso-distance contour.

Flat plate circulation distribution using potential flow theory

The thin flat plate can be obtained from a circle of radius a in the complex Z-plane using the Joukowski transformation $z = Z + \frac{a^2}{Z}$. [21] For a point on the circle $Z = ae^{i\theta}$, the

corresponding point on the plate is:

$$z(\theta) = ae^{i\theta} + \frac{a^2}{ae^{i\theta}} = a\left(e^{i\theta} + e^{-i\theta}\right) = 2a\cos\theta \tag{A.5}$$

Thus, the circle is mapped onto a flat plate ranging from $z_L = -2a$ to $z_T = 2a$. The chord is therefore $c = 4a$. The complex potential for a uniform flow at an angle of attack α, with circulation Γ, is:

$$F(Z) = U_\infty\left(Ze^{-i\alpha} + \frac{a^2}{Z}e^{i\alpha}\right) + \frac{\Gamma}{2\pi i}\log\left(\frac{Z}{a}\right) \tag{A.6}$$

Evaluating this expression on the circle $Z = ae^{i\theta}$, the complex velocity in the physical z-plane is obtained from

$$\overline{w}(z) = \frac{dF/dZ}{dz/dZ} = \frac{U_\infty\left(e^{-i\alpha} - \frac{a^2}{Z^2}e^{i\alpha}\right) + \frac{\Gamma}{2\pi i}\frac{1}{Z}}{1 - \frac{a^2}{Z^2}} \tag{A.7}$$

At the trailing edge, $Z = a$, the denominator vanishes. To impose a finite velocity there, the numerator must also vanish. This is the Kutta condition:

$$U_\infty\left(e^{-i\alpha} - e^{i\alpha}\right) + \frac{\Gamma}{2\pi i a} = 0 \tag{A.8}$$

Using $e^{-i\alpha} - e^{i\alpha} = -2i\sin\alpha$, one obtains : $\Gamma = -4\pi U_\infty a\sin\alpha$.
The complex potential and the associated complex velocity can therefore be rewritten as:

$$F(Z) = U_\infty\left(Ze^{-i\alpha} + \frac{a^2}{Z}e^{i\alpha} + i\,2a\sin\alpha\log\left(\frac{Z}{a}\right)\right), \tag{A.9}$$

$$\overline{w}(z(Z)) = \frac{U_\infty\left(e^{-i\alpha} - \frac{a^2}{Z^2}e^{i\alpha} + i\,2\sin\alpha\,\frac{a}{Z}\right)}{1 - \frac{a^2}{Z^2}} = U_\infty\frac{\sin(\theta-\alpha) + \sin\alpha}{\sin\theta} = u - iv \tag{A.10}$$

We again verify that $v = 0$ and hence the flow is parallel to the plate. The velocity at the trailing edge therefore remains finite :

$$u_T = U_\infty\cos\alpha. \tag{A.11}$$

For small angles of attack, this velocity remains very close to U_∞. Using the trigonometric identity $\tan\left(\frac{A}{2}\right) = \frac{1-\cos A}{\sin A}$ and since $v = 0$, the velocity remains tangent to the plate and the tangential velocity component reduces to:

$$u = U_\infty\left(\cos\alpha + \frac{1-\cos\theta}{\sin\theta}\sin\alpha\right). \tag{A.12}$$

Here, the coordinate x is measured from the mid-chord of the plate, such that $x \in [-c/2, c/2]$. Using

Using $\cos\theta = \frac{x}{2a} = \frac{2x}{c}$, any position x along the plate can be related to the angular coordinate θ.

The upper side of the plate corresponds to $0 \leq \theta \leq \pi$, and therefore $\sin\theta = \sqrt{1-\left(\frac{2x}{c}\right)^2} \geq 0$. The velocity distribution along the upper side therefore becomes:

$$u^+ = U_\infty \left(\cos\alpha + \frac{1-\frac{2x}{c}}{\sqrt{1-\left(\frac{2x}{c}\right)^2}} \sin\alpha \right) = U_\infty \left(\cos\alpha + \sqrt{\frac{1-\frac{2x}{c}}{1+\frac{2x}{c}}} \sin\alpha \right) \tag{A.13}$$

The lower side of the plate corresponds to $\pi \leq \theta \leq 2\pi$, and therefore $\sin\theta = -\sqrt{1-\left(\frac{2x}{c}\right)^2} \leq 0$. The velocity below the plate is therefore :

$$u^- = U_\infty \left(\cos\alpha - \sqrt{\frac{1-\frac{2x}{c}}{1+\frac{2x}{c}}} \sin\alpha \right). \tag{A.14}$$

The vortex sheet strength is then obtained from the tangential velocity jump:

$$\gamma = u^+ - u^- = 2U_\infty \sqrt{\frac{1-\frac{2x}{c}}{1+\frac{2x}{c}}} \sin\alpha. \tag{A.15}$$

Here, x is measured from the mid-chord. To compare this result with the thin airfoil notation, a leading-edge coordinate $\tilde{x} \in [0, c]$ is introduced.

$$\frac{\tilde{x}}{c} = \frac{1}{2}(1+\cos\theta) \tag{A.16}$$

with $0 \leq \theta \leq \pi$ and so, $0 \leq \frac{\tilde{x}}{c} \leq 1$. One obtains:

$$\frac{\tilde{x}}{c} = \left(\frac{1}{2} + \frac{x}{c}\right) \quad \text{and} \quad 1 - \frac{\tilde{x}}{c} = \left(\frac{1}{2} - \frac{x}{c}\right) \tag{A.17}$$

The tangential velocity above and below the plate can therefore be written as:

$$u^+ = U_\infty \left(\cos\alpha + \sqrt{\frac{1-\frac{\tilde{x}}{c}}{\frac{\tilde{x}}{c}}} \sin\alpha \right) \tag{A.18}$$

$$u^- = U_\infty \left(\cos\alpha - \sqrt{\frac{1-\frac{\tilde{x}}{c}}{\frac{\tilde{x}}{c}}} \sin\alpha \right) \tag{A.19}$$

The vortex sheet strength finally becomes:

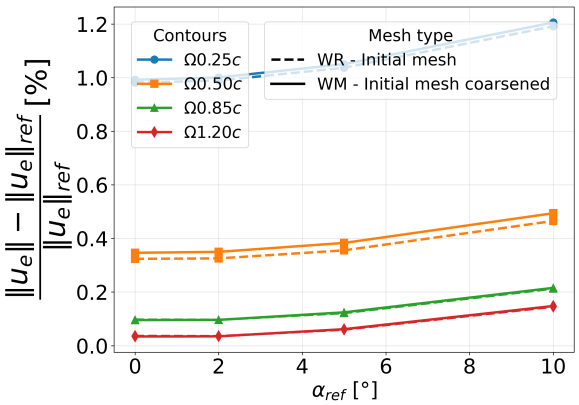
$$\gamma = u^+ - u^- = 2U_\infty \sqrt{\frac{1-\frac{\tilde{x}}{c}}{\frac{\tilde{x}}{c}}} \sin\alpha = 2U_\infty \frac{1-\cos\theta}{\sin\theta} \sin\alpha \tag{A.20}$$

Considering small AoA, $\sin\alpha \simeq \alpha$ and therefore:

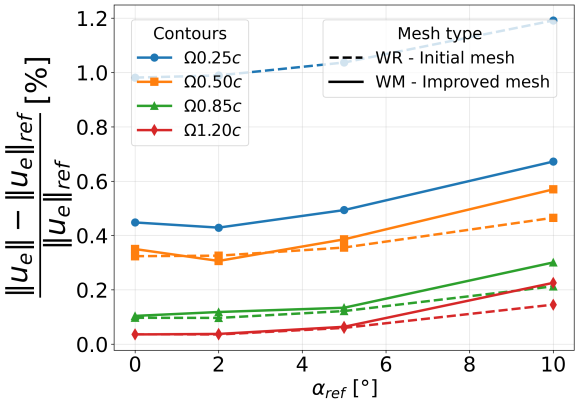
$$\gamma(\tilde{x}) \simeq 2U_\infty \alpha \sqrt{\frac{1-\tilde{x}/c}{\tilde{x}/c}} \tag{A.21}$$

This result is identical to the distribution obtained from thin airfoil theory, demonstrating the equivalence between both approaches for a flat plate at small angle of attack.

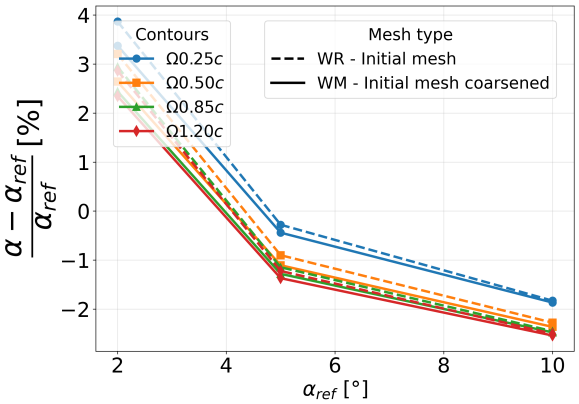
Figures



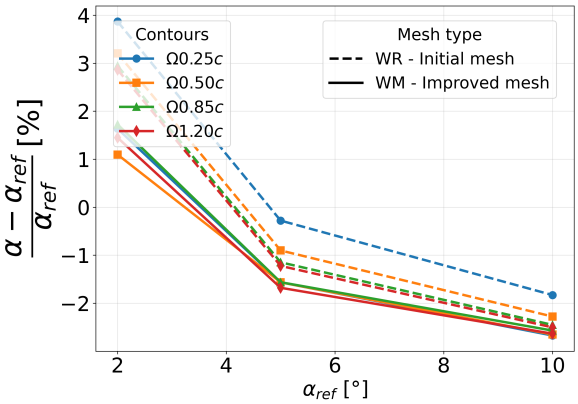
(a) Relative error in the effective velocity magnitude $||u_e||$ for the initial coarsened mesh.



(b) Relative error in the effective velocity magnitude $||u_e||$ for the improved mesh.

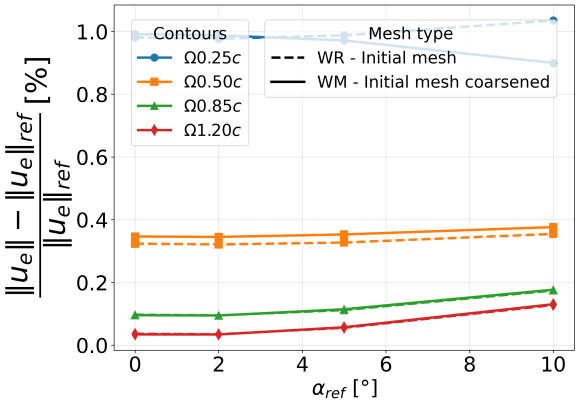


(c) Relative AoA error for the initial coarsened mesh.

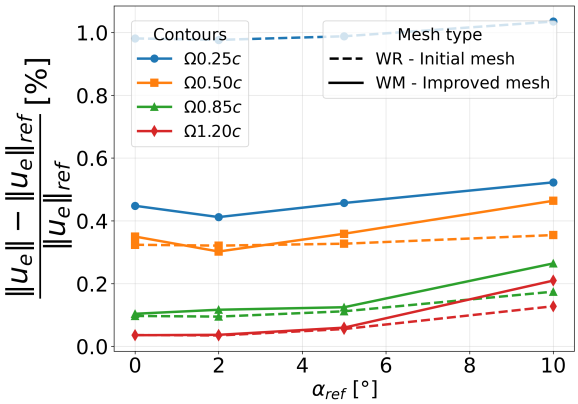


(d) Relative AoA error for the improved mesh.

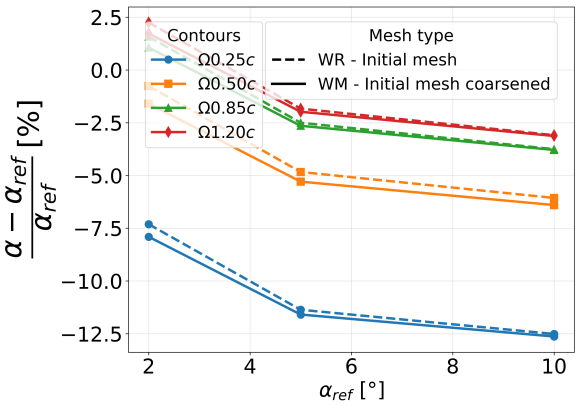
Figure A.1: Comparison with the wall-resolved reference for the compressible case using the flat-plate assumption: relative error in the effective velocity magnitude $||u_e||$ (top) and relative AoA error (bottom) for both mesh configurations.



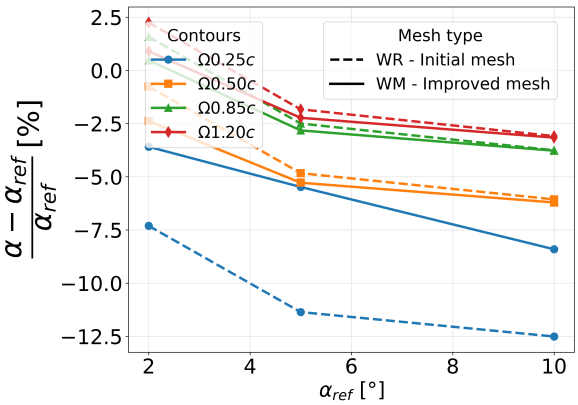
(a) Relative error in the effective velocity magnitude $||u_e||$ for the initial coarsened mesh.



(b) Relative error in the effective velocity magnitude $||u_e||$ for the improved mesh.



(c) Relative AoA error for the initial coarsened mesh.



(d) Relative AoA error for the improved mesh.

Figure A.2: Comparison with the wall-resolved reference for the compressible case using the uniform circulation assumption: relative error in the effective velocity magnitude $||u_e||$ (top) and relative AoA error (bottom) for both mesh configurations.

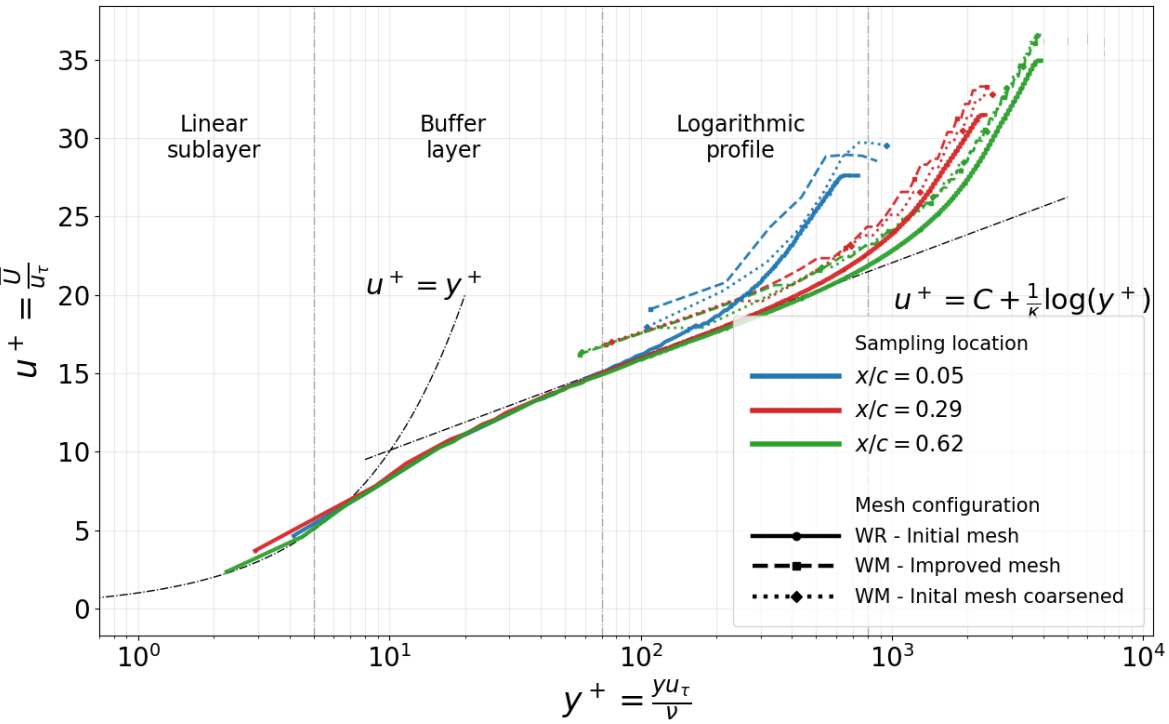


Figure A.3: Comparison of the dimensionless velocity profiles $u^+(y^+)$ measured along the sampling normals with the theoretical law-of-the-wall profile (black dashed line) for the wall-resolved and wall-modeled configurations in the compressible case.

Bibliography

[1] H. Rahimi, J. G. Schepers, W. Z. Shen, N. R. García, M. S. Schneider, D. Micallef, C. S. Ferreira, E. Jost, L. Klein, and I. Herráez, "Evaluation of different methods for determining the angle of attack on wind turbine blades with cfd results under axial inflow conditions," *Renewable Energy*, vol. 125, pp. 866–876, 2018.

[2] W. Z. Shen, M. O. Hansen, and J. N. Sørensen, "Determination of angle of attack (aoa) for rotating blades," in *Wind Energy: Proceedings of the Euromech Colloquium*, pp. 205–209, Springer, 2007.

[3] D.-G. Caprace, M. Mounier, D. G. Perez, P. V. Diaz, and S. Yoon, "Comparing methods to extract sectional angle of attack from blade-resolved rotor simulations," in *50th European Rotorcraft Forum 2024*, 2024.

[4] K. Zaman, A. F. Fagan, and M. R. Mankbadi, "An experimental study and database for tip vortex flow from an airfoil," tech. rep., 2017.

[5] H. Rahimi, M. Hartvelt, J. Peinke, and J. G. Schepers, "Investigation of the current yaw engineering models for simulation of wind turbines in bem and comparison with cfd and experiment," in *Journal of Physics: Conference Series*, vol. 753, p. 022016, IOP Publishing, 2016.

[6] D.-G. Caprace, G. Winckelmans, and P. Chatelain, "Assessment of the vortex particle-mesh method for efficient les of hovering rotors and their wakes," in *AIAA Scitech 2021 Forum*, p. 0738, 2021.

[7] G. Winckelmans, "En-1." LMECA2323 – Aerodynamic of external flows.

[8] P. Chatelain, D.-G. Caprace, and G. Winckelmans, "Support for lmeca2323 course: Wake rollup from an elliptical wing using the vortex particle-mesh method with immersed lifting and dragging line (vpm-ildl)," 2020. Course support material.

[9] G. Winckelmans, "En-1, p. 2." LMECA2323 – Aerodynamic of external flows.

[10] G. Winckelmans, "En-2, p.1-6." LMECA2323 – Aerodynamic of external flows.

[11] C. K. Zioutis, A. I. Spyropoulos, A. P. Fragias, D. P. Margaris, and D. G. Papanikas, "Influence of helicopter rotor wake modeling on blade airload predictions," *International Journal of Engineering*, vol. 3, no. 6, pp. 521–535, 2010.

[12] ANSYS Inc., *ANSYS Fluent Theory Guide*, 2025. Release 2025 R2.

[13] S. A. Khan, M. Bashir, M. A. A. Baig, and F. A. G. M. Ali, "Comparing the effect of different turbulence models on the cfd predictions of naca0018 airfoil aerodynamics," *CFD letters*, vol. 12, no. 3, pp. 1–10, 2020.

[14] N. Shelil, "2d numerical simulation study of airfoil performance," *Wind Energy Science Discussions*, vol. 2021, pp. 1–19, 2021.

[15] L. Mangani, M. Darwish, and F. Moukalled, "An openfoam pressure-based coupled cfd solver for turbulent and compressible flows in turbomachinery applications," *Numerical Heat Transfer, Part B: Fundamentals*, vol. 69, no. 5, pp. 413–431, 2016.

[16] N. M. Khalifa, A. S. Rezaei, and H. E. Taha, "Comparing the performance of different turbulence models in predicting dynamic stall," in *AIAA Scitech 2021 Forum*, p. 1651, 2021.

[17] ANSYS Inc., "Ansys fluent user's guide – boundary conditions." `https://ansyshelp.ansys.com/public/account/secured?returnurl=/Views/Secured/corp/v261/en/flu_ug/flu_ug_bcs_sec_bound_cond.html`, 2026.

[18] Flow360 Help Center, "Turbulence quantities." `https://flow360-help-center.simulation.cloud/02.simulation-setup/03.flow-solver/01.boundary-conditions/08.turbulence-quantities.html`, 2024.

[19] C. L. Rumsey, "Apparent transition behavior of widely-used turbulence models." `https://ntrs.nasa.gov/api/citations/20060017022/downloads/20060017022.pdf`, 2006. NASA Langley Research Center, AIAA-2006-3906.

[20] V. G. Winckelmans, "Mecanique des fluides et transferts 1." LMECA1321 – MECANIQUE DES FLUIDES ET TRANSFERTS 1.

[21] G. Winckelmans, "Steady, incompressible and irrotational, 2-d flows." LMECA2322 – Fluid mechanics 2.

[22] G. Winckelmans, "Lmeca2322: Fluid mechanics and transfer 2: Compressible flows." LMECA2322 – Fluid mechanics 2.

[23] N. Golmirzaee and D. H. Wood, "Some effects of domain size and boundary conditions on the accuracy of airfoil simulations," *Advances in Aerodynamics*, vol. 6, no. 1, p. 7, 2024.

[24] G. Winckelmans, "En-1, p. 30." LMECA2323 – Aerodynamic of external flows.

[25] G. Kalitzin, G. Medic, G. Iaccarino, and P. Durbin, "Near-wall behavior of rans turbulence models and implications for wall functions," *Journal of Computational Physics*, vol. 204, no. 1, pp. 265–291, 2005.

[26] Y. Marchal, "Efficient and accurate simulation of the flow past moving bodies," Master's thesis, 2022.

[27] ANSYS Inc., "Fluent user's guide – near-wall treatments and wall functions." `https://ansyshelp.ansys.com/public/account/secured?returnurl=/Views/Secured/corp/v251/en/flu_th/ch04s18s02.html`, 2025.

[28] D.-F. Feder and M. Abdel-Maksoud, "Tracking a tip vortex with adaptive vorticity confinement and hybrid rans-les," *Open Journal of Fluid Dynamics*, vol. 6, no. 4, pp. 406–429, 2016.

[29] N. Secco, G. K. W. Kenway, P. He, C. A. Mader, and J. R. R. A. Martins, "Efficient mesh generation and deformation for aerodynamic shape optimization," *AIAA Journal*, 2021.

[30] NASA Ames Research Center, "Nasa hover verification and acoustic baseline (hvab) program." `https://rotorcraft.arc.nasa.gov/HVAB/generalInformation.html`, 2026.

[31] G. Winckelmans, "En-1, p.18." LMECA2323 – Aerodynamic of external flows.

UNIVERSITÉ CATHOLIQUE DE LOUVAIN
École polytechnique de Louvain
Rue Archimède, 1 bte L6.11.01, 1348 Louvain-la-Neuve, Belgique | **www.uclouvain.be/epl**